COMPUTATIONAL INVESTIGATION OF SELECTIVE ONE- AND TWO-PHOTON INDUCED ACTIVATION OF PHOTOLABILE PROTECTING GROUPS: FROM VIPER SPECTROSCOPY TO TANDEM UNCAGING

DISSERTATION
ZUR ERLANGUNG DES DOKTORGRADES
DER NATURWISSENSCHAFTEN

VORGELEGT BEIM FACHBEREICH 14
DER JOHANN WOLFGANG GOETHE-UNIVERSITÄT
IN FRANKFURT AM MAIN

VON
MADHAVA SHYAM NIRAGHATAM

AUS
BANGALORE, INDIEN

FRANKFURT AM MAIN
2022

(D30)

vom Fachbereich 14 Biochemie, Chemie und Pharmazie
der Johann Wolfgang Goethe-Universität als Dissertation angenommen

Dekan:	Prof. Dr. Clemens Glaubitz
Gutachter:	Prof. Dr. Irene Burghardt
	Prof. Dr. Jens Bredenbeck

Datum der Disputation: .....

It doesn't matter how beautiful your theory is ...
If it doesn't agree with experiment, it's wrong.

— Richard Feynman

ABSTRACT

This work deals with the theoretical investigation of the vibrationally promoted electronic resonance (VIPER) experiment, the intramolecular energy transfer within a rhodamine-BODIPY antenna system initiated by two-photon excitation and a computational study of the photochemical mechanism of the uncaging of the [7-(dimethylamino)coumarin-4-yl]methyl (DEACM) class of photocages . In continuation to Jan von Cosel's work, the setup for the theoretical investigation of the VIPER experiment has been extended to two-photon absorption (TPA) also including the first-order Herzberg-Teller (HT) effects which are dependent on changes with respect to nuclear coordinates.

The VIPER experiment constitutes an extended form of two-dimensional infrared (2DIR) spectroscopy with a sequence of infrared (IR) and ultraviolet (UV) or visible (vis) pulses. The molecular system under probe is excited initially by a narrow-band IR pump pulse and then electronically excited by an off-resonant UV/vis pulse. An IR probe pulse is applied afterwards to probe the system and record a 2DIR spectrum in combination with the first pulse. Since the lifetime of the vibrational excitation is very short, the electronic excitation by the UV/vis pulse is used to enlarge the lifetime of the excitation in the molecule and thus enable measurements on a longer timescale. Therefore, it becomes easier to study dynamical photochemical processes on long timescales. In the VIPER experiment with TPA, the UV/vis pulse is replaced by a near-infrared (NIR) pulse which offers an intrinsic 3D resolution, minimzed photodamage, a lower noise level and an increased penetration depth. This makes TPA highly attractive for biological systems among a wide range of other possible applications.

The computation of the vibrationally resolved electronic absorption spectra accounts for the Franck-Condon (FC) contributions which are independent of the nuclear framework as well as the HT effects which are dependent on the nuclear coordinates. The FC contributions are dominant for electronically-allowed transitions whereas HT contributions could be important for weakly-allowed or forbidden transitions. Laying emphasis on TPA, the test systems used belong to the category of two-photon active compounds. The initial candidate is dimethylamino-nitrodibenzofuran (DMA-NDBF) which has been reported to be a two-photon only caging compound. The other system is a well-known laser dye, a rhodamine derivative of the commercially available rhodamine 101 (Rh101). Rhodamines are also recognized for their excellent TPA characteristics.

The findings for both the test systems show interesting contrasts. The one-photon absorption (OPA) and TPA spectrum together with vibronic couplings present the same lineshape in case of DMA-NDBF and also the HT effects have very weak contributions to the vibronic spectrum. Insignificant HT effects are quite typical for electronically allowed transitions. Overall, the NO_2 bending mode exhibits the strongest change in the absorption spectrum upon vibrational pre-excitation, even stronger than in the case of different ring distortion modes that usually show a high VIPER activity. In the case of rhodamine, the vibronic OPA spectrum is predominantly the FC spectrum and the HT couplings have a very weak contribu-

tion. The vibronic TPA spectrum is entirely dominated by the HT contributions and hence, the vibrationally resolved TPA spectrum of the rhodamine is a HT-only spectrum. Explanations towards this behaviour have been reported by Milojevich *et al.* which are holding the change in symmetry of the molecular orbital transitions from the ground to the excited state accountable. No significantly VIPER-active normal modes could be determined owing to the low magnitudes of their dimensionless displacements that are connected to the Huang-Rhys factors. Two ring distortion modes however have been probed but the intensity of their vibrational pre-excitation is observed to be very low.

The other part of this work is concerned with the estimation of the rate of the intramolecular energy transfer within rhodamine-BODIPY dyads. After the investigations on the prospective rhodamine derivatives, the Rho101 derivative shows the highest TPA activity. This linked together with the BODIPY derivative with styryl substituents through an acetylene bond has been probed theoretically as well as experimentally for the excitation energy transfer (EET).

Time-resolved spectroscopic measurements reveal an ultrafast energy transfer process on femtosecond timescales. The theoretical estimation of the EET rates through the Förster theory and the determination of the coupling between the donor and acceptor groups by the transition density cube (TDC) method falls short of the experimental results. Because of this disagreement, quantum dynamics simulations with the multi-layer multi-configuration time-dependent Hartree (ML-MCTDH) method have been performed on an adapted rhodamine-BODIPY molecular dyad which reveal that the energy transfer occurs through transient coherence whose mechanism cannot be described by Förster theory.

Towards the end, a theoretical study to understand the photochemical mechanism of uncaging in the DEACM class of photocages specifically with respect to the leaving groups (LG) is illustrated. An attempt to interpret LG-specific kinetics for the three DEACM species having thiocyanate (-SCN), azide (-N_3) and carbonate respectively as LGs has been made by performing excited-state potential energy surface (PES) scans. The scan coordinates include the dissociative DEACM-LG distance coordinate as well as the dihedral angle of the LG relative to the coumarin scaffold. In all the three systems, the DEACM scaffold remains as a spectator after serving as a light harvesting antenna upon S_1 ($\pi - \pi^*$) bright state after excitation. From the 2D relaxed PES scans, it is revealed that the bond cleavage in all systems is preceded by a rotation of the dihedral angle upto an almost perpendicular orientation of the LG with respect to the DEACM plane. The DEACM-SCN undergoes barrierless dissociation whereas the DEACM-N_3 and DEACM-Carb species have to surpass a comparatively steep barrier in order to undergo dissociation.

ZUSAMMENFASSUNG

Diese Arbeit befasst sich mit der theoretischen Untersuchung des VIPER (vibrationally promoted electronic resonance) Experiments, dem intramolekularen Energietransfer einer Rhodamin-BODIPY-Dyade, der durch eine Zwei-Photonen-Anregung („two-photon absorption“, TPA) initiiert wird sowie der theoretischen Untersuchung der Dissoziationsmechanismen verschiedener Abgangsgruppen („leaving group“, LG) an einer Coumarin-basierten Photoschutzgruppe. Aufbauend auf Arbeiten von Jan von Cosel wurde die theoretische Untersuchung des VIPER-Experiments auf die TPA erweitert, wobei auch die geometrieabhängigen Herzberg-Teller-Effekte (HT) erster Ordnung berücksichtigt werden.

Das VIPER-Experiment ist eine erweiterte Form der zweidimensionalen Infrarotspektroskopie (2DIR) mit einer Abfolge von Infrarot- (IR) und Ultravioletten- (UV) oder sichtbaren (Vis) Pulsen. Das jeweilige untersuchte molekulare System wird dabei zunächst durch einen schmalbandigen IR-Puls und anschließend durch einen nicht resonanten UV/Vis-Puls elektronisch angeregt. Am Ende der Pulssequenz steht ein weiterer IR-Puls, der den Zustand des Systems abfragt und in Kombination mit dem ersten IR-Puls ein 2DIR-Spektrum aufnimmt. Da die Lebensdauer der Schwingungsanregung sehr kurz ist, kann es schwierig sein dynamische Prozesse zu untersuchen. Die zusätzliche elektronische Anregung durch den UV/Vis-Puls ermöglicht daher eine Untersuchung dynamischer photochemischer Prozesse auf den Zeitskalen der deutlich längeren Lebensdauer der elektronischen Anregung. Im Falle des VIPER-Experiments, welches eine TPA nutzt, wird der UV/Vis-Puls durch einen Puls im nahen Infrarotbereich (Near-infrared, NIR) ersetzt, der durch eine größere Eindringtiefe, minimierte Photoschäden und eine intrinsische dreidimensionale Auflösung große Vorteile im Speziellen bei der Anwendung an biologischen Proben bringt.

Um die Frage zu adressieren, welche Normalmoden besonders effizient für eine Voranregung durch den IR-Puls im VIPER-Experiment genutzt werden können, wurden schwingungsaufgelöste Absorptionsspektren berechnet. Die Berechnung dieser schwingungsaufgelösten elektronischen Absorptionsspektren berücksichtigt sowohl die Franck-Condon-Beiträge (FC), die unabhängig vom Kerngerüst sind, als auch die HT-Effekte, die von einer Geometrieänderung der Kernkoordinaten abhängen. Die FC-Beiträge sind für elektronisch erlaubte Übergänge dominant, während HT-Beiträge für schwache oder verbotene Übergänge wichtig sein können. Mit dem Schwerpunkt der TPA gehören alle innerhalb dieser Arbeit verwendeten Testsysteme zur Kategorie der Zwei-Photonen-aktiven Verbindungen. Das erste betrachtete System ist Dimethylamino-Nitrodibenzofuran (DMA-NDBF), welches eine bekannte TPA aktive Verbindung ist. Das zweite betrachtete System ist ein bekannter Laserfarbstoff, ein Rhodaminderivat des handelsüblichen Rhodamin 101 (Rh101). Rhodamine sind ebenfalls für ihre hervorragenden TPA-Eigenschaften bekannt.

Die Ergebnisse für die beiden Moleküle weisen interessante Kontraste auf. Das Ein-Photonen-Absorptionsspektrum (OPA) und das TPA-Spektrum weisen im Falle von DMA-NDBF die gleiche Form auf und der HT-Anteil trägt nur sehr schwach

zum vibronischen TPA Spektrum bei. Unbedeutende HT-Effekte sind typisch für elektronisch erlaubte Übergänge. Insgesamt weist die NO_2-Beugeschwingung noch vor den Ringverzerrungsmoden bei einer IR-Voranregung die stärkste Veränderung des Absorptionsspektrums auf. Im Fall von Rhodamin ist das vibronische OPA-Spektrum überwiegend durch das FC-Spektrum gegeben und der HT-Anteil liefert nur einen geringen Beitrag. Das vibronische TPA-Spektrum wird hingegen vollständig durch die HT-Beiträge dominiert. Eine Erklärung dafür wurde von Milojevich *et al.* geliefert, die das Verhalten auf eine Änderung der Symmetrie durch die Orbitalübergänge vom Grundzustand in den angeregten Zustand zurückführen. Aufgrund der geringen Huang-Rhys-Faktoren konnten keine signifikant VIPER-aktiven Normalmoden ermittelt werden.

Der zweite Teil der Arbeit befasst sich mit der Abschätzung der Rate des intramolekularen Energietransfers innerhalb einer Rhodamin-BODIPY-Dyade. Nach den Untersuchungen an den in Frage kommenden Rhodaminderivaten zeigt das Rho101-Derivat die höchste TPA-Aktivität. Dieses wurde zusammen mit einem BODIPY-Derivat mit Styryl-Substituenten über eine Acetylenbindung kovalent verknüpft und anschließend sowohl theoretisch als auch experimentell untersucht um den Energietransfer (excitation energy transfer, EET) zu charakterisieren.

Zeitaufgelöste spektroskopische Messungen zeigten einen ultraschnellen Energietransfer im Bereich von Femtosekunden. Damit wird die theoretische Abschätzung der EET-Raten mit Hilfe der Förster-Theorie unzureichend. Deshalb wurden Quantendynamiksimulationen mit der ML-MCTDH-Methode (Multi-Layer-Multi-Configuration Time Dependent Hartree) an einer leicht angepassten Rhodamin-BODIPY-Moleküldyade durchgeführt. Hierfür wurde ein „Linear Vibronic Coupling "(LVC) – Hamiltonoperator verwendet. Elektronische Kopplungen wurden mit Hilfe der TDC-Methode (Transition Density Cube) erhalten, vibronische Kopplungen sowie die Zustandsenergien konnten mittels elektronischer Strukturrechnungen parametrisiert werden. Die Ergebnisse zeigen anschließend, dass es sich um einen kohärenten Energietransfer handelt, der nicht durch die Förster-Theorie beschrieben werden kann. Die Simulationen reproduzieren dabei sowohl die Zeitskala auf der der Energietransfer abläuft, als auch die kohärente Superposition aus zwei Zuständen, die am Ende des Experiments ebenfalls sichtbar ist.

Das finale Projekt, das innerhalb dieser Arbeit besprochen wird, beschäftigt sich mit der theoretischen Untersuchung des photochemischen Mechanismus zur Entschützung der Photoschutzgruppe [7-(Dimethylamino)cumarin-4-yl]methyl (DEACM) im Hinblick auf verschiedene LG. Dabei wurden die Kinetiken für drei DEACM-Spezies jeweils mit Thiocyanat (-SCN), Azid (-N_3) sowie Carbonat als LG untersucht, indem Scans der Potentialhyperfläche („potential energy surface“, PES) entlang relevanter Geometrieauslenkungen in den angeregten Zuständen angefertigt wurden. Die Koordinaten entlang derer die PES der verschiedenen Systeme untersucht wurden umfassen die dissoziative DEACM-LG-Abstandskoordinate sowie den Diederwinkel der LG relativ zum Cumarin-Gerüst. In allen drei Fällen verbleibt das DEACM-Gerüst unverändert, nachdem die Anregung in den S_1 Zustand ($\pi - \pi^*$ Übergang) durch Überquerung einer entsprechenden Barriere zu einem dissoziativen Zustand führt. Dies wird möglich durch nichtadiabatische Kreuzungen mit höherliegend Zuständen. Aus den 2D „relaxed Surface Scans“geht hervor, dass die Bindungsspaltung in allen Systemen durch eine Änderung des

Diederwinkels bis hin zu einer fast senkrechten Ausrichtung der LG relativ zum DEACM ausgelöst wird. Dabei dissoziiert DEACM-SCN barrierefrei, während DEACM-N_3 und DEACM-Carb eine vergleichsweise hohe Barriere überwinden müssen, um dissoziieren zu können.

Insgesamt wurde innerhalb dieser Arbeit damit die theoretische Evaluation des VIPER-Experiments um die TPA erweitert, der Energietransfer innerhalb einer Rhodamin-BODIPY-Dyade aufgeklärt sowie der Mechanismus der Entschützung für DEACM mit verschiedenen LGs anhand der 1D und 2D PES untersucht.

PUBLICATIONS

[1] M. Asido, C. Hamerla, R. Weber, M. Horz, M. S. Niraghatam, A. Heckel, I. Burghardt, J. Wachtveitl, "Ultrafast and efficient energy transfer in a one- and two- photon sensitized rhodamine-BODIPY dyad: A perspective for broadly absorbing photocages," *Phys. Chem. Chem. Phys.* **2022**, *24*, 1795–1802.

[2] C. Hamerla, C. Neumann, K. Falahati, J. von Cosel, L. J. G. W. van Wilderen, M. S. Niraghatam, D. Kern-Michler, N. Mielke, M. Reinfelds, A. Rodrigues-Correia, A. Heckel, J. Bredenbeck, I. Burghardt, "Photochemical mechanism of DEACM uncaging: A combined time-resolved spectroscopic and computational study," *Phys. Chem. Chem. Phys.* **2020**, *22*, 13418–13430.

PUBLICATIONS TO BE SUBMITTED

[1] M. Horz, H. Vormann, H. Masood, M. S. Niraghatam, H. Brunst, D. Picconi, F. Santoro, J. Bredenbeck, I. Burghardt, "Vibrationally Promoted Electronic Resonance (VIPER) Spectroscopy of Coumarin-6 using two-photon excitation," to be submitted.

CONTENTS

LIST OF TABLES

LIST OF ABBREVIATIONS

1D	one-dimensional
2D	two-dimensional
2D-IR	two-dimensional infrared
AH	Adiabatic Hessian
AS	Adiabatic Shift
ASF	Adiabatic shifts and frequencies
BODIPY	Boron dipyromethenes
CASSCF	Complete active space self-consistent field
CC	Coupled Cluster
CI	Configuration interaction
CSM	Continuum Solvation Model
DEACM	[7-(dimethylamino)coumarin-4-yl]methyl
DEACM-Carb	[7-(dimethylamino)coumarin-4-yl]methyl carbonate
DEACM-N_3	[7-(dimethylamino)coumarin-4-yl]methyl azide
DEACM-SCN	[7-(dimethylamino)coumarin-4-yl]methyl thiocyanate
DFT	Density Functional Theory
DMA-NDBF	Dimethylamino-nitrodibenzofuran
DMSO	Dimethyl sulphoxide
DNA	Deoxyribonucleic acid
EET	Excitation Energy Transfer
EOM	Equation of Motion
ESA	Excited State Absorption
FC	Franck-Condon
FCHT	Franck-Condon-Herzberg-Teller
FCWD	Franck-Condon Weighted Density
FRET	Förster Resonance Energy Transfer
FWHM	Full Width at Half Maximum

GGA	Generalized Gradient Approach
GM	Göppert Mayer
HF	Hartree-Fock
HF-SCF	Hartree-Fock Self-consistent Field
HOMO	Highest Occupied Molecular Orbital
HT	Herzberg-Teller
HWHM	Half Width at Half Maximum
IC	Internal Conversion
IDA	Ideal Dipole Approximation
IR	Infrared
ISC	Inter-system Crossing
IVR	Intramolecular Vibrational Energy Redistribution
KS	Kohn-Sham
LCM	Linear Coupling Model
LDA	Local Density Approximation
LG	Leaving Group
LUMO	Lowest Unoccupied Molecular Orbital
LVC	Linear Vibronic Coupling
MCSCF	Multi-configuration Self-consistent Field
MCTDH	Multi-configuration Time-dependent Hartree
ML-MCTDH	Multilayer Multi-configuration Time-dependent Hartree
MO	Molecular Orbital
MP2	Møller-Plesset perturbation theory of second order
NDBF	Nitrodibenzofuran
NIR	Near-Infrared
PCM	Polarizable Continuum Model
PES	Potential Energy Surface
PPG	Photolabile Protecting Groups
QM	Quantum Mechanical
RMSD	Root Mean Square Deviation

RNA	Ribonucleic acid
SCF	Self-consistent Field
SCRF	Self-consistent Reaction Field
SERS	Surface Enhanced Raman Spectroscopy
SEHRS	Surface Enhanced Hyper-Raman Spectroscopy
SPF	Single Particle Function
TBET	Through Bond Energy Transfer
TD	Time-dependent
TDA	Tam-Dancoff Approximation
TDC	Transition Density Cubes
TDDFT	Time-dependent Density Functional Theory
TDSE	Time-dependent Schrödinger Equation
TI	Time-independent
TISE	Time-independent Schrödinger Equation
TPA	Two-photon Absorption
TPEF	Two-photon Excitation Fluorescence
UV/vis	Ultraviolet/visible
vis	Visible light
VG	Vertical Gradient
VGF	Vertical gradients and shifts
VH	Vertical Hessian
VIPER	Vibrationally Promoted Electronic Resonance

DEUTSCHE ZUSAMMENFASSUNG

Die vorliegende Arbeit gliedert sich im Wesentlichen in drei Projekte und beschäftigt sich zum einen mit der theoretischen Beschreibung des „vibrationally promoted electronic resonance (VIPER)"-Experiments, zum anderen mit dem intramolekularen Energietransfer innerhalb einer Donor-Akzeptor Dyade sowie mit den theoretischen Untersuchung der Mechanismen zur Abspaltung von drei verschiedenen Abgangsgruppen („leaving group", LG) von der Photoschutzgruppe [7-(Dimethylamino)cumarin-4-yl]methyl (DEACM). Die ersten beiden Projekte teilen dabei die initiale Anregung des jeweiligen betrachteten Systems durch einen Zwei-Photonen-Anregung. Die hierbei relevante Zwei-Photonen Absorption („Two-Photon absorption", TPA) bietet neben der intrinsischen dreidimensionalen (3D) Auflösung auch den Vorteil, dass die Eindringtiefe in Gewebe erhöht sowie der Photoschaden an biologischen Systemen durch die größere Wellenlänge verringert wird.

Beim VIPER-Experiment handelt es sich um eine erweiterte Form der zweidimensionalen Infrarotspektroskopie, bei der nach der Schwingungsanregung eine zusätzliche elektronische Anregung erfolgt. Im hier betrachteten Fall handelt es sich bei dem ultraschnellen Laserpuls der für die elektronische Anregung verantwortlich ist um einen near-infrared (NIR) Puls. Im Falle des intramolekularen Energietranfers geht es darum, eine photolabile Schutzgruppe mittels TPA abzuspalten, die eigentlich keinen aktiven Zwei-Photonen Übergang aufweist. Dazu wurde ein Donor-Fragment an die Schutzgruppe angebracht, welches Zwei-Photonen aktiv ist. Somit kann durch die Zwei-Photonen-Anregung auf dem Donor-Fragment und den anschließenden ultraschnellen Energietransfer die eigentlich Zwei-Photonen inaktive Schutzgruppe trotzdem mittels einer Zwei-Photonen-Anregung abgespalten werden.

Das VIPER-Experiment hat durch die zusätzliche elektronische Anregung den Vorteil, dass die Messbarkeit des VIPER-2DIR-Signals nicht von der Lebensdauer der Schwingungsanregung, sondern der längeren Lebensdauer der elektronischen Anregung abhängt. Durch den zusätzlichen UV/vis Puls wird so auch die Untersuchung dynamischer Prozesse auf längeren Zeitskalen mittels mehrdimensionaler Schwingungsspektroskopie möglich. Das VIPER-Experiment zählt damit zu den Methoden, die Schwächen der konventionellen 2DIR-Spektroskopie umgehen und weist eine Sequenz von drei Pulsen auf. Der erste ist ein schmalbandiger IR-Puls, der selektiv eine bestimmte Normalmode des Moleküls anregen soll. Die Lebensdauer dieser ersten Schwingungsanregung beträgt meist nur wenige Pikosekunden. Grund für das schnelle Abklingen der Anregung kann etwa die intramolekulare Schwingungsenergieumverteilung (intramolecular vibrational energy redistribution, IVR) innerhalb eines Moleküls sein.

Der zweite Puls ist ein schmalbandiger, nicht resonanter UV/Vis-Puls, der durch die Anregung in einen elektronisch angeregten Zustand den Zerfall der Schwingungsanregung des ersten Pulses verzögert. Die Wellenlänge des UV/Vis-Pulses wird hier so gewählt, dass nur das bereits durch den IR-Puls vorangeregte Sub-Ensemble auch elektronisch angeregt werden kann. Damit ist eine Anregung sehr viel selektiver möglich, was zum Beispiel von Kern-Michler *et al.* für verschiedene

Isotopenmarkierungen nachgewiesen wurde. Der zusätzliche UV/Vis-Puls erhöht nicht nur die Zeitspanne, in der ein Signal messbar ist, sondern moduliert auch die elektronischen Absorptionsspektren der Moleküle. Der letzte Puls ist ein ultrakurzer IR-Sondenpuls, der den Zustand des jeweiligen untersuchten Systems nach den beiden Anregungspulsen abfragt und mit dem ersten IR-Puls ein 2DIR-Spektrum aufzeichnet.

Der von Jan von Cosel (Goethe-Universität Frankfurt) implementierte Aufbau wurde innerhalb dieser Arbeit nun um die Untersuchung eines TPA VIPER-Experiments erweitert, wobei auch Effekte erster Ordnung, die sogenannten Herzberg-Teller (HT) Anteile, berücksichtigt wurden. Zunächst besteht der einzige Unterschied zum konventionellen VIPER-Experiment darin, dass statt dem UV/Vis-Puls im Falle der Zwei-Photonen-Anregung nun ein NIR-Puls eingesetzt wird, sodass nur mit der Absorption von zwei Photonen eine elektronische Anregung stattfinden kann. TPA ist dabei ein Prozess dritter Ordnung, der ebendiese gleichzeitige Wechselwirkung mit zwei Photonen beinhaltet, während die Ein-Photonen-Absorption (OPA) ein linearer Prozess ist, bei dem nur ein einziges Photon im UV/Vis-Bereich absorbiert wird. OPA ist linear von der Intensität des einfallenden Lasers abhängig, während die TPA proportional zum Quadrat der Lichtintensität ist. Ein Zwei-Photonen-Übergang kann als zweistufiger Prozess dargestellt werden: Ein Photon wird absorbiert, während das Molekül von seinem Ausgangszustand in einen „Zwischenzustand“angeregt wird, ein weiteres Photon wird während des Übergangs des Moleküls vom Zwischenzustand in den „Endzustand“absorbiert.

Wie auch im OPA Fall wurden im TPA Fall schwingungsaufgelöste elektronische Absorptionsspektren berechnet, um zu untersuchen, welche Normalmoden besonders für eine VIPER-Anregung geeignet sind. Die Berechnung des schwingungsaufgelösten elektronischen Absorptionsspektrums hängt von dem elektrischen Dipolmoment des Übergangs ab. Im Falle eines hellen oder stark erlaubten Übergangs ist das Übergangsdipolmoment unabhängig von den Kernkoordinaten, was zu einem Spektrum führt, das vollständig durch die Franck-Condon-Näherung beschrieben werden kann. Der Übergang im Rahmen der FC-Näherung findet vertikal unter der Annahme von stationären Kernkoordinaten statt. Für schwach erlaubte oder verbotene Übergänge spielen die Effekte erster Ordnung, die HT-Effekte, eine wichtige Rolle. Vorherige Untersuchungen von von Cosel *et al.* ergaben, dass die VIPER-Aktivität einer Normalmode, die durch den IR-Puls vorangeregt wird, eng mit der Größe der Huang-Rhys-Faktoren zusammenhängt, welche wiederum korrelieren mit der dimensionslosen Verschiebung entlang den jeweiligen Normalmoden. Diese Größe wird daher im Folgenden als Indikator für eine starke VIPER-Aktivität herangezogen.

Die erweiterte Implementierung wurde anhand zweier molekularer Systeme ausgearbeitet, bei denen es sich um Zwei-Photonen aktive Verbindungen handelt. Eines davon ist ein Derivat von Nitrodibenzofuran (NDBF), ein bekanntes Beispiel für eine photolabile Schutzgruppe (Photolabile protecting group, PPG) mit TPA-Eigenschaften, welche mittels Femtosekundenlasern abgespalten werden kann. Hier wurde eine rotverschobene Variante mit einem zusätzlichen Dimethylaminosubstituenten (Dimethylamino-Nitrodibenzofuran, DMA-NDBF) untersucht, über deren gute Eigenschaften als Zwei-Photonen aktive PPG Becker *et al.* berichteten. Die

Substitution mit einer Donor-Funktionalität erhöht den dipolaren Charakter sowie den TPA-Querschnitt des Chromophors. Das andere betrachtete Testsystem ist ein Derivat des kommerziell erhältlichen Rhodamin 101 (Rho 101). Rhodamine sind allgemein eher für ihre Anwendungen als Laserfarbstoffe bekannt, sie werden üblicherweise als Fluoreszenzmarker zum Beispiel in der Fluoreszenzmikroskopie eingesetzt.

Die TPA-Spektren im Falle des DMA-NDBF wurden auf der Grundlage des „adiabatic Hessian"Modells (AH) berechnet, bei dem das Potential des angeregten Zustands (Potential energy surface, PES) um das eigentliche Minimum des angeregten Zustands aufgespannt wird. Die schwingungsaufgelösten elektronischen Absorptionsspektren von DMA-NDBF für den Übergang vom Grundzustand zum elektronisch angeregten Zustand sind sowohl im Falle der OPA als auch für die TPA innerhalb der FC-Näherung identisch. Die HT-Beiträge haben jeweils keinen signifikanten Einfluss auf das vibronische Gesamtspektrum. Das ist allerdings erwartet, da der erste elektronisch angeregte Zustand aufgrund seiner hohen Oszillatorstärke und des ebenfalls hohen TPA-Querschnitts sowohl Ein- als auch Zwei-Photonen aktiv ist und elektronisch erlaubte Übergänge typischerweise unbedeutende HT-Beiträge aufweisen. Auf Grundlage der Huang-Rhys-Faktoren aller Normalmoden wurden eine Ringverzerrungsmode und die NO_2-Beugeschwingung untersucht. Die NO_2-Beugeschwingung weist für DMA-NDBF dabei die stärkste VIPER-Aktivität auf.

Die Berechnung der schwingungsaufgelösten elektronischen Absorptionsspektren von Rhodamin basierte dagegen auf dem „vertical gradient"(VG) Modell, bei dem die PES des angeregten Zustands um den Franck-Condon Punkt aufgespannt wird. Das liegt daran, dass im angeregten Zustand die Geometrie des Rhodamins stark von der im Grundzustand abweicht, womit eine Berechnung von Franck-Condon Überlappintegralen mit der eigentlichen Gleichgewichtsgeometrie nicht möglich ist. Die schwingungsaufgelösten elektronischen Absorptionsspektren des Rhodamins zeigen einen interessanten Kontrast zwischen dem OPA und dem TPA Fall, denn das OPA-Spektrum wird hauptsächlich durch die FC-Anteile beschrieben, während das TPA-Spektrum hingegen vollständig von den HT-Anteilen dominiert wird. Dieser Befund wurde ebenfalls von Milojevich *et al.* für das handelsübliches Rhodaminderivat Rho 6G erhalten. Sie begründen dieses Verhalten mit den Orbitalübergängen, welche den Übergang vom Grundzustand zum ersten elektronisch angeregten Zustand beschreiben. Dabei wirkt eine Seite des Xanthenrings als Elektronendonor und die andere Seite als Elektronenakzeptor, es handelt sich also um ein sogenanntes „Push-Pull "-System, welche oft nichtlineare optische Eigenschaften aufweisen.

Keine der Normalmoden in diesem Fall wies einen besonders signifikanten Huang-Rhys-Faktor und damit auch eine signifikante dimensionslose Verschiebung auf. Deshalb wurden im hochfrequenten Bereich des IR-Spektrums zwei Ringverzerrungsmoden auf ihre potenzielle VIPER-Aktivität untersucht. Die Voranregung der Ringmoden zeigt aber erwartungsgemäß keine signifikante Auswirkung auf die vibronischen Spektren, da sich die Intensitäten der rotverschobenen VIPER-Übergänge als sehr gering erwiesen.

Der zweite Teil dieser Dissertation befasst sich mit dem intramolekularen Energietransfer innerhalb einer Rhodamin-BODIPY-Dyade. Das Rhodamin-Fragment

spielt dabei die Rolle einer Donor-Gruppe und das BODIPY die Rolle eines Akzeptors. Die Übertragung von Anregungsenergie (Excitation energy transfer, EET) erfolgt innerhalb eines schwachen Kopplungsregimes, sodass die Wechselwirkung mit Hilfe eines störungstheoretischen Ansatzes untersucht werden kann. Zunächst wird versucht, den Energietransfer mittels der Förster-Theorie für Donor-Akzeptor-Paare zu beschreiben, wobei die Wechselwirkung als Dipol-Dipol-Wechselwirkung beschrieben wird. Dabei ist die Rate für den strahlungslosen Energietransfer proportional zu der inversen sechsten Potenz des Abstands zwischen Donor- und Akzeptor-Fragment.

Eine Möglichkeit zur Berechnung der elektronischen Dipol-Dipol-Kopplung zwischen den Donor- und Akzeptorgruppen ist die „Transition Density Cube"(TDC) Methode. Bei der TDC-Methode wird die vollständige dreidimensionale Übergangsdichte verwendet. Die Übergangsdichten für die elektronischen Zustände mit Orbitalübergängen innerhalb der jeweiligen Donor- und Akzeptor-Fragmente können durch quantenchemische Berechnungen erzeugt werden. Die Coulombwechselwirkung zwischen den Donor- und Akzeptor-Übergangsdichten ergibt anschließend die elektronische Kopplung. Neben der Berechnung der Kopplung wird auch der spektrale Überlapp zwischen dem vibronischen Emissionsspektrum der Donorgruppe und dem Absorptionsspektrum des Akzeptor-Fragments benötigt. Die FRET-Rate ist schließlich proportional zum Quadrat der Kopplung und dem spektralen Überlappintegral.

Es wurden innerhalb des Projekts zunächst einige Rhodaminderivate, abgeleitet von den kommerziell erhältlichen Rho 110, Rho B, Rho 6G und Rho 101, auf ihrer Zwei-Photonen-Absorptionsquerschnitte untersucht. Der Einfachheit halber werden die Derivate der Rhodamine im weiteren Text als Rho1, Rho2, Rho3 und Rho4 bezeichnet. In Übereinstimmung mit den Fluoreszenzmessungen, die in Zusammenarbeit mit Prof. Josef Wachtveitl (Goethe Universität Frankfurt) durchgeführt wurden, bestätigen die berechneten Zwei-Photonen Eigenschaften, dass Rho4 die höchste Zwei-Photonen Aktivität aufweist, gefolgt von Rho1 und Rho2. Rho3 hingegen weist die geringste Zwei-Photonen Aktivität auf, da sein TPA-Querschnitt sowohl in theoretischen Beschreibungen als auch in experimentellen Messungen am geringsten ist.

BODIPY ist die Abkürzung für Bor-Dipyrromethen, welches eine wichtige Klasse von organischen Fluorophoren darstellt. Für die hier untersuchte Klasse von Antennensystemen wurden zwei BODIPY-Derivate als Akzeptor untersucht. Bei einem handelt es sich um das klassische BODIPY (im Weiteren bezeichnet als BODIPY1), das über eine Acetylenbindung mit Rho1 verbunden wurde. Problematisch ist hierbei, dass das Absorptionsmaximum von BODIPY1 im Experiment eine kleinere Wellenlänge aufwies als das des Rhodamins. Um dies zu umgehen wurde ein anderes BODIPY-Derivat mit konjugierten ortho-Methoxyphenyl-Substituenten (im Weiteren bezeichnet als BODIPY2) untersucht, dessen Absorptionsmaximum rotverschoben ist. BODIPY2 wurde über denselben kovalenten Acetylenlinker mit dem Rho4-Fragment verknüpft. In dieser molekularen Dyade hat das Rho4 als Donorfunktionalität nun eine höhere Anregungsenergie als der substituierte BODIPY2-Akzeptor.

Aus der Sicht der Synthese stellte die Entwicklung eines geeigneten Linkers zur Verbindung der Farbstoffe eine grundlegende Herausforderung dar. Um die Bil-

dung von Aggregaten, das sogenannte „π-stacking "zu vermeiden, wurde ein kovalenter Linker eingeführt. Dieser Linker ist auch für die Untersuchung des Energietransfers relevant, da er den Mechanismus des Energietransfers beeinflussen kann. Dieser kann zum Beispiel „durch den Raum"in Übereinstimmung mit der Förster-Theorie oder „durch die Bindung"erfolgen.

Die Berechnung der elektronischen Struktur zeigt angeregte Zustände mit sehr lokalisierten Orbitalübergängen innerhalb der Fragmente BODIPY1 und Rho1 sowie BODIPY2 und Rho4. Die Orbitale innerhalb der Dyaden ähneln denen in den isolierten BODIPY1 und Rho1 sowie BODIPY2 und Rho4 Systemen. Der Zwei-Photonenaktive angeregte Zustand des isolierten Rho1 beziehungsweise Rho4 spiegelt sich jeweils als ein höherer angeregter Zustand in der Rho1-BODIPY1-Dyade beziehungsweise der Rho4-BODIPY2-Dyade wider. Auf dieser Grundlage wird angenommen, dass eine Anregung mit einem TPA-Puls zunächst in den höheren, Zwei-Photonen aktiven Zustand, führt. Danach erfolgt eine „Internal Conversion"(IC) innerhalb der auf dem Rhodamin-Fragment lokalisierten Zustände. Die Energieübertragung von Rho1 auf das BODIPY1-Fragment beziehungsweise von Rho4 auf BODIPY2 findet im Anschluss statt.

Die Zeitskalen eines Energietransfers, die mittels spektralen Überlapps und elektronischer TDC-Kopplungen zwischen den lokalisierten angeregten Zuständen in der Dyade innerhalb der Förster-Theorie berechnet wurden, liegen im Falle der Rho1-BODIPY1-Dyade zwischen 80 fs und 10 ps. Im Fall der zweiten Dyade Rho4-BODIPY2-OH liegen die Zeitskalen für den Energietransfer vom Rho4 zum BODIPY2 deutlich höher zwischen 5 ps und 1 ns. Zeitaufgelöste spektroskopische Messungen an der Rho4-BODIPY2-Dyade zeigen allerdings einen ultraschnellen intramolekularen Energietransfer vom Rho4 zum BODIPY2 auf einer Zeitskala von 150 – 500 fs.

Da der hier gemessene Energietransfer auf dieser Zeitskala nahelegt, dass die Förster-Theorie nicht geeignet ist um den Prozess zu beschreiben, wurden quantendynamische Untersuchungen an einer Rho1-BODIPY1-Dyade durchgeführt. Unter Verwendung der ML-MCTDH-Methode (Multilayer-Multiconfiguration Time Dependent Hartree) und eines „Linear Vibronic Coupling"-Hamiltonian (LVC) wurden so Simulationen für den Energietransfer nach der IC durchgeführt. Dabei wurde ein Zerfall der Population des Donorzustandes festgestellt, während der angeregte Zustand, der auf dem Akzeptor-Fragment BODIPY1 lokalisiert ist, populiert wird. Dieser kohärente Energietransfer findet auf einer Zeitskala von etwa 200 fs statt. Weiterhin führen die Simulationen zu einer stationären Superposition beider Zustände, welche auch im Experiment zu sehen ist. Das wird unter anderem durch den nicht verschwindenden Realteil der Kohärenz deutlich. Der Imaginärteil, d.h. die transiente Kohärenz, bestimmt dagegen den Energietransfer und zerfällt auf einer analogen Zeitskala. Daher kann dieser ultraschnelle Energietransfer als kohärenter Energietransfers beschrieben werden, während die Förster-Theorie den ultraschnellen Transfer nicht erklären kann.

Der letzte Teil dieser Arbeit befasst sich mit einer theoretischen Studie über die photochemischen Mechanismen der Entschützung der DEACM Photoschutzgruppe, wobei drei verschiedenen LG untersucht wurden, ein Thiocyanat (-SCN), ein Azid (-N_3) sowie ein Carbonat. Um die LG-spezifischen Kinetiken für die drei verschiedenen DEACM-Varianten zu untersuchen, wurden Scans der Potentialhyper-

flächen („potential energy surface“, PES) der angeregten Zustände mittels TDDFT-Rechnungen angefertigt. Berücksichtigt wurden dabei die dissoziative DEACM-LG-Abstandskoordinate und der Diederwinkel zwischen LG und dem Cumarin-Gerüst. Hier wurde deutlich, dass ein Übergang durch eine Kreuzung zwischen dem ursprünglich angeregten S_1-Zustand ($\pi - \pi^*$ Anregung), der auf dem DEACM-Teil lokalisiert ist und einem dissoziativen Zustand, der auf der LG lokalisiert ist, für die beobachtete Abspaltung der LG verantwortlich ist. Dieser wird durch eine Änderung der beiden betrachteten Koordinaten vermittelt. Aus den 1D- und 2D-PES-Scans geht hervor, dass die DEACM-SCN-Spezies eine barrierefreie Dissoziation erfährt, während die DEACM-N_3- und DEACM-Carb Varianten eine mehr oder weniger steile Energiebarriere überwinden müssen und somit langsamer dissoziieren.

Insgesamt konnten damit im Rahmen dieser Arbeit zwei Projekte innerhalb der Zwei-Photonen Absorption bearbeitet werden. Die Implementierung der TPA in die theoretische Evaluation des VIPER-Experiments und der VIPER-Aktivität hat gezeigt, dass die TPA durchaus einen positiven Einfluss auf die Effizienz der VIPER Anregung haben kann. Für das VIPER-Experiment können nun also geeignetere Zwei-Photonen-aktive PPGs entwickelt und auf ihre potenziellen Anwendungen bei der Entschützung untersucht werden. Das ist vor allem für biologische oder medizinische Anwendungen vorteilhaft, da hier durch den NIR-Laser die Gefahren, die die konventionelle UV/Vis-Anregung für das Molekül mit sich bringt, umgangen werden, was zu einer geringeren Schädigung des Systems führt. Außerdem konnte der Energietransfer innerhalb einer neuen Klasse von TPA-Antennensystemen aufgeklärt werden, womit eine Interpretation der spektroskopischen Messungen des Systems und eine Weiterentwicklung im Bezug auf die Effizienz des Energietransfers möglich sind. Weiterhin könnten im letzten Projekt die photochemischen Mechanismen der Abspaltung von drei unterschiedlichen LG von der Photoschutzgruppe DEACM aufgeklärt werden. Dabei zeigte sich, dass trotz unterschiedlicher Zeitskalen grundsätzich die gleichen Geometrieänderungen für die Abspaltung verantwortlich sind. Die Erkenntnisse über die Mechanismen zur Abspaltung der LG werden in Zukunft beim Design und der Weiterentwicklung dieser Klasse von Photoschutzgruppen helfen.

1 INTRODUCTION

Although the concept of two-photon absorption (TPA) was first proposed by Maria Göppert-Mayer way back in 1931 [54], it was only until the advent of lasers three decades later that a demonstration of TPA experiment could be achieved [64]. Since then, owing to the successive revolutions in the development of lasers, the possibilities today extend not just to two-photon but towards higher-order multi-photon excitations as well. Research on non-linear optical spectroscopy has been very intense for the past thirty years. Therefore, two-photon absorption continues to be an area of extensive investigation due to its wide-ranging applications.

Achieving better efficiencies of uncaging phenomena and the development of suitable photolabile protecting groups for this purpose has always remained a formidable challenge for the spectroscopists and the organic chemists. Two-photon absorption improves the efficiency for these purposes in which a molecular species can be excited by simultaneous absorption of two photons. Therefore, search for photolabile protecting groups (PPG) or dyes which have very good TPA characteristics becomes extremely important. Rhodamines are well-known for these desired TPA properties. The rhodamine moieties are often selected as a suitable donor fragment for the development of dyads in order to achieve fast energy transfer.

The objective of the work is to extend the avenues of theoretical investigations of Vibrationally Promoted Electronic Resonance (VIPER) experiment and the photocages exhibiting intramolecular energy transfer to TPA. Both of the concepts delve also into the vibronic effects in the calculation of absorption spectra. These phenomena occur in the range of picosecond to femtosecond timescales.

In continuation of the research on VIPER experiment by Jan von Cosel [62] in which theoretical investigations have been extensively carried out on coumarin based dyes, the scope of this experiment is being extended to TPA as depicted in fig. 1. An experiment in this regard has already been reported by Mastron and Tokmakoff [88] where two-photon-excited fluorescence with a femtosecond near-IR (NIR) pulse detection was employed. VIPER is a non-linear spectroscopic technique which consists of a sequence of IR and Vis pulses. In collaboration with Prof. Bredenbeck (Goethe University Frankfurt), who is one of the experts in mixed IR/UV/vis two-dimensional spectroscopy, theoretical investigations have been performed on some two-photon-active molecular systems.

The VIPER scheme inducts the sequence of the IR and UV/vis or a two-photon excitation to probe the vibrational dynamics of a molecular system in the ground and excited electronic states. If the UV/vis pulse helps in extending the lifetimes to study dynamics in the excited states, a two-photon excitation probably with a NIR pulse could serve as an alternative method of excitation to the excited electronic states also avoiding the possible side-effects to the molecule from the UV/vis pulse. The theoretical investigations also now account for the computation of the first-order effects which are dependent on the nuclear coordinates. These first-order effects can play a significant role and vary accordingly with the electronically weakly allowed or forbidden transitions. Also, as investigated earlier, the effects of pre-

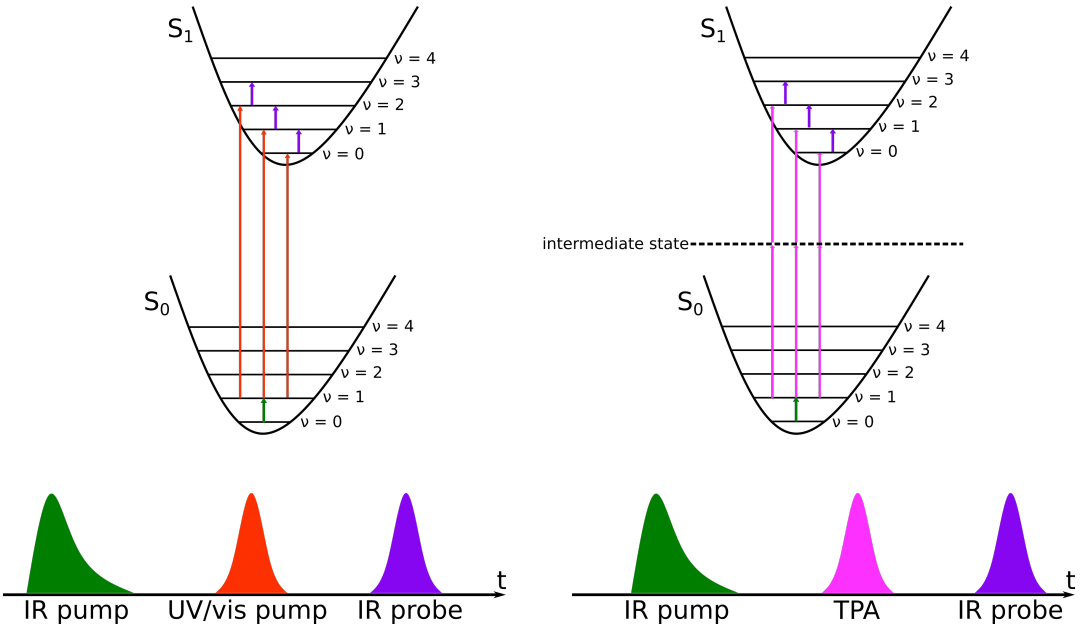

Figure 1: Bottom left: The VIPER pulse sequence consisting of IR pump, UV/vis pump and IR probe pulses. Top left: Vibronic level scheme depicting the corresponding transitions for one-photon VIPER experiment. Bottom right: The VIPER pulse sequence consisting of the IR pump, TPA and IR probe pulses. Top right: Vibronic level scheme depicting the corresponding transitions for two-photon VIPER experiment.

excitation of a specific normal mode of vibration with a distinct IR pulse are also studied.

Cassette molecules composed of rhodamine and BODIPY dyes as donor and acceptor groups is another important area of interest for excitation energy transfer (EET) processes. Attempts are made to improve efficiency by first exciting the donor group through TPA and then subsequently transfering energy to the acceptor group. Fig. 2 illustrates the scheme of intramolecular energy transfer initiated by a two-photon excitation. Based on the available literature, the energy transfer process is expected to be ultrafast with the timescales ranging from femto to picoseconds. In collaboration with Prof. Heckel for organic synthesis as well as Prof. Wachtveitl for time-resolved spectroscopic measurements at Goethe University Frankfurt, this work aims to design the molecular dyads which facilitate efficient and fast energy transfer through a suitable linker. Linking the donor and acceptor dyes is a commonly encountered design problem.

The conventional approach to determine the mechanism of energy transfer is that of Förster resonance energy transfer (FRET). The scheme of estimation of EET rate involves calculation of couplings between donor and acceptor groups through dipole-dipole approximation. A more accurate method of evaluating the coupling between the donor and acceptor groups is known as transition density cube (TDC) method [7, 31, 71] which is based on a numerical grid representation of the transition densities. Then the estimation of EET rate also depends on the extent of the overlap between the emission spectra of the donor group and the absorption spectra of the acceptor group. Quantum dynamics simulations through the multi-layer

multi-configuration time-dependent Hartree (ML-MCTDH) method is able to provide a more accurate explanation to the phenomenon of ultrafast energy transfer.

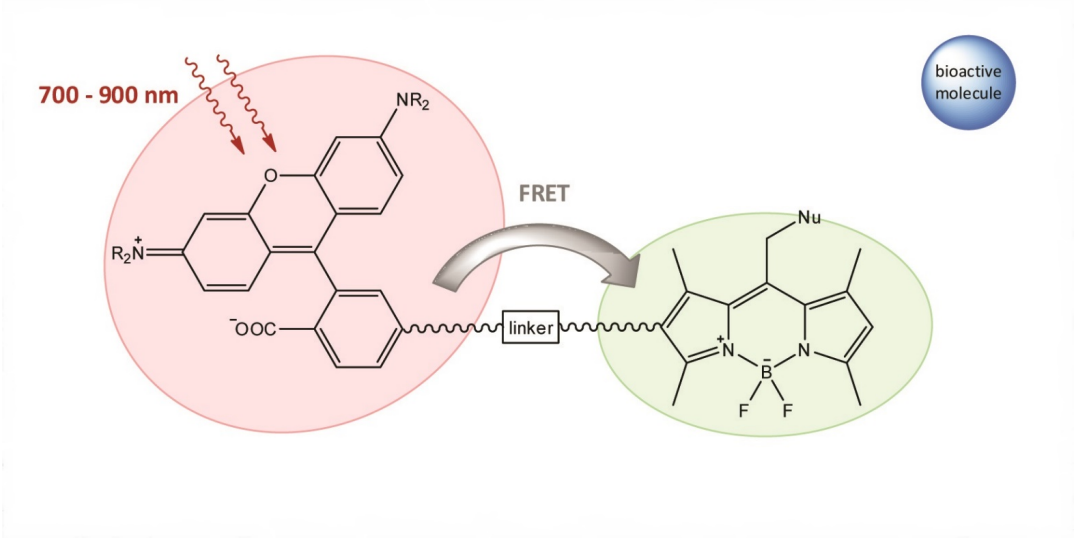

Figure 2: Schematic illustration of intramolecular energy transfer within a rhodamine-BODIPY dyad.

To design photocages for their potential applications, the extent of their regioselectivity and temporal reaction control through light-induced activation plays the most important role. Diving deeper into the functionalities of PPGs, an interesting computational study is performed specifically on [7-(dimethylamino)coumarin-4-yl]methyl (DEACM) class of photocages. The DEACM photocages have been recently explored for red-shifted absorption [47] and two-photon activation applications [58]. The cleavage of the LG in the excited state is probed by performing the one-dimensional (1D) and two-dimensional (2D) potential energy surface (PES) scans with the help of time-dependent density functional (TDDFT) methods. The characterization of photocleavage pathways are also supported by the time-resolved spectroscopic analysis in collaboration with Prof. Bredenbeck.

2 THEORETICAL BACKGROUND

This chapter aims to describe the quantum chemical methods which will lay the foundation for the computational investigations for the VIPER and EET experiments with TPA. Interactions between atoms and molecules through the valence electrons forms the core of chemistry. Electronic structure theory provides the physical and mathematical description of these interactions. Numerous textbooks of quantum mechanics and quantum chemistry give a clear and detailed analysis of the theoretical methods in order to understand easily [30, 63, 127].

2.1 SEPARATION OF ELECTRONIC AND NUCLEAR MOTION: BORN-OPPENHEIMER APPROXIMATION

The final postulate of quantum mechanics illustrates the time evolution of the wavefunction according to the time-dependent Schrödinger equation (TDSE). The crux of electronic structure theory calculations revolves around solving the TDSE:

$$i\hbar\frac{\partial}{\partial t}\Psi(\mathbf{r},\mathbf{R},t) = \hat{H}(\mathbf{r},\mathbf{R})\Psi(\mathbf{r},\mathbf{R},t) \tag{1}$$

$\mathbf{r}$ and $\mathbf{R}$ refer to the electronic and nuclear coordinates respectively. The Hamiltonian $\hat{H}$ of a molecule with N_e electrons and N_n nuclei in atomic units is defined as

$$\begin{aligned}\hat{H}(\mathbf{r},\mathbf{R}) = &-\sum_{i=1}^{N_e}\frac{1}{2}\nabla_i^2 - \sum_{A=1}^{N_n}\frac{1}{2M_A}\nabla_A^2 - \sum_{i=1}^{N_e}\sum_{A=1}^{N_n}\frac{Z_A}{r_{iA}} + \sum_{i=1}^{N_e}\sum_{j>i}^{N_e}\frac{1}{r_{ij}} \\ &+ \sum_{A=1}^{N_n}\sum_{B>A}^{N_n}\frac{Z_A Z_B}{r_{AB}} \\ &= \hat{T}_e + \hat{T}_N + \hat{V}_{eN} + \hat{V}_{ee} + \hat{V}_{NN}\end{aligned} \tag{2}$$

where $r_{ij} = |\mathbf{r}_i - \mathbf{r}_j|$ is the distance between electrons i and j, $r_{iA} = |\mathbf{r}_i - \mathbf{R}_A|$ is the distance between electron i and nucleus A and $r_{AB} = |\mathbf{R}_A - \mathbf{R}_B|$ is the distance between nuclei A and B. This Hamiltonian consists of the terms respectively for the kinetic energy of electrons, nuclei as well as the electron-electron, nuclear-nuclear and electron-nuclear potential interactions.

$\hat{H}$ does not contain time explicitly and therefore the method of separation of variables can be applied. The total wavefunction can then be split through the product form: $\Psi(\mathbf{r},\mathbf{R},t) = \psi(\mathbf{r},\mathbf{R})\chi(t)$. Substituting this product form back into the TDSE and dividing both sides by $\psi(\mathbf{r},\mathbf{R})\chi(t)$ [91],

$$\frac{1}{\psi(\mathbf{r},\mathbf{R})}\hat{H}\psi(\mathbf{r},\mathbf{R}) = \frac{i\hbar}{\chi(t)}\frac{d\chi(t)}{dt} \tag{3}$$

Now the left-hand side is a function of position x only and the right-hand side is a function of t only. Hence, both sides must equal a constant. Denoting the separation constant by E, eq. 1 becomes

$$\hat{H}\psi(\mathbf{r},\mathbf{R}) = E\psi(\mathbf{r},\mathbf{R}) \tag{4}$$

which could be called as the time-independent Schrödinger equation (TISE). And

$$\frac{d\chi(t)}{dt} = -\frac{i}{\hbar}E\chi(t) \tag{5}$$

Integrating eq. 5 gives

$$\chi(t) = e^{-\frac{i}{\hbar}Et} \tag{6}$$

Therefore $\Psi(\mathbf{r},\mathbf{R},t)$ is of the form

$$\Psi(\mathbf{r},\mathbf{R},t) = \psi(\mathbf{r},\mathbf{R})e^{-\frac{i}{\hbar}Et} \tag{7}$$

Eq. 4 is in the form of an eigenvalue equation where $\psi(\mathbf{r},\mathbf{R})$ is the eigenfunction of the Hamiltonian $\hat{H}$ and E is the eigenvalue. The *electronic* TISE can simplify this equation by keeping the positions of the nuclei fixed

$$\hat{H}_e\psi_e(\mathbf{r};\mathbf{R}) = E(\mathbf{R})\psi_e(\mathbf{r};\mathbf{R}) \tag{8}$$

The wavefunction for the electron $\psi_e(\mathbf{r};\mathbf{R})$ is a function of its position r and in turn only parametrically dependent on the nuclear positions R [128]. The electronic Hamiltonian $\hat{H}_e$ consists of only the terms dependent on the electronic positions, $\hat{H}_e = \hat{T}_e + \hat{V}_{eN} + \hat{V}_{ee}$. The total wavefunction is finally a product of the electronic and nuclear wavefunctions: $\psi(\mathbf{r},\mathbf{R}) = \psi_e(\mathbf{r};\mathbf{R})\chi(\mathbf{R})$.

Inserting this *ansatz* for the total wavefunction into the full TISE leads to terms partially derived from the electronic wavefunction $\psi_e(\mathbf{r};\mathbf{R})$ with respect to the nuclear coordinates $\mathbf{R}$ scaled with the inverse nuclear mass. The magnitude of these terms is very small since nuclei are far too heavier than electrons ($\frac{m_p}{m_e} \approx 2000$). In the *Born-Oppenheimer approximation* or the *adiabatic approximation*, these terms are neglected in the TISE. The motion of the electrons and the nuclei is decoupled in this approximation and the final term V_{NN} in eq. 2 represents the repulsive interaction between the nuclei. The potential with respect to the position of the nuclei leads to the generation of the potential energy surfaces (PES). The Born-Oppenheimer approximation works well for the equilibrium geometries where the derivative of the electronic wavefunction with respect to the nuclear coordinates is small and the electronic states are quite far apart in energy. The Born-Oppenheimer breaks down when the states are closer to each other in energy and the derivatives become very strong. In this work, only those cases in which the Born-Oppenheimer is valid would be considered.

2.2 HARTREE-FOCK THEORY

Following up on the breakdown of the approach to the solution of the Schrödinger equation for electrons and nuclei combined towards the solution of the electronic

Schrödinger equation, an *ab initio* method now concentrates on calculating the electronic wavefunction and the electronic energy. The presence of electron-electron repulsion is the main complication in all electronic structure calculations. Consider first a system of noninteracting electrons. The Hamiltonian reads

$$H^0 = \sum_{i=1}^{N_e} \hat{h}_i \tag{9}$$

where $\hat{h}_i$ is the one-electron Hamiltonian describing the kinetic energy and potential energy for electron i. An orbital is defined as one-electron wavefunction $\psi(r)$ and an electron can either have spin $\alpha(\omega)$ (spin up $\uparrow$) or $\beta(\omega)$ (spin down $\downarrow$). Therefore, a *spin orbital* $\chi(x)$ would then be a wavefunction for an electron that describes both its spatial distribution and its spin, where x indicates both space and spin coordinates.

$$\chi(x) = \begin{cases} \psi(r)\alpha(\omega) \\ \text{or} \\ \psi(r)\beta(\omega) \end{cases} \tag{10}$$

The total wavefunction $\Psi(x)$ is a product of one-electron wavefunctions also termed as *Hartree product*.

$$\Psi(x) = \prod_i \chi_i(x_i) \tag{11}$$

Electrons are categorized as *fermions*, i.e., particles with half-integral spin. So the total wavefunction has to satisfy two requirements:

1. They are indistinguishable implying that the total probability density does not change upon interchange of any two electrons:

$$|\Psi(x_1, \dots, x_i, \dots, x_j, \dots, x_N)|^2 \stackrel{!}{=} |\Psi(x_1, \dots, x_j, \dots, x_i \dots, x_N)|^2 \tag{12}$$

2. The antisymmetry with respect to the interchange of any two electrons:

$$\Psi(x_1, \dots, x_i, \dots, x_j, \dots, x_N) = -\Psi(x_1, \dots, x_j, \dots, x_i, \dots, x_N) \tag{13}$$

   This requirement is famously known as *Pauli exclusion principle* which states that no more than one electron can occupy a spin orbital.

Evidently, the Hartree product in eq. 11 is unable to obey these requirements. To ensure the fufillment of these requirements, the overall wavefunction can be written in the form of *Slater determinant*.

$$\begin{aligned} |\Psi(x_1, \dots, x_N)\rangle &= \frac{1}{\sqrt{N!}} \begin{vmatrix} \chi_1(x_1) & \chi_2(x_2) & \cdots & \chi_N(x_1) \\ \chi_1(x_2) & \chi_2(x_2) & \cdots & \chi_N(x_2) \\ \vdots & \vdots & \ddots & \vdots \\ \chi_1(x_N) & \chi_2(x_N) & \cdots & \chi_N(x_N) \end{vmatrix} \\ &= |\chi_1 \chi_2 \cdots \chi_N\rangle \end{aligned} \tag{14}$$

The last expression is a short-hand notation. With the introduction of the Slater determinant, the derivation of Hartree-Fock (HF) theory is set to proceed by formulating a well-defined wavefunction for a N_e electron system. According to the variation principle, any normalized wavefunction subject to the appropriate boundary conditions yields an energy (expectation value of the Hamiltonian) that is an upper bound to the exact ground state energy and the best spin-orbitals are those which minimize the electronic energy.

$$E_0 = \langle \Psi_0 | \hat{H} | \Psi_0 \rangle = \sum_{i=1}^{N} \langle i | \hat{h} | i \rangle + \frac{1}{2} \sum_{i=1}^{N} \sum_{j=1}^{N} \langle ij | ij \rangle - \langle ij | ji \rangle \tag{15}$$

where the core one-electron Hamiltonian $\hat{h}$ definition involves its kinetic energy and the potential energy for attraction to the nuclei.

$$\hat{h}(1) = -\frac{1}{2}\nabla_1^2 - \sum_{A=1}^{N_n} \frac{Z_A}{r_{1A}} \tag{16}$$

The Coulomb operator $\hat{J}$ (representing the term $\langle ij|ij \rangle$) and the exchange operator $\hat{K}$ (representing the term $\langle ij|ji \rangle$) act on a spin orbital χ_i in the following way:

$$\hat{J}_j(1)\chi_i(x_1) = \left[\int dx_2 \chi_j^*(x_2) \frac{1}{r_{12}} \chi_j(x_2) \right] \chi_i(x_1) \tag{17}$$

$$\hat{K}_j(1)\chi_i(x_1) = \left[\int dx_2 \chi_j^*(x_2) \frac{1}{r_{12}} \chi_i(x_2) \right] \chi_j(x_1) \tag{18}$$

A Fock operator can now be defined by including the above terms

$$\hat{f}(1) = \hat{h}(1) + \sum_{j=1}^{N} \left[\hat{J}_j(1) - \hat{K}_j(1) \right] \tag{19}$$

Finally the HF equation can be arrived at as an eigenvalue equation:

$$\hat{f}\chi_i(x_1) = \epsilon_i \chi_i(x_1) \tag{20}$$

Although eq. 20 could be written as an eigenvalue equation, the Fock operator has a functional dependence through the Coulomb and exchange operators on the desired spin orbitals χ_i. Hence, the HF equations are actually nonlinear equations and will have to be solved by iterative procedures. Solution is reached through the following steps:

1. An intial wavefunction i.e., an *inital guess* for the spin orbitals is created followed by the construction of the Fock matrix.
2. Fock matrix is diagonalized leading to a new set of spin orbitals and the eigenvalues of the first iteration.
3. These new spin orbitals are used to contruct a new Fock matrix and the process repeats until convergence is achieved meaning that the new spin orbitals obtained equal the ones from that of the previous iteration.

This iterative procedure is most commonly referred to as the self-consistent field (SCF) method. This SCF approach is relatively straightforward for atoms as the HF equations can be solved numerically for their spherical symmetry. However, in case of molecular orbitals (MO) matrix manipulations are used to overcome the complexities in obtaining the numerical solutions. To develop eq. 20, a set of K known basis functions $\{\phi_\mu(r)|\mu = 1, 2, \dots, K\}$ can be introduced and the spin orbitals can be expanded as a linear combination of these basis functions:

$$\psi_i(r) = \sum_{\mu=1}^{K} C_{\mu i}\phi_\mu(r) \tag{21}$$

From here, the problem of calculating the HF MOs reduces to the problem of computing the set of expansion coefficients $C_{\mu i}$. Substituting the expansion in the above equation into the HF equation (eq. 20):

$$f(1)\sum_\nu C_{\nu i}\phi_\nu(1) = \epsilon_i \sum_\nu C_{\nu i}\phi_\nu(1) \tag{22}$$

Multiplying both sides of the equation by $\phi^*_\mu(1)$ and intergrating over all space

$$\sum_\nu C_{\nu i}\int d\mathbf{r}_1 \phi^*_\mu(1)\hat{f}(1)\phi_\nu(1) = \epsilon_i \sum_\nu C_{\nu i}\int d\mathbf{r}_1 \phi^*_\mu(1)\phi_\nu(1) \tag{23}$$

Two matrices can be defined:

1. The overlap matrix

$$S_{\mu\nu} = \int d\mathbf{r}_1 \phi^*_\mu(1)\phi_\nu(1) = \langle\phi_\mu|\phi_\nu\rangle \tag{24}$$

2. The Fock matrix

$$F_{\mu\nu} = \int d\mathbf{r}_1 \phi^*_\mu(1)\hat{f}(1)\phi_\nu(1) = \langle\phi_\mu|\hat{f}|\phi_\nu\rangle \tag{25}$$

The integrated HF equation with the definitions of $F_{\mu\nu}$ and $S_{\mu\nu}$ can now be written as

$$\sum_{\nu=1}^{K} F_{\mu\nu}C_{\nu i} = \epsilon_i \sum_{\nu=1}^{K} S_{\mu\nu}C_{\nu i} \qquad \text{or} \qquad \mathbf{FC} = \epsilon\mathbf{SC} \tag{26}$$

known popularly as Roothaan equations based on the matrix techniques introduced by C.C.J. Roothaan in 1951 for closed shell systems.

2.3 ELECTRON CORRELATION: POST HARTREE-FOCK METHODS

The HF ground-state wavefunction is still not the 'exact' wavefunction since it relies on electron being in motion in the average field of the other electrons. It still remains an approximation as the Coulombic interactions between the electrons or the electron-electron correlations are not taken into account. To improve upon this,

the exact ground-state wavefunction can be expressed as a linear combination of all possible N_e-electron Slater determinants:

$$|\psi\rangle = c_0 |\psi_0\rangle + \sum_{a,p} c_a^p \psi_a^p + \sum_{\substack{a<b \\ p<q}} c_{ab}^{pq} \psi_{ab}^{pq} + \sum_{\substack{a<b<c \\ p<q<r}} c_{abc}^{pqr} \psi_{abc}^{pqr} + \cdots \tag{27}$$

where the c's are expansion coefficients and the sum over all unique pairs of spinorbitals in doubly, triply excited determinants and so on are summed over by the limits in the summation indices ($a < b$ and so on). This expression of the wavefunction is called configuration interaction (CI), which becomes exact in the limit that all excitations are taken into consideration and accounts for the electron correlation effects neglected in the HF method. The energy associated with the exact ground state wavefunction of the form of eq. 27 which represents the effects of explicit electron correlation is the exact non-relativistic ground-state energy (within the Born-Oppenheimer approximation). The *correlation energy* is then the difference between this exact energy and the HF limit.

In the CI methods, the expansion coefficients c's are determined through initial HF-SCF calculation and held fixed in the subsequent CI calculation. Beyond CI, there are several post-HF methods [87] on which a lot has been worked upon for years and whose development is still going on.

1. The multiconfigurational self-consistent field (MCSCF) method and its more specific scheme, the complete active-space self-consistent field (CASSCF) method in which the spin orbitals and the coefficients are variationally optimized simultaneously. The spatial wavefunctions are respectively divided into the sets of inactive, virtual and active orbitals.

2. The Møller-Plesset perturbation theory of second order (MP2) method takes the zero-order Hamiltonian from the Fock operators of the HF-SCF method and the other part of the full Hamiltonian as a perturbation which accounts for the electron-electron interaction. With respect to this perturbation, there is a series expansion of the wavefunction and the energy. This results in the second-order energy correction which is an improvement over the HF energy.

3. The coupled cluster (CC) method is similar to CI, the improvisation being the inclusion of single, double and higher excitations. This sophistication leads to enormous increase in computational cost and its applications are limited to small systems [30, 63, 127].

2.4 DENSITY FUNCTIONAL THEORY

Density functional theory (DFT) proposes to replace the N_e-electron wavefunction with the one-electron density $\rho(r)$. This approach uses the electron density as a single three-dimensional function for the N_e-electron molecule with no constraints due to permutation symmetry [69]. Initially in the development of Thomas-Fermi method for atoms [42, 131], the electronic energy E is treated as a functional of the electron density consisting of the kinetic energy, the electron-nuclear attraction, the coulombic and exchange interactions, respectively.

$$E[\rho] = T[\rho] + V_{en}[\rho] + \underbrace{J[\rho] + K[\rho]}_{V_{ee}[\rho]} \tag{28}$$

Here, the electron-nuclear interaction, $V_{en}[\rho] = \sum_{k}^{N_n} \int \frac{Z_k \rho(\mathbf{r})}{|\mathbf{r}-\mathbf{r}_k|} d\mathbf{r}$, the coulombic interaction, $J[\rho] = \frac{1}{2} \iint \frac{\rho(\mathbf{r}),\rho(\mathbf{r}')}{|\mathbf{r}-\mathbf{r}'|} d\mathbf{r}d\mathbf{r}'$, the exchange interaction $K[\rho] = \frac{1}{2} \iint \frac{\rho(\mathbf{r},\mathbf{r}')^2}{|\mathbf{r}-\mathbf{r}'|} d\mathbf{r}d\mathbf{r}'$. For a given function $\rho(\mathbf{r})$, there is a unique corresponding energy.

The Hohenberg-Kohn existence theorem formulates that the electron density uniquely determines the ground-state energy and all other ground-state electronic properties [61]. With this, it becomes possible to express the ground-state energy of a molecule as a functional of the ground-state electron density

$$E[\rho] = \overbrace{T[\rho] + V_{ee}[\rho]}^{E_{HK}[\rho]} + \int \rho(\mathbf{r}) v(\mathbf{r}) d\mathbf{r} \tag{29}$$

The next Hohenberg-Kohn variational theorem imposes the exact ground-state energy of the molecule as an upper-bound to the energy functional $E_0[\rho']$ for a trial density function $\rho'(\mathbf{r})$. Because of the complexity in expressing the contributions of kinetic and exchange potentials in terms of density, the Thomas-Fermi method has limitations for practical purposes. Kohn and Sham provided a specific guidance to the development of DFT with the re-introduction of orbitals[70]. They considered a hypothetical reference system consisting of N_e non-interacting electrons in an external potential. The ground-state wavefunction of the reference system is represented by the Slater determinant:

$$\Psi_{ref} = ||\chi_1^{KS}(x_1)\chi_2^{KS}(x_2)\cdots\chi_N^{KS}(x_N)|| \tag{30}$$

where the χ^{KS} are the Kohn-Sham (KS) spinorbitals, each one being a product of a Kohn-Sham spatial orbital ψ^{KS} and a spin state ($\alpha(\omega)$ or $\beta(\omega)$). The total energy functional for the reference system can be represented in the same way as for a real system [123]. We can write

$$E[\rho] = T_{ref}[\rho] + J[\rho] + \int \rho(\mathbf{r}) v(\mathbf{r}) d\mathbf{r} + E_{XC}[\rho] \tag{31}$$

where the exchange-correlation energy is

$$E_{XC}[\rho] = T[\rho] + V_{ee}[\rho] - (T_{ref}[\rho] + J[\rho]) \tag{32}$$

This exchange-correlation functional consists of the difference between the exact and approximate kinetic energy along with all non-classical contributions to the electron-electron interactions. The kinetic energy of the reference system T_{ref} can be approximately calculated in the basis of KS orbitals

$$T_{ref} = -\frac{1}{2} \sum_i \langle \varphi_i | \nabla^2 | \varphi_i \rangle \tag{33}$$

Hence, the key takeaway from the entire DFT is the solution of KS equation through the electron density that minimizes the energy functional.

$$\left\{ h_1 + \frac{1}{4\pi\varepsilon_0} \int \frac{\rho(\mathbf{r}_2)}{|\mathbf{r}_1 - \mathbf{r}_2|} d\mathbf{r}_2 + v_{XC}(\mathbf{r}_1) \right\} \chi_i^{KS}(\mathbf{r}_1) = \epsilon_i^{KS} \chi_i^{KS}(\mathbf{r}_1) \tag{34}$$

where $\hat{h}_1$ is the one-electron hamiltonian

$$\hat{h}_1 = -\frac{\hbar^2}{2m_e} \nabla_1^2 + v(\mathbf{r}_1) \tag{35}$$

and the exchange-correlation energy

$$v_{XC}(\mathbf{r}) = \frac{\delta E_{XC}[\rho]}{\delta \rho(\mathbf{r})} \tag{36}$$

Development of accurate DFT functionals continues to be a challenging area of research due to the fact that the nature of exchange-correlation functional, $E_{XC}[\rho]$ is still approximate. Over the years, a large number of exchange-correlation functionals have been developed and made available. Based on the sophistication levels, DFT functionals could be broadly categorized into three kinds of approaches.

1. Local Density Approximation (LDA) where only the electron density value at a certain point is used to calculate exchange-correlation energy.
2. Generalized Gradient Approximation (GGA) which depends on the derivative of the density.
3. *Hybrid functionals* incorporating portions of HF and DFT energies with adaptations of the coefficients from the experimental data.

2.5 TIME-DEPENDENT DENSITY FUNCTIONAL THEORY

An extension of ground-state DFT that allows modelling of excited states is the time-dependent density functional theory (TDDFT). The formalism is based on the Runge-Gross theorem [110] which determines the dynamics of the system by the time-dependent potential via Schrödinger equation. Accordingly, the TDSE formally defines a map by which every external potential $v(\mathbf{r}, t)$ produces a time-dependent wavefunction $\Psi(t)$, for a given initial state Ψ_0 [134]. A second map follows which generates a density $n(\mathbf{r}, t)$ from $\Psi(t)$.

$$v(\mathbf{r}, t) \xrightarrow[\text{fixed}\Psi_0]{i\frac{\partial\Psi}{\partial t} = \hat{H}(t)\Psi} \Psi(t) \xrightarrow{\langle\Psi(t)|\hat{n}|\Psi(t)\rangle} n(\mathbf{r}, t) \tag{37}$$

The time-dependent Kohn-Sham equation is written as

$$i\frac{d}{dt}\psi^{KS}(\mathbf{r}, t) = \left[-\frac{\hbar^2}{2m_e}\nabla^2 + v_{eff}^{KS}(\mathbf{r}, t)\right]\Psi^{KS}(\mathbf{r}, t) \tag{38}$$

with the time-dependent KS orbitals $\Psi^{KS} = \sum_j c_j(t)\chi_j^{KS}(\mathbf{r}_j)$. The usage of TDDFT asks for the absence of a relevant static correlation contribution or a multireference character. The excitation energies are calculated with an exact linear-response expression [20, 21]. For a system with a time-dependent oscillating perturbation, the non-hermitian eigenvalue equation formulates as

$$\begin{bmatrix} \mathbf{A} & \mathbf{B} \\ \mathbf{B}^* & \mathbf{A}^* \end{bmatrix} \begin{bmatrix} \mathbf{X} \\ \mathbf{Y} \end{bmatrix} = \omega \begin{bmatrix} 1 & 0 \\ 0 & -1 \end{bmatrix} \begin{bmatrix} \mathbf{X} \\ \mathbf{Y} \end{bmatrix} \tag{39}$$

where ω gives the excitation energy between the ground and excited states, $\mathbf{X}$ and $\mathbf{Y}$ are the response of the density matrix with respect to the magnitude of the

electric field. The **A** and **B** matrices correspond to the so-called excitations and deexcitations, respectively, and take the form

$$A_{ia,jb} = \delta_{ij}\delta_{ab}(\epsilon_a - \epsilon_i) + \langle ij|ab\rangle + \langle ij|v_{XC}|ab\rangle \tag{40}$$

and

$$B_{ia,jb} = \langle ib|aj\rangle + \langle ib|v_{XC}|aj\rangle \tag{41}$$

respectively. v_{XC} is the exchange-correlation potential corresponding to the exchange-correlation functional E_{XC}. One can define the Tamm-Dancoff approximation (TDA) [113] in which if we set the deexcitation matrix B equal to zero, the procedure becomes computationally more efficient and retains a reasonable amount of accuracy. TDDFT methods have proven to be reliable and efficient along with the advantage of being computationally inexpensive. However, while computing the excitation energies for organic molecules, it overestimates the lowest electronic excitations. This could be seen later in great detail when looking at rhodamines and BODIPY moieties.

2.6 MOLECULAR VIBRATIONAL ANALYSIS

The nuclear potential energy surface (PES) determines the molecular vibrational energy behaviour [142]. A general expression of the PES of an N-atomic molecule is done through the means of Taylor expansion around some reference structure:

$$V(\{x_i\}) = V_0 + \sum_{i=1}^{3N}\frac{\partial V}{\partial x_i}x_i + \frac{1}{2}\sum_{i,j=1}^{3N}\frac{\partial^2 V}{\partial x_i \partial x_j} + \frac{1}{6}\sum_{i,j,k=1}^{3N}\frac{\partial^3 V}{\partial x_i \partial x_j \partial x_k}x_i x_j x_k + \cdots \tag{42}$$

where the $\{x_i\}$ are the atomic Cartesian displacements relative to the reference structure. The reference point chosen is usually an equilibrium structure leading to the disappearance of the first derivatives. Moreover, the need to consider constant energy offset V_0 does not arise as it has no influence on the calculated vibrational properties. Additionally, making the *harmonic approximation* results in the derivatives of higher than second order being neglected. The expression for the potential now looks like

$$V(x_i) = \frac{1}{2}\sum_{i=1}^{3N}\sum_{j=1}^{3N} f_{ij}^{cart}x_i x_j, \quad \text{with} \quad f_{ij}^{cart} = \frac{\partial^2 V}{\partial x_i \partial x_j} \tag{43}$$

The second derivative of the molecular energy with respect to the nuclear coordinates is contained in the matrix $\mathbf{F}^{cart}$ known as the *Hessian* of the molecule. The transformation of the nuclear coordinates to the mass-weighted coordinates $q_i = \sqrt{m_i}x_i$ is a must for the determination of the normal modes of vibration.

$$f_{ij}^{mwc} = \frac{f^{cart}}{\sqrt{m_i m_j}} = \frac{\partial^2 V}{\partial q_i \partial q_j} \tag{44}$$

In the next step, the transformation of the mass-weighted Hessian into internal coordinates removing the effects of translation and rotation is required [100, 142].

$$\mathbf{F^{int}} = \mathbf{D}^T\mathbf{F}^{mwc}\mathbf{D} \tag{45}$$

Here, the transformation matrix $\mathbf{D}$ is constructed based on the Eckart conditions [41, 100, 118] and has the dimensions $3N \times N_{vib}$ with $N_{vib} = 3N - 6$ for non-linear molecules and $N_{vib} = 3N - 5$ for linear molecules. Hence, the dimension of the internal Hessian $\mathbf{F}^{int}$ is $N_{vib} \times N_{vib}$.

By diagonalizing the internal Hessian F^{int}, the normal modes and vibrational frequencies can be determined.

$$\mathbf{L}^{\top}\mathbf{F}^{int}\mathbf{L} = \Lambda \tag{46}$$

Λ is the diagonal matrix which contains the squares of the frequencies of the normal modes. The $\mathbf{L}$ matrix consists of the normal modes in internal coordinates. These matrices can be transformed to mass-weighted and Cartesian coordinates using the respective relations

$$\mathbf{L}^{mwc} = \mathbf{DL} \quad \text{and} \quad \mathbf{L}^{cart} = \mathbf{MDL} \tag{47}$$

The diagonal matrix $\mathbf{M}$ consists of the inverse square root of the mass asscociated with each atomic coordinate. The normal modes in Cartesian coordinates $\mathbf{L}^{cart}$ are routinely obtained from quantum chemical package.

When the previously neglected higher order terms of the potential energy expansion are required, the molecular structure along each normal mode is displaced and then the internal Hessian f^{int} at those new geometries are evaluated. This numerical technique [8] is applied in particular cases, e.g. modeling of vibrational overtones or anharmonic coupling between normal modes. By numerical differentiation, the third and fourth order derivatives with respect to the normal modes can be calculated accordingly.

$$\frac{\partial^3 V}{\partial Q_i \partial Q_j \partial Q_k} \approx \frac{1}{3}\left[\frac{f_{ik}(\delta Q_i) - f_{jk}(-\delta Q_j)}{2\delta Q_i} + \frac{f_{ki}(\delta Q_j) - f_{ki}(-\delta Q_j)}{2\delta Q_j} + \frac{f_{ij}(\delta Q_k) - f_{ij}(-\delta Q_k)}{2\delta Q_k}\right] \tag{48}$$

and

$$\frac{\partial^4 V}{\partial Q_i \partial Q_j \partial Q_k^2} \approx \frac{f_{ij}(\delta Q_k) + f_{ij}(-\delta Q_k) - 2f_{ij}(0)}{\delta Q_k^2} \tag{49}$$

where the superscript of the Hessian has been omitted for clarity. The evaluation of the Hessian for $2(3N-6)$ additional times is needed to obtain all third derivatives for a nonlinear molecule with N atoms. In order to compute fully general fourth order derivatives, simultaneous displacements along two normal modes is required. Taking into account all possible combination of indices for this, the computational cost would be very high. Thus the fourth derivatives in eq. 49 are limited to the case where two of the four indices are equal (note the second derivative with respect to the mode Q_k).

2.7 SOLVATION: POLARIZABLE CONTINUUM MODEL

Many of the electronic structure calculations for the molecules in the respective projects are performed by treateting the solvent effects in accordance with the solvents used for the experiments by the collaboration partners. One of the most

successful computational methods so far for calculations with solvations models has been the polarizable continuum model (PCM). So much so that it is the default choice in many computational procedures due to continuous improvements in terms of efficiency and generality. [93] PCM revolves around the quantum mechanical description of the molecular system of interest in order to account for the effects of the environment on its reactivity and properties. The solvation model plays an essential role especially in the calculation of TPA cross-section of the molecules with the quadratic response method.

To begin with, a continuum model is one in which a number of particles are described in a continuous way by means of a distribution function [93, 132]. Utilizing this model, a solvent is treated as a dielectric polarizable medium with a dielectric constant, ε. The solute molecule M is described at the quantum level and fills a cavity in the dielectric medium. The solute charge density polarizes the solvent that creates a reaction electrostatic potential, V_R that in turn reacts on the solute itself. The solvent reaction potential is then added to the solute quantum Hamiltonian, thus defining a new solute charge distribution. This process is iterated till self-consistency is attained and hence the field in which it is done is termed as self-consistent reaction field (SCRF). Schrödinger equation in continuum solvation methods (CSM) is a non-linear one i.e., the reaction potential $V_R(\psi_i)$ entering the electronic Hamiltonian depends on the equation solution themselves i.e., ψ_i. Different kinds of CSM with different cavity definitions as well as different V_R calculations are possible in which the PCM is the most commonly used.

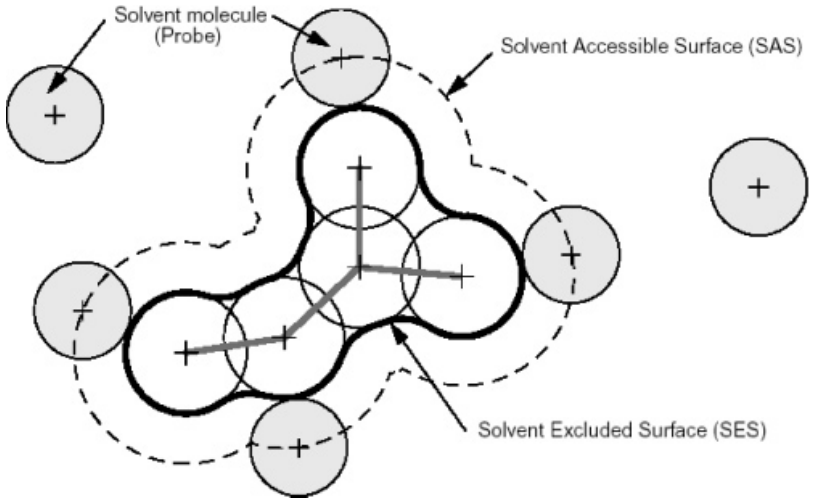

Figure 3: Schematic illustration of a continuum solvation model. Reprinted (adapted) with permission from [132]. Copyright 2005 American Chemical Society.

The basic requirement for the formulation of the continuum models is the solution to a classical electrostatic problem (Poisson equation):

$$-\vec{\nabla} \times \left[\varepsilon(\vec{r})\vec{\nabla}V(\vec{r})\right] = 4\pi\rho_M(\vec{r}) \tag{50}$$

where $\rho_M(\vec{r})$ is the solute charge distribution and $\varepsilon(\vec{r})$ is the general position-dependent permittivity. The cavity fits the solute geometry with van der Waals spheres centered on the atoms. Assuming that a molecular cavity C of proper shape

and dimension contains the charge distribution $\rho_M(\vec{r})$ within a homogenous and isotropic solvent, $\varepsilon(\vec{r})$ assumes the simple form:

$$\varepsilon(\vec{r}) = \begin{cases} 1 & \vec{r} \in C \\ \varepsilon & \vec{r} \notin C \end{cases} \tag{51}$$

The electrostatic potential V is the sum of the solute potential $V_M(\vec{r})$ and the contribution due to a fictitious charge distribution $\sigma(\vec{s})$ on the boundary between the solute and the solvent

$$V(\vec{r}) = V_M(\vec{r}) + V_\sigma(\vec{r}) \tag{52}$$

$$V_\sigma(\vec{r}) = \int_\Gamma \frac{\sigma(\vec{s})}{|\vec{r} - \vec{s}|} d^2s \tag{53}$$

where $\Gamma = \partial C$ represents the surface of the cavity C.

As the whole dielectric medium is considered as the source of reaction potential, the electrostatic problem is greatly simplified by reducing the source of the solvent reaction potential to a charge distribution limited to a closed surface. The entire problem could be solved once $\sigma(\vec{s})$ is known and then the electrostatic component of the solvation free energy would be

$$G^{el} = \frac{1}{2} \int_\Gamma \sigma(\vec{s}) \left[\int_V \frac{\rho_M(\vec{r})}{|\vec{r} - \vec{s}|} d^3r \right] d^2s \tag{54}$$

The key requirement for a practical implementation of a PCM model is a discrete representation of the surface charge distribution over the solute-solvent boundary. In the most common approach, the surface is discretized in N surface elements (often called *tesserae*) characterized by their position $\vec{s}_i$ and their surface area a_i. This discretization of Γ automatically leads to a discretization of $\sigma(\vec{s})$ in terms of point-like charges:

$$q(\vec{s}_i) = \sigma(\vec{s}_i) a_i \tag{55}$$

The generation of the surface elements (i.e., the surface mesh) is a necessary preliminary step in this strategy.

In the quantum mechanical (QM) strategy, the coupling of a continuum description of a solvent with a QM description of the solute is based on the definition of an effective Hamiltonian

$$\hat{H}^{eff} = \hat{H}^0 + \hat{V}^R \tag{56}$$

where the electrostatic interaction between the solute and the solvent

$$\hat{V}^R = \sum_i q(\vec{s}_i) \hat{V}(\vec{s}_i) \tag{57}$$

in which the $\hat{V}(\vec{s}_i)$ indicates the electrostatic potential operator calculated on the surface tesserae.

2.8 QUANTUM DYNAMICS

To study evolution of ultrafast quantum effects on large systems, quantum dynamical methods based on the solutions of TDSE (eq. 1) are employed. In a one-dimensional system, the wavefunction and Hamiltonian can be easily represented by a set of orthogonal basis functions χ_i,

$$\psi(x,t) = \sum_i c_i(t)\chi_i(x) \qquad \text{and} \qquad H_{ij} = \langle \chi_i(x)|\hat{H}|\chi_j(x)\rangle\,, \tag{58}$$

where the wavefunction takes the vector form and the Hamiltonian the matrix form [128]. For systems of more than one dimension, elaborate methods are needed to solve the TDSE.

2.8.1 *Multi-configuration time-dependent Hartree*

The multi-configuration time-dependent Hartree (MCTDH) method [10, 85, 95] is formulated with an *ansatz* where a multidimensional wave function $\Psi(\vec{q},t)$ with n degrees of freedom is represented in a product basis of the form

$$\begin{aligned}\Psi(\vec{q},t) = \Psi(q_1,\cdots,q_n,t) &= \sum_{i_1=1}^{N_1'} \cdots \sum_{i_n=1}^{N_n'} A_{i_1\cdots i_n}(t) \prod_{\kappa=1}^{n} \varphi_{i_\kappa}^{(\kappa)}(q_\kappa,t) \\ &= \sum_I A_I \Phi_I\end{aligned} \tag{59}$$

where $\Phi_I = \prod_{\kappa=1}^{n} \varphi_{i_\kappa}^{(\kappa)}(q_\kappa,t)$ is the configuration corresponding to the multiindex I. In the MCTDH *ansatz*, these 1-D basis functions $\varphi_{i_\kappa}^{(\kappa)}(q_\kappa,t)$ are also denoted as *Single Particle Functions (SPFs)* which are time-dependent. To get the equations of motion (EOMs) for the MCTDH wave function, additional constraints need to be introduced so that eq. 59 is uniquely defined.

$$\langle \varphi_{i_\kappa}^{(\kappa)}(0)|\varphi_{i_\kappa'}^{(\kappa)}(0)\rangle \stackrel{!}{=} \delta_{i_\kappa i_\kappa'} \tag{60}$$

$$\langle \varphi_{i_\kappa}^{(\kappa)}(t)|\dot{\varphi}_{i_\kappa'}^{(\kappa)}(t)\rangle \stackrel{!}{=} 0 \tag{61}$$

Without these constraints, it becomes possible to perform linear transformations on the coefficients $A_{i_1\cdots i_n}(t)$ and the SPFs without changing the total wavefunction. The inclusion of the constraints ensure that the initial SPFs of the κth degree of freedom remains orthonormal.

2.8.2 *Multilayer MCTDH*

An extension of the MCTDH approach, the ML-MCTDH method [135–137] consists of a layered structure to treat systems with several hundred degrees of freedom [94]. The concept of the MCTDH method is repeated for the basis function φ in the ML-MCTDH scheme. The time-dependent basis functions φ used in the

MCTDH method to express the wave function Ψ are themselves expressed through the MCTDH method. The wave function takes the same form as in eq. 59 as in the normal MCTDH method and

$$\begin{aligned}\varphi_{i_\kappa}^{(\kappa)}(q_\kappa, t) &= \varphi_{i_\kappa}^{(\kappa)}\left(q_1^{(\kappa)}, \cdots, q_{n_\kappa}^{(\kappa)}, t\right) \\ &= \sum_{j_1=1}^{N'_{\kappa,1}} \cdots \sum_{j_{n_\kappa}=1}^{N'_{\kappa,n_\kappa}} A_{i_\kappa; j_1 \cdots j_{n_\kappa}}(t) \prod_{\mu=1}^{n_\kappa} \chi_{j_\mu}^{(\kappa,\mu)}\left(q_\mu^{(\kappa)}, t\right)\end{aligned} \tag{62}$$

The functions φ of the MCTDH method are now labelled as *first-layer* SPFs and the functions χ used to express φ as *second-layer* SPFs. The second-layer SPFs can either be expanded in a primitive basis, or the MCTDH approach can be repeated for them also, resulting in deeper layers. The last layer of SPFs has to be expanded in a primitive basis.

3

VIPER EXPERIMENT WITH TWO-PHOTON ABSORPTION

The past decades have witnessed rapid development of sophisticated techniques in spectroscopy. With the availability of the spectroscopic techniques to more than one dimension, it has become easier to reveal the finer details of molecular compositions through the investigation of their rotational, vibrational or electronic motions. Complemented with the advancements in quantum chemistry and computing facilities, it has become easier to study ultrafast processes.

3.1 FUNDAMENTAL OPTICAL SPECTROSCOPY

Understanding interaction of matter with electromagnetic radiation is dealt by spectroscopy. The different regions of the electromagnetic spectrum have a certain effect on the system under probe [4]. The electromagnetic region ranges from $\sim 10^7$Hz (radio waves) to $\sim 10^{19}$Hz (Gamma rays). In between lies the infrared (IR) region (10^{12}Hz-10^{14}Hz), the visible light (vis: 4×10^{16}Hz-8×10^{16}Hz) and the ultraviolet (UV: 8×10^{16}Hz-3×10^{17}Hz).

IR radiation interacts with the molecular vibrations and therefore it helps in identifying the type of bonding with the stretching frequencies. Units commonly used are in terms of wavenumbers. Vibrations can be identified in the range $20\text{cm}^{-1}-4000\text{cm}^{-1}$. In the UV-vis regions, it is the valence electrons of the atoms and molecules which are excited. The fundamental aspect of fluorescence spectroscopy is the measurement of light absorption. A general spectroscopic experiment is setup with a radiation source, a sample and a detector. A sample when irradiated by a light beam of certain wavelength results in reduction of its intensity.

Consider a thin sample having thickness dx that has molar absorptivity ε and concentration c. The intensity dI absorbed per thickness dx is proportional to the intensity of the incident light I, ε and c:

$$\frac{dI}{dx} = -I\varepsilon c \tag{63}$$

Rearrangement and integration of the proportionality yields

$$\ln\left(\frac{I_0}{I}\right) = \varepsilon c l \tag{64}$$

where l is the thickness of the sample. This equation represents the Beer-Lambert law [74].

3.2 TWO-DIMENSIONAL INFRARED SPECTROSCOPY

The fundamental principle of absorption described in the earlier section deals with one-dimensional spectroscopy which has a continuous flow of light. The setup consists of a single source of light and the path begins from the source through the

sample towards the detector. When more than one beam of radiation interacts with the sample, the domain of multidimensional spectroscopy kicks in. More information can be extracted by multidimensional nonlinear spectroscopy that exceeds the information content obtained from one-dimensional absorption spectroscopy.

In the two-dimensional infrared (2D-IR) spectroscopy [23, 56, 57], a femtosecond source generates intense broadband pulses which are further split into an IR-pump and IR-probe pulse. The IR-pump pulse passes through a Fabry-Perot filter [106] after which it shapes into a narrow-band pulse. The center frequency of this pulse can either be controlled by a computer or by changing the distance between the mirrors. The Fabry-Perot filter consists of two parallel partial reflectors between which the pulse is reflected back and forth so that it interferes with itself. Only one frequency survives depending on the distance between the reflectors. Reunification of both the pump and probe pulses occurs at the sample. The probe pulse still has the full bandwidth of the spectrum and can be employed to measure the sample spectrum with respect to the changes after the arrival of the pump pulse. The 2D-IR spectrum thus has two axes, one for the probe frequency and the other for the narrow band pump frequency scanned over the frequency range of interest. This technique is classified under the *double resonance* or *frequency domain* 2D-IR spectrsocopy [18].

In another implementation of nonlinear 2D-IR spectroscopy, a total of four ultrashort laser pulses are generated, three of which pass through the sample creating a nonlinear polarization that radiates a signal field. The fourth pulse is heterodyned with the signal which acts as a local oscillator [23]. Scans of the times delays between the pulses are performed and the fourier transform along them gives the spectrum. This experimental scheme falls under the domain of *pulsed fourier transform* or *time domain* 2D-IR spectroscopy.

These 2D-IR techniques are also referred to as pump-probe experiments where the third-order response functions of the system are directly measured.

3.2.1 *Mixed infrared and optical spectroscopy*

Pure IR experiments remain limited to the electronic ground state where the systems under investigation are usually in equilibrium. In order to extract information about the processes in the electronically excited states, an additional UV/vis pulse is introduced to initiate dynamic evolution of the system. In addition to this, pulse sequences can be designed to take advantage of vibronic coupling [139]. VIPER experiment is one such area of prime interest here. In these mixed techniques, reasonant or nonresonant UV, vis or NIR pulses are sequenced thereby helping in investigating the coupling or correlation between two vibrations, hence generating a 2D-IR spectrum.

3.3 VIPER SPECTROSCOPY

As the expansion of the acronym VIPER indicates, the experiment is a combined vibrational-electronic (shortly termed as vibronic) spectroscopy. Here, an additional UV/vis- pulse between the IR-pump and probe pulse helps in extracting information related to electronic excitation along with that of vibrations [141]. This way

dynamic processes on time scales longer than the typical vibrational lifetime can be investigated which the conventional 2D-IR exchange spectroscopy falls short of. With the help of the fig. 4, the scheme of the experiment with respect to the sequence of pulses can be understood.

In accordance with the conventional 2D-IR experiment [57, 141], the first in the sequence is a narrow-band IR pump pulse. This pulse selectively excites a specific normal mode of the molecule. The timescale of this vibrational excitation decay is a few picoseconds because of intramolecular vibrational redistribution (IVR) as well as the effects of the surrounding medium.

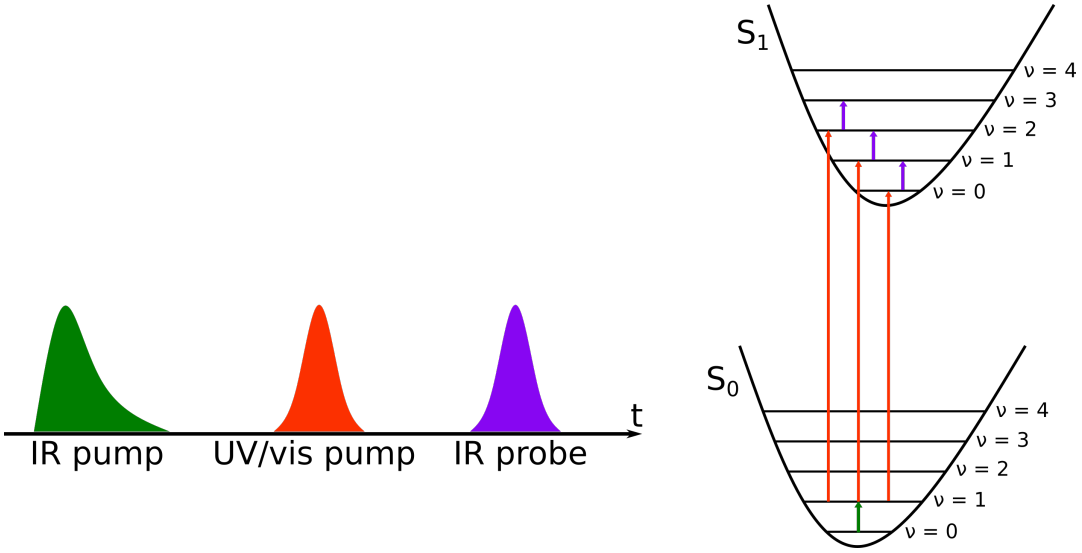

Figure 4: Left: The VIPER pulse sequence consisting of the IR pump, UV/vis pump and IR probe pulses. Right: Vibronic level scheme depicting the corresponding transitions.

The second in the sequence is a narrow-band, off-resonant UV/vis pulse which circumvents the vibrational excitation decay from the first pulse. The molecular system gets elevated from the electronic ground state to an electronically excited state. The criteria for choosing the wavelength of the UV/vis pulse is such that only those molecules which have been previously vibrationally excited by the first IR pump pulse are electronically excited. In other words, only the molecules "labeled" by the IR pre-excitation are excited to the higher electronic state by the off-resonant UV/vis pulse. Since the lifetime of an electronic excitation is much longer than that of the vibrational excitation, the sequence becomes useful for the study of the chemical dynamics. The IR pre-excitation modulates the UV/vis absorption cross-section of the molecule.

The IR probe pulse is the last in the sequence which is an ultrashort and therefore spectrally broad pulse. There exists a possibility of the excited state undergoing further photochemistry and not returning to the ground state at all. Typically, the timescale for fluorescence ranges from nano- to even microseconds. Exploiting this possiblility, the third IR probe pulse can be applied for further exchange spectroscopy measurements [16, 17]. To sum it up, the VIPER experiment could be considered as a modified 2D-IR experiment with an additional UV/vis pulse between the pump and probe pulses [140].

VIPER spectroscopy provides two important benefits:

1. The signal probed with the IR probe pulse decays with the electronic lifetime and not with the vibrational lifetime due to the preceding electronic excitation. This is unlike in a conventional 2D-IR experiment where the second IR probe pulse decay is of the order of picoseconds. This helps in extending the lifetime of the vibrational information to the lifetime of the electronically excited state.

2. The method enables high selectivity. As IR spectra are pretty well-resolved, specific vibrational modes can be targeted by the narrow-band IR pump pulse. When exchange spectroscopy is performed i.e., certain selected atoms of a molecule are subsituted with non-standard isotopes, the vibrational properties alter significantly due to the differences in the masses of the isotopes. The electronic characteristics still remain unaltered. This opens interesting photochemical possibilities, as sub-enesembles within a mixtures such as certain conformers, isomers or species with different intermolecular interactions can be selected by the narrow-band IR pulse for subsequent electronic excitation [66]. Thus, different reaction pathways and dynamics of sub-ensembles in fast dynamic equilibrium can be investigated.

3.4 ELECTRONIC ABSORPTION

The description about the electronic excitation or absorption mentioned so far talks of a linear optical process. In a linear optical process, only a single photon in the UV/vis range gets absorbed. The one-photon absorption (OPA) is linearly dependent on the intensity. The conventional approach to electronic absorption spectroscopy is in frequency domain [128] with the conventional formula for the vibronic absorption spectrum

$$\sigma(\omega_I) = \frac{4\pi^2\omega_I}{3\hbar c} \sum_n |\langle \psi_n|\mu|\psi_i\rangle|^2 \delta(\omega_I + \omega_i - \omega_n) \tag{65}$$

where ω_I is the incident light frequency and ω_i is the frequency of the initial vibrational level in the initial electronic state. The coefficients of the δ function are called as Franck-Condon (FC) factors. These reflect the overlap of the initial state with the excited state ψ_n at energy $E_n = \hbar\omega_n$.

With the development of lasers as sharp as up to the order of attoseconds [104], efficient higher order non-linear optical spectroscopy through simultaneous absorption of more than one photon is now available [103]. So multi-photon absorption brings along with it numerous advantages. It becomes very important to deal with two-photon absorption in great detail.

TPA involves simultaneous interaction of two photons and therefore it increases with the square of the light intensity. This is observed in intense laser beams, particularly focused pulsed lasers generating a high instantaneous photon density. TPA is another way where a given excited state can be accessed by using photons of half the energy (or twice the wavelength) of the corresponding one-photon transition. To understand the process in a simplistic way, consider a single laser beam of frequency ν passing through a non-linear absorbing medium. In a two-step event, the TPA inducing molecular transition between two electronic states can be visualized:

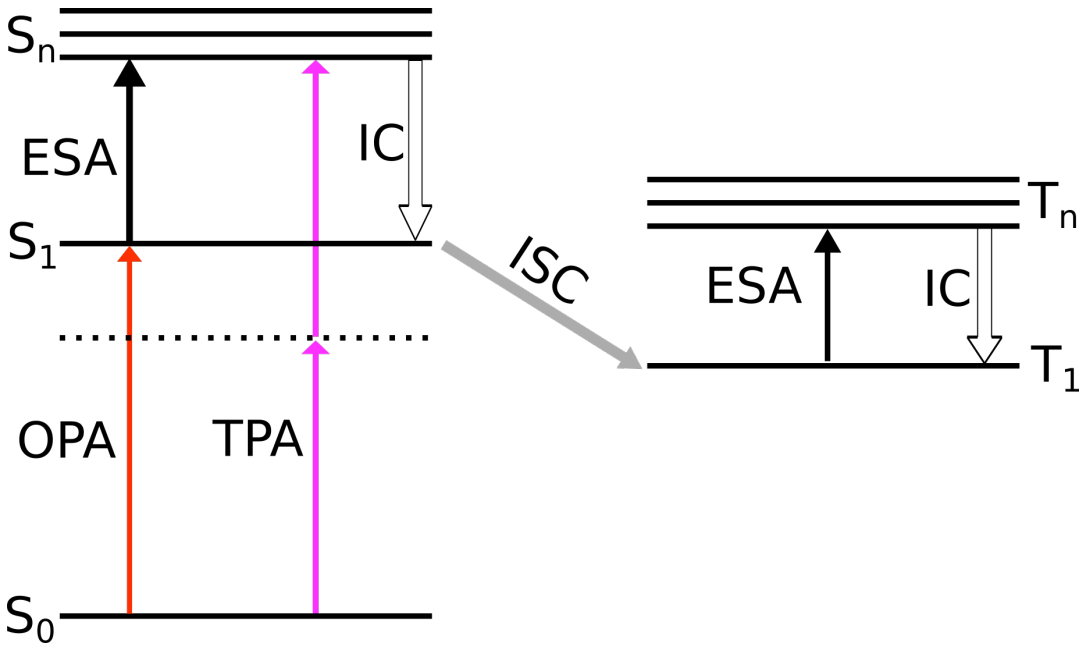

Figure 5: Simplified Jablonski diagram depicting one- and two-photon absorption as well as other photochemical processes: excited state absorption (ESA), internal conversion (IC) and inter-system crossing (ISC).

(i) While the molecule excites from its initial state to an intermediate state, one photon is absorbed.

(ii) Another photon gets absorbed while the molecule transits from the intermediate state to the final state.

The intermediate state here is the key connection between these two steps. During the course, the molecule may stay in all possible eigenstates with a certain probability of distribution on them. Taking into consideration the large uncertainty distribution range, the residence time of the molecule in the intermediate state should be infinitely short according to the uncertainty principle. To summarize, a real TPA is a single elementary process involving simultaneous occurence of the two steps. In the other so-called cascaded two-step one-photon processes, the molecule absorbs one photon to reach an excited state with a certain lifetime, followed by absorption of another photon by the excited molecule to reach a higher level in the second step [59].

The theoretical aspects of the OPA and TPA can now be further understood with the role of the vibronic coupling [78].

3.4.1 *One-photon absorption*

When both electronic and vibrational states are accounted for, the absorption cross-section in atomic units (a.u.) [80] can be written as

$$\sigma_{OP} = \frac{4\pi^2\omega}{3c} \sum_u |\mu_{vu}|^2 \Delta(\omega_u - \omega, \Gamma_u) \tag{66}$$

where c is the speed of light *in vacuo*, ω is the circular frequency of the laser, and ω_u is the transition energy from the initial state u to the final state v. This summation is done over the molecular x, y and z axes to account for the average over all the possible orientations. The transition dipole moment is explicitly evaluated as

$$\mu_{vu} = \langle v|\mu|u\rangle \tag{67}$$

μ denotes the Cartesian component of the transition electric dipole moment operator. The lifetime broadening for a general n-photon absorption process is usually described by a Lorentzian function

$$\Delta(\omega_u - n\omega, \Gamma_u) = \frac{1}{\pi}\frac{\Gamma_u}{(\omega_u - n\omega)^2 + \Gamma_u^2} \tag{68}$$

Γ_u is the broadening of the final state. To get more information about the dipole moment operator, the Born-Oppenheimer adiabatic approximation is applied separating the electronic and vibrational parts.

$$\mu_{vu} = \langle v|\mu(Q)|u\rangle \tag{69}$$

where $\mu(Q)$ is the electronic part of the transition dipole moment which can be expanded in a Taylor series with respect to the normal coordinates Q_a,

$$\mu(Q) = \mu(Q)_0 + \sum_a \frac{\partial\mu}{\partial Q_a} Q_a + \dots \tag{70}$$

Inserting the first two terms of this expansion into eq. 69

$$\mu_{vu} = \mu(Q)_0 \langle v|u\rangle + \sum_a \frac{\partial\mu}{\partial Q_a} \langle v|Q_a|u\rangle \tag{71}$$

The first term here is the electronic transition moment at the equilibrium position of the initial state multiplied by the Franck-Condon (FC) overlap. The second term is called as Herzberg-Teller (HT) contribution which arises from the vibronic coupling between electronic states.

3.4.2 *Two-photon absorption*

For two photons of equal frequency $\omega_1 = \omega_2 = \omega$, the TPA cross-section σ_{TP} is given by the expression

$$\sigma_{TP} = \frac{4\pi^3 a_0^5 \alpha}{15c} \omega^2 \Delta(\omega_u - 2\omega, \Gamma_u) \delta_{TP}^{vu}(\omega) \tag{72}$$

where α is the fine structure constant, a_0 is Bohr radius, and $\delta_{TP}(\omega)$ the orientationally TPA probability. Because of the sensitivity of the TPA to the polarization of fundamental laser beams, an orientational average is required [90, 98]. For molecules in the gas phase and solutions,

$$\begin{aligned}\delta_{TP}^{vu}(\omega) = \sum_{ij=x,y,z} \big[& F \times S_{ii}^{vu}(\omega) S_{jj}^{vu}(\omega) + G \times S_{ij}^{vu}(\omega) S_{ij}^{vu}(\omega) \\ & + H \times S_{ij}^{vu}(\omega) S_{ji}^{vu}(\omega) \big]\end{aligned} \tag{73}$$

The F,G and H coefficients depend on the polarization of the light.

$F = G = H = 2$ for linearly polarized light.

$F = -2; \quad G = H = 3$ for circular polarized light.

The two-photon transition matrix element can be written in a sum-over-state formulation when the vibronic states are explicitly included in the summation [122].

$$S_{ij}(\omega) = \sum_K \left[\frac{\langle \nu|\mu_i|K\rangle \langle K|\mu_j|u\rangle}{\omega_K - \omega} + \frac{\langle \nu|\mu_j|K\rangle \langle K|\mu_i|u\rangle}{\omega_K - \omega} \right] \tag{74}$$

where the summation runs over all the intermediate electronic and vibrational ($|K\rangle$) states. Applying the Born-Oppenheimer adiabatic approximation separating the electronic and vibrational parts to the two-photon transition matrix element

$$S_{ij}^{\nu u}(\omega) = \langle \nu|S_{ij}(\omega, Q)|u\rangle \tag{75}$$

where $S_{ij}(\omega, Q)$ is the electronic part of the two-photon matrix element

$$S_{ij}(\omega, Q) = \sum_k \left[\frac{\langle g|\mu_i|f\rangle \langle k|\mu_j|f\rangle}{\omega_k - \omega} + \frac{\langle g|\mu_j|k\rangle \langle k|\mu_i|f\rangle}{\omega_k - \omega} \right] \tag{76}$$

The summation explicitly includes the ground state $|g\rangle$. Expanding $S_{ij}(\omega, Q)$ in a Taylor series with respect to the normal coordinates Q_a

$$S_{ij}(\omega, Q) = S_{ij}(\omega, 0) + \sum_a \frac{\partial S_{ij}(\omega, Q)}{\partial Q_a} Q_a + \dots \tag{77}$$

Therefore the total TPA transition moment is given by the expression

$$S_{ij}^{\nu u}(\omega) = S_{ij}(\omega, 0) \langle \nu|u\rangle + \sum_a \frac{\partial S_{ij}(\omega, Q)}{\partial Q_a} \langle \nu|Q_a|u\rangle \tag{78}$$

Likewise as in OPA, here too, the first and second terms correspond to the FC and HT contributions, respectively to the TPA spectrum. Hence in both OPA and TPA spectra the vibronic intensity distributions within this approximation share the same set of vibrational overlap integrals, the electronic transition moments being quite different in principle.

3.5 VIPER EXPERIMENT WITH TWO-PHOTON ABSORPTION

In contrast to the VIPER experiment with the UV/vis pulse, the VIPER spectrsocopy with TPA would replace the UV/vis pulse with a NIR on-resonant pulse for two-photon excitation according to the scheme illustrated in the fig. 6. The sequence of the pulses remains the same as in a conventional 2D-IR experiment. A design of an ultrafast two-pulse fluorescence encoded IR spectroscopy has been reported by Mastron *et al.* [88] which provides an intuition also about the study of ground-electronic-state vibrational dynamics using IR excitation followed by two-photon excitation to the first electronic singlet state.

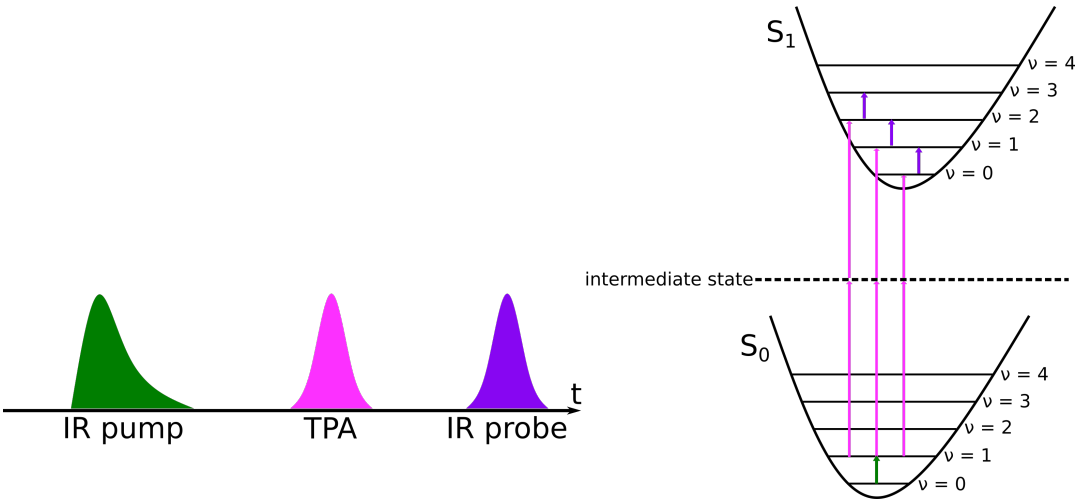

Figure 6: Left: The pulse sequence of the VIPER experiment with TPA consisting of the IR pump, TPA and IR probe pulses. Right: Vibronic level scheme depicting the corresponding transitions. The TPA transition involves passing through an intermediate virtual state.

3.6 SIMULATION OF VIBRATIONALLY RESOLVED ELECTRONIC SPECTRA

In a conventional way, a thermally averaged ensemble of excited vibrational states is considered that are populated according to the Boltzmann distribution. According to the VIPER experiment sequence, the first IR pump pulse elevates the molecule to a vibrationally excited state. This means that a specific normal mode resonant to the pump pulse frequency gets excited while all the other normal modes remain in their respective ground state. As understood earlier, the IR pre-excitation modulates the electronic absorption spectra which would be probed by the subsequent UV/vis pulse.

If an ideal purely electronic two-level system is taken into consideration, the spectrum would show only one possible transition. There would just be a single signal which is a δ function at a frequency resonant to the energy gap between the two electronic states. In real case, however, the electronic and the nuclear contributions are coupled resulting in the electronic transition generating a force on the nuclei further leading to vibration. Referring to the vibrational level structure of the molecule, the excitation from the ground state $|g\rangle$ to the excited state $|e\rangle$ is accompanied by a multitude of transitions between vibrational levels. In other words, there exists a combination of electronic and vibrational transitions easily termed as *vibronic* transitions. Given the fact that the nuclei are heavier than the electrons and slower in motion, a justified assumption is made that the electronic transitions are vertical, implying that the nuclear configuration remains unchanged during the transition. Based on this fact, a popularly known Franck-Condon principle [3] states that an electronic transition occurs within a stationary nuclear framework. The δ function generates the signals giving out a stick spectrum.

It becomes clear that the real complete spectrum consists of all possible vibronic transitions. At temperature 0K, only the vibrational ground state is populated. When the temperature is higher than 0K, additionally several vibrational states $|w_g\rangle$ in the electronic ground state are populated, w_g indicating the vector of vibrational

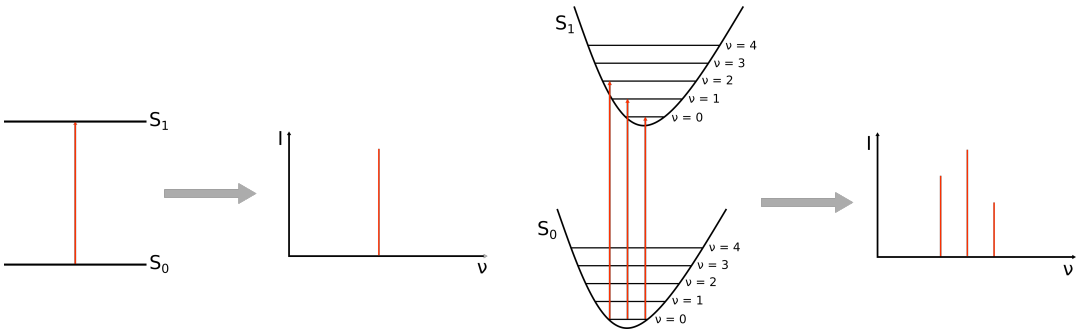

Figure 7: Left: a simplified two-level system, where only a single transition is possible, resulting in a single line in the idealized spectrum. Right: nuclear PESs that give rise to multiple vibronic transitions with different intensities depending on the overlap of the corresponding vibrational wavefunctions.

quantum numbers. The absorption spectrum composed of vibronic transitions is given by the expression [112]

$$\epsilon(\omega) = A\omega \sum_{w_g} \sum_{w_e} p_{w_g} |\mu_{w_g,w_e}|^2 \delta(E_{w_g} - E_{w_e} - E_{ad} + \hbar\omega) \tag{79}$$

where all possible vibrational states $|w_g\rangle$ in the electronic ground state $|g\rangle$ and the vibrational states $|w_e\rangle$ in the excited electronic state $|e\rangle$, whose corresponding energies are E_{w_g} and E_{w_e}, respectively are ran over by the summation. E_{ad} represents the adiabatic energy difference between the minima of the ground and excited state PES and p_{w_g} the population of the initial vibrational state. The conversion of the absorption spectrum to the regular units of molar absorptivity is done by the scaling prefactor whose magnitude turns out to be 703.3 in atomic units [108]

$$A = \frac{4\pi^2 N_A}{3\log(10)\hbar c \cdot 4\pi\epsilon_0} \tag{80}$$

Using BO approximation, the transition dipole moment between the vibronic states can be separated into an electronic and a vibrational contribution accordingly

$$\mu_{w_g,w_e} = \langle w_g | \langle g|\hat{\mu}|e\rangle | w_e\rangle = \langle w_g|w_e\rangle \, \mu_{ge}(Q) \tag{81}$$

where the electronic transition dipole moment is represented by $\mu_{ge}(Q)$, which in turn depends on the nuclear coordinates. Using Taylor's expansion of the vibrational normal modes Q, the coordinate dependence can be easily expressed as

$$\mu_{ge}(Q) = \mu^{(0)} + \sum_k \mu^{(k)} Q_k + \frac{1}{2} \sum_k \sum_l \mu^{(k,l)} Q_k Q_l + \dots \tag{82}$$

The zero-order term $\mu^{(0)}$ makes dominating contribution in the case of strongly allowed electronic transitions. When the transition dipole moment is coordinate independent, the higher order terms can be neglected. This assumption results in FC spectrum, within the *Franck-Condon approximation* [14] where the excitation is vertical within the stationary framework of the nuclear coordinates. In case of weakly allowed or forbidden transitions the first order term makes a significant contribution under the *Herzberg-Teller approximation* [116]. The FC and HT approximations have already been dealt with in great detail in the earlier sections.

3.6.1 *The time-independent approach*

To simulate the spectrum, the energies and intensities of the constituent transitions have to be calculated. The superposition of individual vibronic transitions through eq. 79 in the energy domain gives the complete absorption spectrum in a time-independent framework. It has been already stated in the earlier section about how on applying the Born-Oppenheimer approximation, the vibrational part of the transition dipole moment can be obtained by calculating the FC overlap integrals between the two vibrational eigenfunctions of the PES of the contributing electronic states. During the calculation of these integrals, it needs to be considered that the vibrational coordinates of $|e\rangle$ are different from the vibrational coordinates of $|g\rangle$. The linear transformation [40] relates them through the Duschinsky matrix **J**.

$$\mathbf{Q}_g = \mathbf{J}\mathbf{Q}_e + \vec{K} \tag{83}$$

The Duschinsky matrix represents the rotation of the normal coordinates of the ground state with respect to those of the excited state and is not diagonal generally [124]. The displacement of the equilibrium configurations of the two states is represented by the shift vector $\vec{K}$. Both **J** and $\vec{K}$ can be evaluated after a vibrational analysis in both states according to

$$\mathbf{J} = \left(\mathbf{L}_g^{mwc}\right)^{-1} \mathbf{L}_e^{mwc} \tag{84}$$

and

$$\vec{K} = \left(\mathbf{L}_g^{mwc}\right)^{-1} \left(q_e^{eq} - q_g^{eq}\right) \tag{85}$$

L is the normal-mode matrix which relates the normal modes **Q** to mass-weighted cartesian coordinates q. The computation of the general FC integral $\mathcal{J}_{w_g,w_e} = \langle w_g|w_e\rangle$ is enabled by the analytic relation between the normal coordinates of the two states. The square moduli of the integral give out FC factors. Two possible routes exist for this purpose. One is via analytic recursion formulae based on generating functions of Sharp and Rosenstock. In this case, $\mathcal{J}_{0_g,0_e} = \langle 0_g|0_e\rangle$ is analytically solvable and the integrals $\mathcal{J}_{0_g,w_e} = \langle 0_g|w_e\rangle$ and $\mathcal{J}_{w_g,w_e} = \langle w_g|w_e\rangle$ are solved through recursion formulae [112, 121]. The other approach introduced by Doktorov *et al* is based on coherent states [37] which has been found to be mathematically equivalent [76].

Calculating the FC integrals is the key to computing the vibrationally resolved electronic spectrum with the time-independent approach. This actually seems to be a mammoth task as even in medium-sized molecules there are vast number of contributing FC integrals, on the order of 10^7 for a system of 100 normal modes for example. There arises a need, as a result, to compute the set of most relevant integrals after their *a priori* selection. An efficient method named *FCclasses* has been developed by Santoro in which the vibronic transitions are clubbed together into so-called *classes* with respect to the number of simultaneously excited normal modes in the final state $|e\rangle$ [112, 115]. As an example, in C_1 class all vibronic transitions exist where the final state $|w_e\rangle$ consists of all normal modes except the excited one in their respective ground state. The higher classes ($C_n, n = 2, 3, \ldots$) consists of the simultaneously excited respective number of modes. Evidently, the number of

vibronic transitions in every class increases rapidly with n. On the contrary, the transitions belonging to lower classes can reasonably be expected to have higher contributions to the spectrum than the higher classes.

In a simple case of spectra at 0K, i.e., only the vibrational ground state is populated, meaning all the FC integrals of the form $\langle 0_g | w_e \rangle$, the prescreening procedure involves calculation of FC integrals of classes C_1 and C_2 up to a certain quantum number and their storage in memory. For C_2 integrals, only those subset of integrals where both modes are in the same state are computed. The maximum quantum number must be chosen on the basis that the role of the neglected integrals is expected to be still negligible in the spectrum. The FC integrals in the C_1 and C_2 classes provides account of the equilibrium shift and normal mode rotations or the Duschinsky couplings excluding the frequency or the position shifts. Taking this information into consideration, the maximum quantum number for all classes C_n with $n \geqslant 3$ is deduced. The search for the most promising integrals in the higher classes depends on the information from the first two classes based on which a vector of maximum quantum numbers for the class C_n is determined using two previously defined threshold parameters [112]. On exceeding a pre-defined value N_{max}, the threshold parameters reduce and the vector of maximum quantum numbers is recomputed until the integrals to be computed becomes lower than N_{max}. N_{max} determines the level of accuracy of the spectra to be obtained. The FC integrals for all possible combinations of n oscillators are computed after determining the maximum quantum number for the class in correspondence with the respective excitation limit. In practice, the highest class employed for computation is usually C_7.

When $T > 0K$, multiple vibrational states $|w_g\rangle$ are populated according to their Boltzmann factors p_{w_g}. The weighted sum of spectra obtained from the individual vibrational states gives out the total absorption spectrum. A threshold value for p_{w_g} is defined and states with lower population are neglected due to their low influence. Introducing multiple initial states increases the computational effort. This issue can be resolved by introduction of so-called *mother states* exploiting the recursive nature of the formulae for the calculation of FC integrals. In the mother states, each excited mode attains its highest quantum number [115]. The calculation of FC integrals of these states automatically covers all lower energy states with the same excitation pattern. Additionally, the convergence can be improved by treating the subset of the final state normal modes that are strongly coupled to the thermally excited states via the Duschinsky matrix $\mathbf{J}$ with greater accuracy, allowing for higher excitations than the respective C_n class would permit.

Like in the case of computation of finite temperature spectra, the same framework can also be applied to compute the spectrum from a vibrationally pre-excited state because the excitation of single modes formally resembles a thermal excitation of the whole molecular system. Here, there is only one mother state, $|\mathbf{0}_g + \mathbf{1}_k\rangle$ where mode k has been put into its first excited state and all FC integrals are of the form $\langle \mathbf{0}_g + \mathbf{1}_k | \mathbf{w}_e \rangle$.

3.6.2 *The time-dependent approach*

The expression for the absorption spectrum eq. 79 can be reformulated in the time domain by recognizing that the delta function can be defined as

$$\delta(\omega) = \frac{1}{2\pi} \int_{-\infty}^{\infty} e^{i\omega t} dt \tag{86}$$

which can be substituted into eq. 79 to yield [6, 114]

$$\epsilon(\omega) = \frac{A\omega}{2\pi Z} \int \chi(t, T) e^{i\left(\omega - \frac{E_{gd}}{\hbar}\right)t} dt \tag{87}$$

Here, Z is the vibrational partition function and the autocorrelation function $\chi(t, T)$ can be expressed as a trace over the initial vibrational states:

$$\chi(t, T) = \mathrm{Tr}\left[\mu_{ge} e^{-\hat{H}_e \tau_e} \mu_{ge} e^{-\hat{H}_g \tau_g}\right] \tag{88}$$

The vibrational Hamiltonians of the ground and excited state are $\hat{H}_g$ and $\hat{H}_e$, respectively. μ_{ge} is the electronic transition dipole moment. τ_g and τ_e are the time variables [6] defined by

$$\tau_g = \frac{1}{k_b T} - i\frac{t}{\hbar} \qquad \tau_e = i\frac{t}{\hbar} \tag{89}$$

Therefore, in this formulation, the finite temperature is automatically included via τ_g.

3.6.3 *Suitability for vibrational pre-excitation*

A specific normal mode of vibration needs to meet certain criteria to be chosen for pre-excitation. An *a priori* estimate of the effect of a particular pre-excitation has to be determined in regard to the suitability for VIPER excitation. The magnitude of the vibronic transition from the pre-excited state $|0_g + 1_k\rangle$ to the ground state which is enabled by the pre-excitation should be as high as possible. For this purpose, the ratio

$$\frac{\langle 0_g + 1_k | 0_e \rangle}{\langle 0_g | 0_e \rangle} = \frac{S_k}{\sqrt{2}} \tag{90}$$

can be computed where the column vector $\mathbf{S}$ is defined by

$$\mathbf{S} = 2\delta_g \left[1 - \Omega^{\frac{1}{2}} \mathbf{J} \left(\mathbf{J}^T \Omega_g \mathbf{J} + \Omega_e\right)^{-1} \mathbf{J}^T \Omega_g^{\frac{1}{2}}\right] \tag{91}$$

Here, $\delta_g = \mathbf{K}^T$ is the vector of *dimensionless displacements* along the ground state normal coordinates. Due to the fact that these displacements relate the displacement to the steepness of the harmonic potential, i.e., the frequency, a more reliable estimate of the effect of a displacement could be known. The dimensionless displacements are related to the Huang-Rhys factor by $S_k^{HR} = \frac{1}{2}\delta_k^2$ [99]. It becomes

clear from the eq. 91 that the dominant factor determining the integral ratio is the dimensionless displacement.

If the excited state equilibrium structure features a large displacement along the selected mode with respect to the ground state equilibrium configuration as depicted in fig. 8, the vibrational pre-excitation leads to an intense $M - 0$ vibronic transition where M represents the vibrational excited state of the electronic ground state [28]. The role of Duschinsky mixing in this context appears to be insignificant particularly when a purely rotated vibrational structure without any displacement yields no $M - 0$ transition. If a strong vibronic coupling results when the electronic transition involves the same structural region of the molecule as the pre-excited normal mode, the effect of pre-excitation is most pronounced.

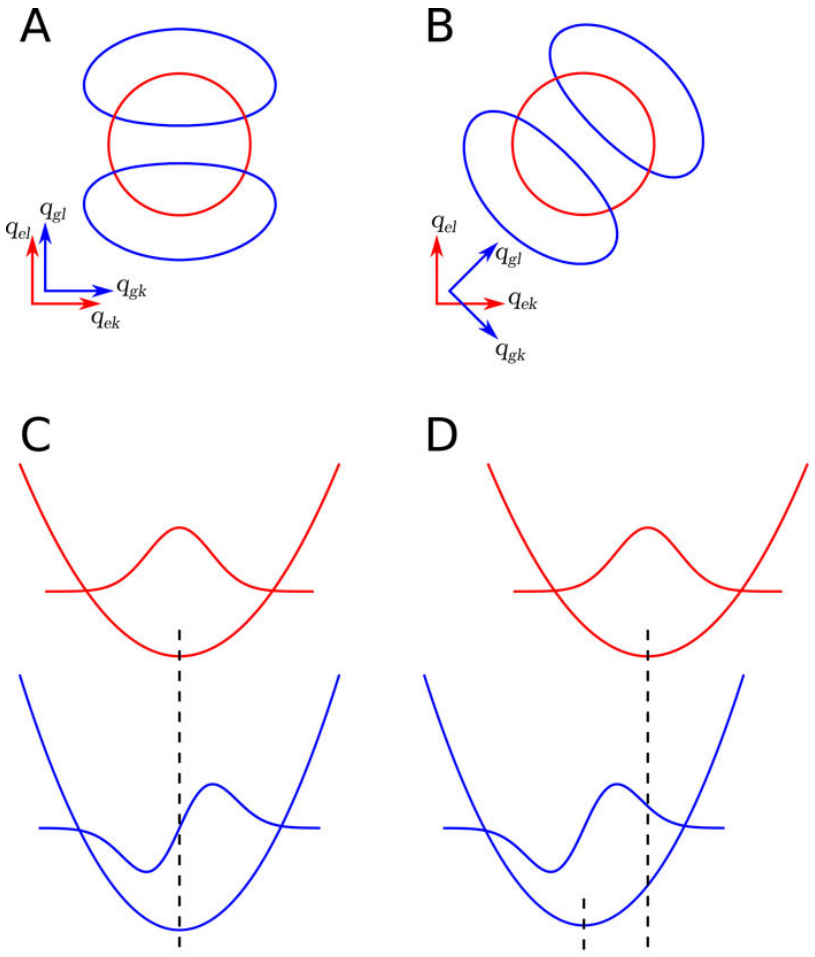

Figure 8: Schematic illustration of the influence of normal coordinates displacement vs Duschinsky rotation on the overlap of the pre-excited vibrational state $|0_g + 1_k\rangle$ with the vibrational ground state $|0_e\rangle$. Reprinted from [28], with the permission of AIP Publishing.

3.6.4 *Adiabatic and vertical harmonic approaches*

The vibronic spectra calculation of large molecules requires expansion of the initial and final state of the PES, V' and V respectively around some reference nuclear structure. The final state PES expansion around the initial- or final- state equilib-

rium structure is enabled by the vertical and adiabatic approaches [44, 113], respectively. To begin with, a N_a-atoms molecular system and an electronic transition from the initial state $|e'\rangle$ to the final state $|e\rangle$ is considered. The 3N column vector of the Cartesian coordinates x define the nuclear structure and x'_0 the equilibrium geometry of the initial state. In the matrix form, the harmonic PES of the initial V' state can be expressed as

$$V'(\mathbf{Q}') = \frac{1}{2}\mathbf{Q}'^{T}\Omega'^{2}\mathbf{Q}' \tag{92}$$

where Ω is the diagonal matrix of the normal frequencies of vibration and Q' is the vector of the N associated normal coordinates defined as

$$\mathbf{L}'\mathbf{Q}' = \mathbf{M}^{\frac{1}{2}}(\mathbf{x} - \mathbf{x}'_0) \tag{93}$$

$\mathbf{M}$ is the diagonal matrix of the atomic masses.

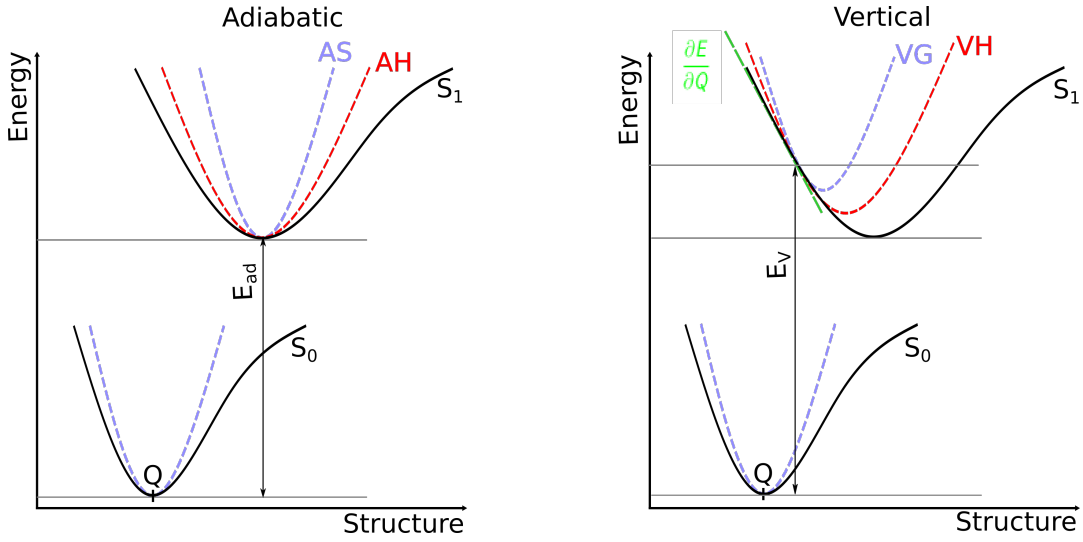

Figure 9: Simpified energy diagrams representing two singlet states without intersections. Left: Display of adiabatic parameters and harmonic model PES. Right: Display of vertical values and harmonic model PES.

3.6.4.1 *Adiabatic approaches*

The adiabatic models involve expansion of the final state PES, V around its own equilibrium structure $\mathbf{x}_0$ as depicted in the left panel of fig. 9.

Adiabatic Hessian (AH) model

The gradient of V at x_0 is zero which leaves only the computation of the Hessian of V at x_0 to get its harmonic approximation.

$$V(\mathbf{Q}) = E_{ad} + \frac{1}{2}\mathbf{Q}^{T}\Omega^{2}\mathbf{Q} \tag{94}$$

$$\mathbf{L}\mathbf{Q} = \mathbf{M}^{\frac{1}{2}}(\mathbf{x} - \mathbf{x}_0) \tag{95}$$

where the E_{ad} represents the minimum energy of the final state PES with respect to the energy of the initial state PES in its own minimum taken as a reference. This model is named as the adiabatic Hessian (AH). $\mathbf{Q}$ and $\mathbf{Q}'$ can be expressed as a function of each other.

$$\mathbf{Q}' = \mathbf{J}\mathbf{Q} + K \tag{96}$$

$$\mathbf{J} = \mathbf{L}'^{-1}\mathbf{L} \tag{97}$$

$$\mathbf{K} = \mathbf{L}'^{-1}\mathbf{M}^{\frac{1}{2}}(\mathbf{x} - \mathbf{x}_0) \tag{98}$$

where $\mathbf{J}$ is the Duschinsky matrix and $\mathbf{K}$ is the equilibrium position displacement vector. These matrices can be represented in terms of mass-weighted coordinates [29] as already shown earlier in Section 3.6.1. The final state PES can be written as a function of the normal coordinates of the initial state $\mathbf{Q}'$

$$V(\mathbf{Q}') = E_{ad} + \frac{1}{2}\mathbf{K}^T\mathbf{J}\Omega^2\mathbf{J}^T\mathbf{K} - \mathbf{K}^T\mathbf{J}\Omega^2\mathbf{J}^T\mathbf{Q}' + \frac{1}{2}\mathbf{Q}'^T\mathbf{J}\Omega^2\mathbf{J}^T\mathbf{Q}' \tag{99}$$

The last term is a quadratic function but not in canonical form, exhibiting linear terms and a generally non-diagonal force constant matrix $\mathbf{F_A} = \mathbf{J}\Omega^2\mathbf{J}^T$. The reorganization energy on the final state PES at the ground state geometry would be

$$E_r^{(AH)} = \frac{1}{2}\mathbf{K}^T\mathbf{J}\Omega^2\mathbf{J}^T\mathbf{K} \tag{100}$$

Hence, the estimate of the vertical excitation energy at the initial state geometry is $E_V^{(AH)} = E_{ad} + E_r^{(AH)}$ according to the AH model.

Adiabatic Shift (AS) model

The adiabatic shift (AS) model [9] is built on the model on the assumption that the final and initial state PES share the same Hessian i.e., the same normal modes and frequencies and their minima are simply displaced. The definitions become $\mathbf{J}^{(AS)} = 1$ and $\Omega^{(AS)} = \Omega'$ whereas $\mathbf{K}$ retains the same expression given in eq. 98. The reorganization energy becomes $E_r^{(AS)} = \frac{1}{2}\mathbf{K}^T\Omega'^2\mathbf{K}$ and $E_V^{(AS)} = E_{ad} + E_r^{(AS)}$. The AS expression for the final state PES is simplified

$$V(\mathbf{Q}') = V'(\mathbf{Q}') + E_V^{(AS)} + \mathbf{K}'^T\Omega'^2\mathbf{Q}' \tag{101}$$

where its difference with respect to V' is just a linear function of $\mathbf{Q}'$.

3.6.4.2 *Vertical approaches*

The vertical approach is an alternative to the adiabatic model. It is a quadratic model of the final state PES V built simply of the ground of vertical data [22] as depicted in the right panel of the fig. 9.

Vertical Hessian (VH) model

The data is computed at the initial state geometry $\mathbf{x}_0$. In Cartesian coordinates (indicated by the subscript x), the final state PES is then

$$V(\mathbf{x}) = E_V + \mathbf{g}_x^T \mathbf{x} + \frac{1}{2}\mathbf{x}^T \mathbf{F}_x \mathbf{x} \tag{102}$$

where E_V is the energy, $\mathbf{g}_x$ is the gradient and $\mathbf{F}_x$ the Hessian of V. It can be expressed in terms of the ground state normal coordinates $\mathbf{Q}'$ exploiting eq. 95

$$V(\mathbf{Q}') = E_V + \mathbf{g}^T \mathbf{Q}' + \frac{1}{2}\mathbf{Q}'^T \mathbf{F} \mathbf{Q}' \tag{103}$$

E_V is the vertical excitation energy.

$$\mathbf{g} = \mathbf{M}^{-\frac{1}{2}} \mathbf{L}' \mathbf{g}_x \tag{104}$$

$$\mathbf{F} = \mathbf{L}'^T \mathbf{M}^{-\frac{1}{2}} \mathbf{F}_x \mathbf{L}' \mathbf{M}^{-\frac{1}{2}} \tag{105}$$

Vertical Gradient (VG) model

The Vertical Gradient method is also known in the literature as the linear coupling model [83] (LCM). The linear term in the expansion of the final state PES V around the equilibrium geometry of the ground state is taken and then physically the excited state PES is approximated by a mere shift in the ground state PES. With no scrambling of the normal mode coordinates or change in the harmonic frequencies, the displacement of the harmonic oscillator corresponding to the mode a could be obtained from the excited state energy gradient $G_a = \frac{\partial E^{exc}}{\partial Q_a}$ as

$$d_a = \frac{G_a}{\omega_a^2} \tag{106}$$

The overlap between two displaced vibronic states for one normal mode a with occupation numbers $m_a > n_a$ can be generally expressed as

$$\langle m_a | n_a \rangle = e^{-\frac{x}{2}} x^{\frac{m_a - n_a}{2}} \sqrt{\frac{n_a!}{m_a!}} L_{n_a}^{m_a - n_a}(x) \tag{107}$$

Here, x is a dimensionaless parameter dependent on the displacement d and frequency of the normal mode as $x = \frac{\omega_a d_a^2}{2\hbar}$. The associated Laguerre polynomial:

$$L_{n_a}^{m_a - n_a}(x) = \sum_{r=0}^{n_a} \frac{m_a!(-x)^r}{(n_a - r)!(m_a - n_a + r)!r!} \tag{108}$$

The expression of Q_a in terms of raising and lowering operators of the intial harmonic oscillator

$$Q_a = \sqrt{\frac{\hbar}{2\omega_a}}(a^\dagger + a) \tag{109}$$

can be applied to evaluate the elements $\langle m_a|Q_a|n_a\rangle$ easily connected to the elements $\langle m_a|n_a\rangle$.

$$\langle n_a|Q_a|m_a\rangle = \sqrt{\frac{\hbar}{2\omega_a}}\left(\sqrt{m_a}\,\langle m_a-1|n_a\rangle + \sqrt{m_a+1}\,\langle m_a+1|n_a\rangle\right) \tag{110}$$

In this case $m_a = 0, 1$, and hence the FC factor could be obtained as

$$\langle 0^0|n_a^F\rangle = (-1)^{n_a^F}\frac{x^{\frac{n_a^F}{2}}}{\sqrt{n_a^F!}}e^{-\frac{x}{2}} \tag{111}$$

The Herzberg-Teller factor would be obtained as

$$\langle 0^0|Q_a|n_a^F\rangle = \sqrt{\frac{\hbar}{2\omega_a}}\frac{(-1)^{n_a^F}x^{\frac{n_a^F-1}{2}}}{\sqrt{n_a^F!}}\left(x-n_a^F\right)e^{-\frac{x}{2}} \tag{112}$$

For a total overlap between ground $|0^0\rangle$ and excited state $|f^F\rangle$ vibrational wavefunctions the product of the single displaced harmonic oscillator overlap integrals needs to be evaluated.

$$\langle 0^0|f^F\rangle = \prod_a \langle m_a^0|n_a^F\rangle \tag{113}$$

$$\langle 0^0|Q_a|f^F\rangle = \langle m^0|Q_a|n_a^F\rangle \prod_{b\neq a}\langle m_b^0|n_b^F\rangle \tag{114}$$

The anharmonicity of the potential around the vertical excitation point in the FC region is also accounted for when calculating the vibronic intensities using first-order coupling constants.

3.6.4.3 *Shifts, Gradients and Frequencies*

There are some intermediate models in which the PES of the final state V is assumed to have the same gradient as the PES of the initial state V' but the Hessian can be different. This leads to the implication that Duschinsky mixing for the normal modes is still not allowed ($\mathbf{J} = 1$) however, the frequencies change upon electronic transition. The models according to the adiabatic and vertical approaches are referred to as *adiabatic shift and frequencies* (ASF) and *vertical gradient and frequencies* (VGF), respectively.

3.7 TWO-PHOTON ACTIVE PHOTOLABILE PROTECTING GROUPS

Chemical biology employs light as an efficient tool in order to regulate biochemical activities on a molecular level [52]. Photoactivable or in other words caged bioactive molecules help in achieving control of biological functions. The general idea behind the scheme is that a bioactive molecule is covalently bonded to a photolabile protecting group (PPG) which blocks its biological function [89, 105, 125]. For these purposes, the PPGs are also referred to as caging groups. The PPGs provide several advantages which makes them employable for a range of regulatory functions.

One such function is also the protection of functional groups in chemical synthesis [143].

In the absence of protection, functional groups introduced in one step are prone to be destroyed in subsequent steps because of their typically high reactivity and sensitivity to changes. To overcome this vulnerability, the functional group is rendered inert by introducing an additional molecular fragment that is inert under the conditions of subsequent steps. This fragment can be removed again after the completion of the synthesis and the original functional group can be restored. A common example would be the protection of a carbonyl group by creating an acetal. In certain biochemical applications, e. g., the solid-phase synthesis of Deoxyribonucleic acid (DNA), Ribonucleic acid (RNA) [107] and oligopeptides [86], chemically introduced and removed protecting groups constitute a critical component. Identification of efficient protecting groups for the given reaction conditions becomes very important.

Photolabile or photoremovable protecting groups form a subgroup of chemical protecting groups, the distinguishing feature being that although their introduction is chemical but the removal is done through a photochemical reaction upon irradiation with UV/vis light. In regular applications, the introduction and removal of protecting groups is done through chemical methods. Removal of the protecting group through photochemical reaction enables a very precise spatial and temporal control within the system [67].

This extent of control is usually not necessary in synthetic applications. PPGs are rather used to investigate complex reaction mechanisms in biological systems [19]. The desired substance, for example, a pharmaceutical drug can be modified with the protecting group to render it inert and then later be released with a laser pulse to monitor the subsequent behaviour of the system. Using this context, the drug deactivated with the protecting group is referred to as a "caged" molecule and the protecting group itself is termed the "photocage", "caging group" or just "cage" for better characterization. The removal process of the protecting group is then referred to as "uncaging".

For applications to biological systems, the design of target caged-compounds has to meet certain desirable properties. Among these, water solubility is the most important requirement since biological processes take place in aqueous media. High water solubility of the photoproduct remaining from the cage is also desirable so as to avoid side effects from precipitation. Moreover, all photoproducts, the substrate and the media must be non-toxic in the system under investigation.

The next point of concern is the minimization of the possible damage to the biological system caused by the light used for uncaging. A high efficiency of the photochemical release would be desirable to ensure a certain amount of unprotected substrate after the interaction with the incident light. Thereafter, the substrate from the protecting group should depart directly from the excited state of the caged system. The wavelength of the "uncaging" light hence should preferably be longer than 300 nm in the visible range. Biological systems, especially DNA and RNA, are prone to significant damage by UV light and this can also lead to unwanted additional photochemical reactions that can interfere with the process under investigation. In view of future medical applications of the cage, the dependence of the wavelength of the incident light becomes even more important. Hence, the role of

PPGs having absorption wavelength in the visible region is crucial to rule out the option of UV light.

Extending to more complex biochemical experiments, the application of PPGs to more than one component of the system under probe may be desired. Here, it is desirable that the different caged compunds release independently from each other. Now the concept of *orthogonal uncaging* [102] is applied. Presently, chemically different PPGs possessing different absorption spectra make this possible. The electronic absorption spectra of these PPGs need to be be sufficiently distinct to be addressed selectively by light. However, this approach has a few disadvantages. Finding two PPGs featuring a high extinction coefficient and a reasonable quantum yield is a considerable challenge as electronic absorption spectra in solution are usually very broad. Furthermore, the two PPGs having absorption maxima that differ enough so as to not excite the other PPG at this wavelength is also very challenging. The other disadvantage is the inevitable byproducts after the use of PPG in the uncaging reaction. This increases the scope of interference of the byproducts with the experiment when two different PPGs are used in the same system compared to when just a single PPG is used.

Now the concept of PPGs and their role in the VIPER experiment stretches to TPA. As discussed before, introduction of TPA brings about incremental amount of efficiency in the excitation processes. It could also help easily meet the requirement of the wavelength of the incident light pulse in uncaging. Due to the doubling of the wavelength of the photons of the incident TPA pulse, the danger posed by the UV light of the possible damage to the biological systems can be easily thwarted. Several classes of photocages which are known to be two-photon active can be considered for the VIPER experiment with TPA. Among these, nitrodibenzofuran (NDBF) [38] and rhodamine [97] are good candidates owing to their excellent TPA characteristics. Section 4.3 contains detailed discussion about rhodamines for their prime role as the donor fragment in molecular dyads exhibiting intramolecular energy transfer. NDBF and synthesis of its derivatives still remain an active area of interest for the development of PPGs.

3.7.1 *Nitrodibenzofuran-based PPGs*

The basic structure of the NDBF is depicted in the left panel of fig. 10. NDBF cages exhibit a broad main absorption band in the 300-400 nm range peaking at around 350 nm subject to the substituent groups. It is one of the great examples of PPGs with TPA characteristics which are cleavable with femtosecond pulse lasers. A red-shifted two-photon-only caging group was successfully synthesized by Becker *et al.* [11] with the addition of a dimethylamino functionality (DMA) at ring position 7. Substitutions of this kind enhance the TPA character as the TPA cross-section of chromophores depends on the length and planarity of the π-electron system and substituent effects [1, 33]. The addition of DMA functionality as a donor increased the push-pull effect and eventually the dipolar character [130].

The synthesized DMA-NDBF had shown to be surprisingly stable under visible-light one-photon excitation. Due to the DMA functionality, the absorption maximum shows a red-shift to the range of 400-450 nm peaking at around 420 nm. The efficiency of uncaging is generally estimated by the product of the uncaging quan-

tum yield and extinction coefficient [1]. Based on other previously reported extensive computational investigations on NDBF-based TPA-active caging compounds, it was found to be safe to assume that an increase in TPA probability can effect an increase in the overall uncaging efficiency.

The DMA-NDBF cage served as a good PPG to be chosen as a starting point for their possible application in the VIPER experiment with TPA. Compared to the parent NDBF, the DMA-NDBF derivative has shown to be 20 times more efficient uncaging group considering that the uncaging quantum yield remains unchanged.

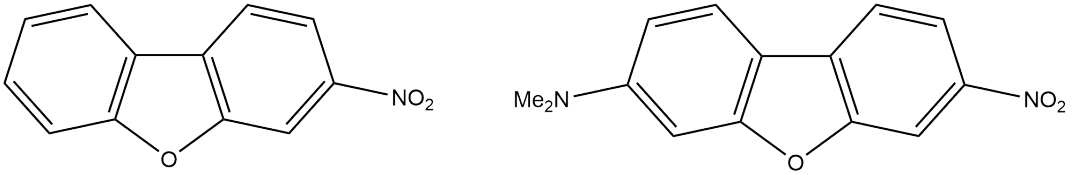

Figure 10: Left: Structure of an unsubstituted nitrodibenzofuran PPG. Right: Structure of DMA-NDBF.

3.7.2 *Rhodamine*

The rhodamine moiety of interest here is the one among the rhodamines investigated for TPA characteristics in Section 4.3. Its parent structure resembles that of commercially available rhodamine 101 (Rho 101). The absorption maximum measured by the spectroscopic collaborators has been measured to be peaking at 572 nm.

Rhodamines are known for their applications as laser dyes and fluorescent probes [75]. Rho 101 being among the most commonly used rhodamines shows an interesting behaviour with pH and solvent polarity [12]. In this work, the theoretical investigations have been carried out in methanol as the solvent. The calculations show the structure to exist in zwitterionic form. On the other hand, the formation of lactone structure negates the purpose of the theoretical investigation. The lactone structure shows differences in photophysical properties and shows reduction in the wavelength of electronic absorption due to interruption in the π-conjugation. Comprehensive discussions will be found in Section 4.3 on rhodamines especially with regards to their TPA character.

The rhodamine depicted in fig. 11 has been preliminarily investigated upon by experimental collaborators for their potential application in VIPER spectroscopy with TPA through their pump-probe setup. The investigation displayed a positive VIPER signal for the rhodamine moiety. In several of the reported works on another commercially available and most commonly used rhodamine 6G (Rho 6G) by Milojevich *et al.* where surface-enhanced hyper-Raman scattering (SERS) has been employed for measuring TPA related properties, it has been found that the non-Condon effects or the first-order HT effects have a severely dominant role when calculating the TPA spectra [97]. An interestingly similar discussions on the results obtained on the Rho 101-based rhodamine would follow in further sections.

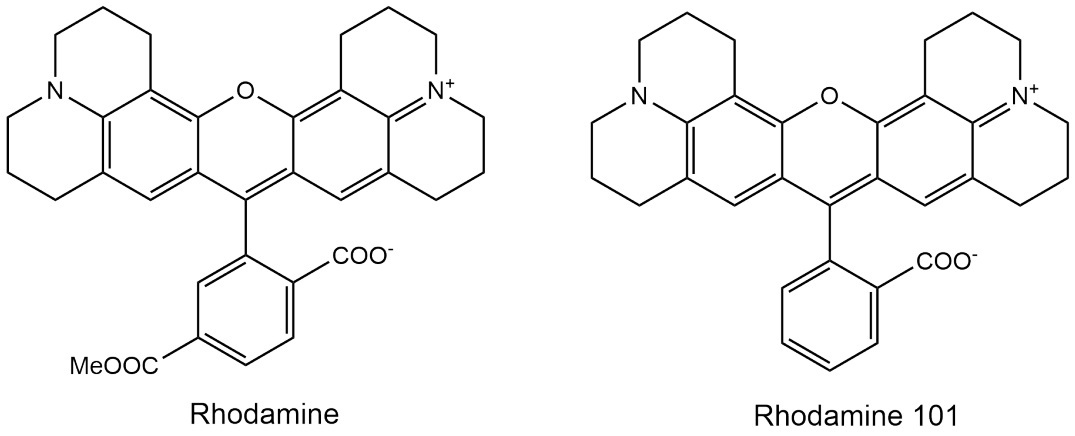

Figure 11: Structure of rhodamine with the parent structure being that of Rho 101.

3.8 COMPUTATIONAL PROCEDURE

All electronic structure calculations were performed with the *Gaussian16* program, revision *B.01* [49] unless noted otherwise. Ground state calculations involving geometry optimization and frequency analysis were performed using DFT while its time-dependent version TDDFT was employed for the calculation of electronically excited states. Analytic first and second derivatives were available for computation of equilibrium structures and vibrational frequencies respectively in the ground state. However, due to the fact that only analytic first derivatives are available in the excited state, vibrational frequencies were therefore obtained by numerical differentiation of analytic gradients along atomic Cartesian coordinates. Through the employment of PCM [132], solvent effects could be accounted for as the analytic gradients are available in the ground as well as the excited state [119]. Usage of fine integration grids (`int=ultrafine`) and assignment of tight optimization criteria for geometry optimizations were opted for all electronic structures.

For calculating the TPA cross-sections of the electronically excited states, quadratic response calculations were performed using 2016 version of DALTON [2] package. The ground state equilibrium geometry optimized from the *Gaussian16* calculations was the reference structure for these calculations.

In order to compute the spectra, the excited state PES was modeled using the AH or VG approach [44], subject to feasibility of the excited state equilibrium structure optimization. In the AH model, the excited state PES expansion to second order is around its own minimum. On the other hand, the VG approach is modeled by the expansion of the excited state PES around the equilibrium geometry of the ground state. Then the approximation is made by a mere shift in the ground state PES. With a new development version of the *FCclasses* code [111], the time-independent (TI) TPA vibronic spectra could also be calculated. The resulting spectra were convoluted with a Gaussian lineshape with a Half Width at Half Maximum (HWHM) of 0.01 *eV*, unless noted otherwise. In these same TI spectra, the number of FC integrals per class $N_{max} = 10^8$ and a maximum quantum number for classes C_1 and C_2 of $w_{max}^{(C_1)} = 30$ and $w_{max}^{(C_2)} = 25$, respectively were assigned for calculations.

Now the attainment of first-order HT spectra for both OPA as well as TPA has to do with the derivatives of the electronic transition dipole moment μ and two-

photon transition matrix elements S_{ij}, respectively. It can rather be detailed case by case:

1. OPA-HT: The *Gaussian16* version provides for numerical computation of second derivatives of the TDDFT excited-state energy needed for the harmonic analysis at the excited state equilibrium geometry through an additional input keyword `Freq=Numer`. A stand-alone Python script computes the derivatives of μ after reading from *Gaussian* output its values (written with a precision of 10^{-4} a.u.) at the 6N geometries obtained by positive and negative displacements (10^{-3}Å) of each of the 3N Cartesian coordinates [116].

2. TPA-HT: Here, the positive and negative displacements of the ground state equilibrium geometry (10^{-3}Å) of each of the 3N Cartesian coordinates needs to be manually executed leading to the creation of 6N separate geometries. A stand-alone Python script generates 6N geometries from the optimized ground state equilibrium geometry from the *Gaussian* calculation. After the quadratic response calculations with DALTON package of these 6N geometries, another stand-alone Python script computes the derivatives of S_{ij} after reading from the DALTON outputs the values (written with a precision of 10^{-6} a.u). These derivatives in terms of normal coordinates are further transformed into derivatives in terms of normal modes [77] to be finally readied as the input for the calculation of HT spectra with the development version of *FCclasses*.

3.9 RESULTS

This section deals with the computation of the vibrationally resolved electronic spectra of the investigated compounds DMA-NDBF and rhodamine. Therefore it is an extension of the previous implementation by Jan von Cosel [28] by TPA inclusive of a consideration of first-order HT effects. The description follows with vibrationally resolved electronic spectra, the effect of vibrational pre-excitation and the resulting VIPER effect.

The criteria for a given normal mode to be suitable for VIPER excitation are several: A high IR absorption intensity should be featured by the mode so that a sufficient population of the excited vibrational state can be achieved. The separation in the spectral domain should be wide enough in order to enable its selective excitation with the narrow-band IR pump pulse that has a Full Width at Half Maximum (FWHM) of about 10 cm^{-1} to 20 cm^{-1}, especially if multiple species have presence in the sample. Naturally, the effect of its excitation should have a high impact on the low-energy edge of the absorption spectrum for a large VIPER effect.

The complete setup for computational procedure has been initially verified by testing with the model molecules reported by Macak *et al.* [83, 84] and also for pyrimidine [82] in which the simulation of vibrationally resolved electronic TPA spectra accounting for FC and HT contributions have been executed using the linear vibronic coupling (LVC) model.

3.9.1 *Dimethylamino-nitrodibenzofuran*

As detailed earlier, the dimethylamino derivative of the NDBF PPG shows a red-shifted OPA and TPA compared to the NDBF group. Red-shifting of the light-induced uncaging becomes less harmful and deeper tissue penetration can also be achieved. Uncaging in the phototherapeutic window $\sim 650 - 950 nm$ is highly desirable and DMA-NDBF is a promising candidate to develop a good strategy to achieve this uncaging. Its structure has been depicted in the right panel of fig. 10. It seemed as a good starting point to probe and also to set as a benchmark system for VIPER experiment with TPA. DMA-NDBF consists of 31 atoms possessing 87 normal modes.

From the reference literature of Becker *et al.* [11], the experimental OPA spectra is shown by fig. 12. The -CH_2OH substituent needs to be taken out of consideration which is the linker substituent that is of importance when the stage of uncaging is reached. The OPA spectrum features an absorption maximum at 420 nm.

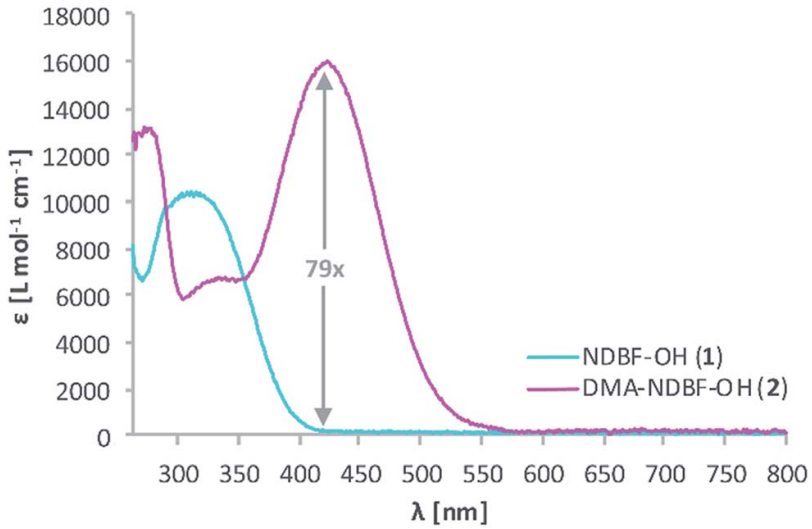

Figure 12: Experimental OPA spectra of DMA-NDBF in comparison with that NDBF. Due to addition of the $N(Me)_2$ moiety, the absorption maximum of the DMA-NDBF is shifted to 420 nm. The spectra was measured in dimethyl sulphoxide (DMSO). Reproduced from [11] with permission from the Royal Society of Chemistry.

All electronic structure calculations on DMA-NDBF were performed with the global hybrid B3LYP functional combined with the Def2-TZVP triple-ζ basis set in vacuum. However, a proper benchmarking has been attempted when calculating the vertical excitation energies at the B3LYP/Def2-TZVP optimized ground state geometry.

3.9.1.1 *Vibrational properties*

The frequency analysis confirms that the optimized ground state geometry corresponds to a real minimum without negative frequency. Fig. 13 shows the IR spectrum computed for the ground state geometry of DMA-NDBF. The normal modes of vibration with high IR absorption intensity lie in the region between 1000 and 1800 cm^{-1}.

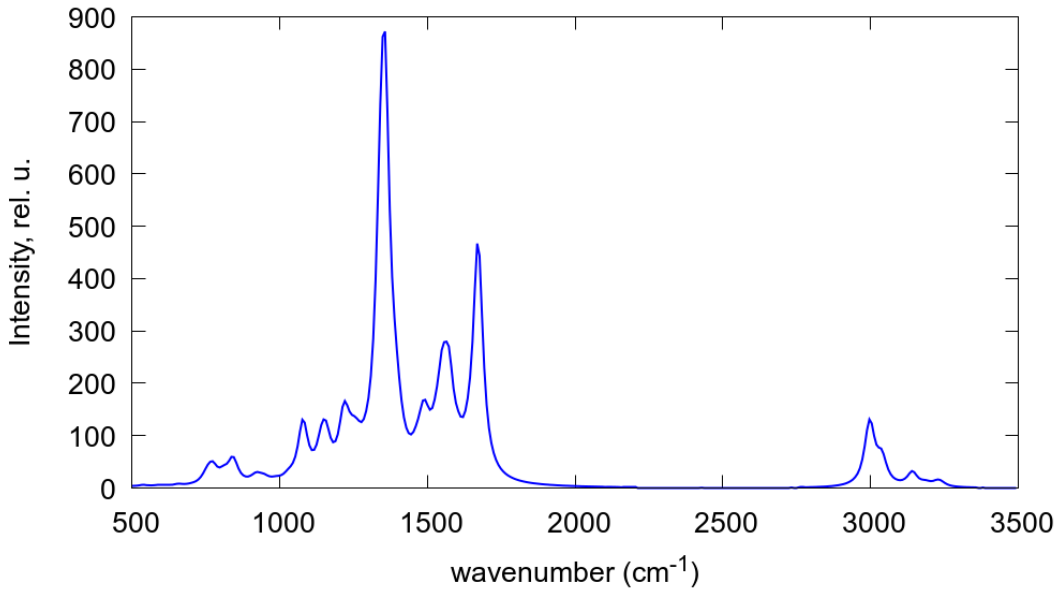

Figure 13: Computed IR spectrum of DMA-NDBF obtained at the B3LYP/Def2-TZVP level in vaccum. Vibrational transitions were convoluted with a lorentzian broadening function with a HWHM of 20 cm^{-1}.

As discussed in the beginning of this section, the normal modes should have a high IR absorption intensity in order to provide an efficient VIPER transition. Taking a closer look at the IR spectrum, three normal modes with high IR absorption intensity could be identified which are listed in table 1.

Table 1: Computed vibrational frequencies of the normal modes of DMA-NDBF obtained at the B3LYP/Def2-TZVP level in vaccum.

Mode	Frequency (cm^{-1})
Ring mode 1	1339
NO_2 bend	1355
Ring mode 2	1670

Among the identified normal modes, there are two ring modes and a nitro-bending mode which exhibit high IR absorption intensity. These could be the potential normal modes for efficient VIPER excitation according to the criteria but the dimensionless displacement plays the most important role in checking the VIPER activity of these normal modes. Higher dimensionless displacment consequently leads to higher Huang-Rhys factor. In the forthcoming process of computation of the vibrationally resolved electronic spectra with *FCclasses*, the relevant vibrational modes for VIPER excitation could be better identified as a measure of their dimensionless displacements.

3.9.1.2 *Electronic excitations and quadratic response*

The lowest singlet excited state of DMA-NDBF has a significant oscillator strength corresponding to a $\pi - \pi^*$-transition within the conjugated π-system from the highest occupied molecular orbital (HOMO) to the lowest unoccupied molecular orbital (LUMO). Fig. 14 depicts the frontier orbitals in the first electronic state. Both the frontier orbitals are delocalized over the entire π-system, however, the LUMO has a slightly lower contribution at the dimethyl amino group.

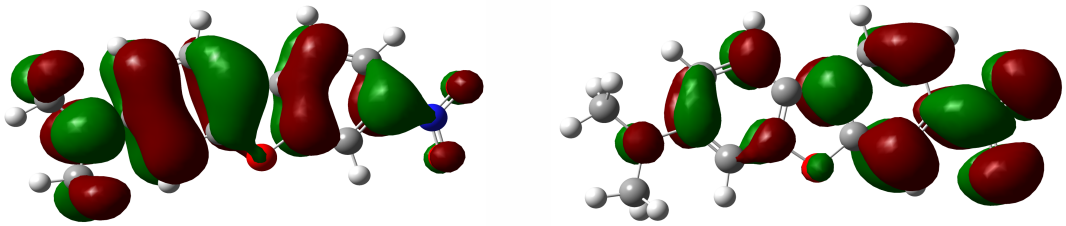

Figure 14: HOMO (left) and LUMO (right) of DMA-NDBF obtained at the B3LYP/Def2-TZVP level in vacuum.

The benchmark of the vertical excitation energies E_V, the oscillator strength f, and the two-photon cross-section σ_{TP} in Göppert-Mayer (GM) units of the $S_0 \rightarrow S_1$ transition with different DFT functionals are listed in table 2. The S_1 state due to its oscillator strength and high two-photon cross-section is determined as both one- and two-photon allowed state.

Table 2: Vertical excitation energies E_V, oscillator strength f and two-photon cross-section σ_{TP} of the lowest excited singlet state of DMA-NDBF obtained with different DFT functionals along with Def2-TZVP basis set.

DFT functional	$E_V(eV)$	f	σ_{TP} (GM)
B3LYP	2.99	0.47	196
BHandHLYP	3.73	0.78	211
CAM-B3LYP	3.70	0.75	201

The next table 3 lists out the values of the vertical and adiabatic electronic excitation energies and oscillator strengths for the same $S_0 \rightarrow S_1$ transition. The separation in energies of the electronic states at the ground state equilibrium structure (the FC point) is referred to as the vertical excitation energy E_V whereas the separation in energies of the minima of the ground and excited states is referred to as the adiabatic excitation energy E_{ad}. By optimizing the geometry in the excited state, E_{ad} is calculated taking the difference between the absolute energies of the S_1 in this structure and the S_0 at the FC point. The difference between E_V and E_{ad} is then known as the molecular reorganization energy in the excited state which is understood as the excess vibrational energy contained in the system after a vertical transition into the excited state.

The experimentally observed maximum absorption of 420 nm of the DMA-NDBF-OH (refer fig. 12) corresponds to an excitation energy of 2.95 eV. It must be noted that the experimental spectrum was measured in DMSO. On comparison with the computed excitation energies in vaccum, the value obtained with B3LYP functional

Table 3: Electronic excitation energies (vertical E_V and adiabatic E_{ad}) and oscillator strengths f (at the ground and excited state equilibrium geometry, respectively) of the lowest excited state of DMA-NDBF obtained at the B3LYP/Def2-TZVP level in vacuum.

$E_V(eV)$	$E_{ad}(eV)$	f_g	f_e
2.99	2.75	0.47	0.42

is close to this with a small blue-shift of 0.04 eV but very large blue-shifts with values obtained from BHandHLYP and CAM-B3LYP are evident. The oscillator strength, a dimensionless quantity indicative of the intensity of the transition, differs very slightly between the ground and excited state equilibrium structure in vacuum.

3.9.1.3 *Vibrationally resolved electronic spectra*

The computed one-photon vibrationally resolved electronic absorption spectra of DMA-NDBF is displayed in fig. 15. The 0-0 transition is always the strongest transition except for the HT part. The HT effects in the total FCHT spectrum is negligible or very insignificant to say the least. The HT contributions are able to enhance the intensity of the vibronic transitions following the 0-0 transition only very slightly but no new peaks or changes in the lineshape can be observed. As can be seen from fig. 15, the HT spectrum had to be scaled up by a factor of 30 in order to make its effects clearly visible when compared to the FC contributions.

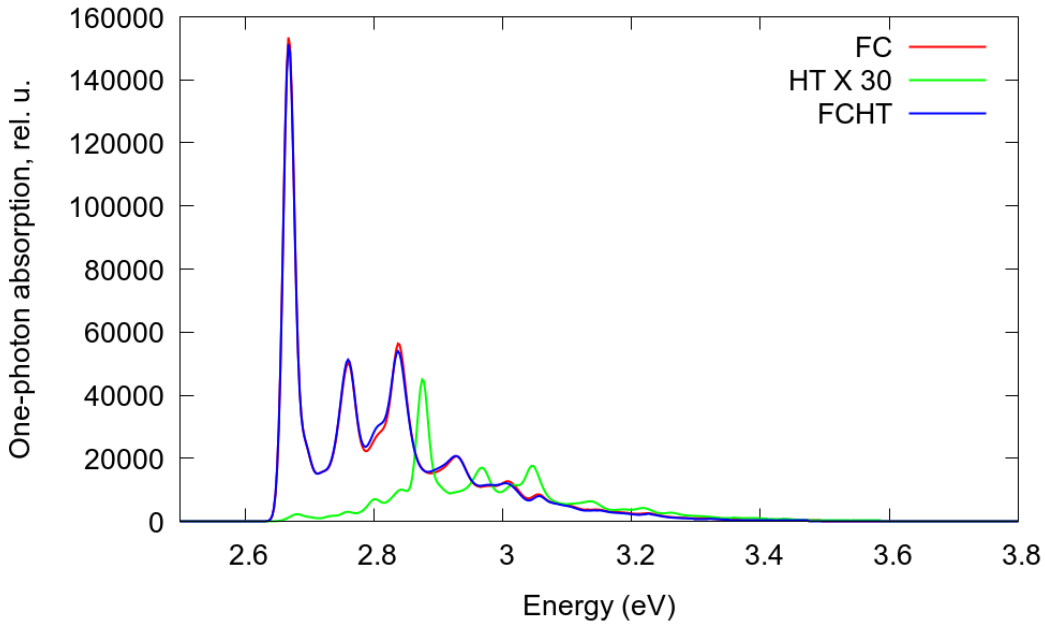

Figure 15: Vibronically resolved OPA spectra of DMA-NDBF in vacuum obtained at the B3LYP/Def2-TZVP level with the TI approach using the AH model.

Fig. 16 shows the computed two-photon vibrationally resolved electronic absorption spectra of DMA-NDBF. The 0-0 transition is always the strongest transition as seen in the case of OPA (ref. fig. 15) followed by a series of vibronic transitions

with decreasing intensities. The HT contributions are once again found to be very small, however, they are seen to slightly enhance the intensity of the 0-0 transition. On the other hand, no significant effects of the HT contributions in the total FCHT spectra can be observed. In the case of TPA, the HT spectrum needed to be scaled by a factor of 200 to bring out its visiblility (ref. fig. 16).

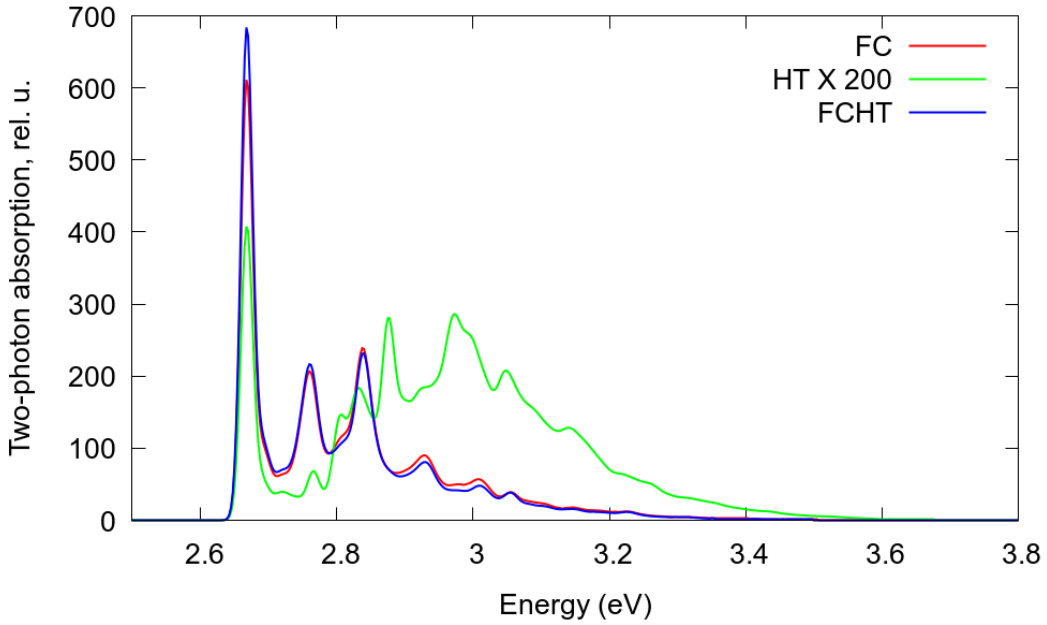

Figure 16: Vibronically resolved TPA spectra of DMA-NDBF in vacuum obtained at the B3LYP/Def2-TZVP level with the TI approach using the AH model.

In both the one-photon and two-photon vibrationally resolved electronic spectra, the lineshapes remain the same and the intensities of the vibronic transitions are almost the same. The HT contributions for both OPA as well as TPA are very small. Since the S_1 is known to be one- and two-photon allowed, the effects of HT contributions are therefore insignificant as it is typical for electronically-allowed transitions.

3.9.1.4 *Influence of vibrational pre-excitation*

An analysis of all the normal modes of vibration reveals their probable VIPER activity as a measure of the dimensionless displacements. As per the elementary critera of looking for the the normal modes in the high-frequency region, the calculations with the TI method bring out two normal modes of vibration which have significantly high dimensionless displacements. Table 4 enlists the displacement vector δ (in mass-weighted coordinates) along with the IR frequency ν of the probable VIPER-active modes.

Visualization of the NO_2 bend and the ring mode as depicted in fig. 17 shows the corresponding displacement vectors. Out of these, the NO_2 bend mode has a high IR absorption as discussed before in Section 3.9.1.1. The ring mode on the other hand shows a very low IR absorption but has relatively higher dimensionless displacement than all other vibrational modes. Based on this calculation, the one- and two-photon vibrationally resolved electronic absorption spectra of DMA-NDBF

Table 4: Dimensionless displacements and the IR frequencies of the probable VIPER-active modes of DMA-NDBF obtained at the B3LYP/Def2-TZVP level in vaccum.

Mode	δ	$\nu(cm^{-1})$
NO_2 bend	0.7637	1355
Ring mode	0.3734	1374

are computed in order to investigate the effects of pre-exciting the NO_2 bend and the ring modes vibrationally.

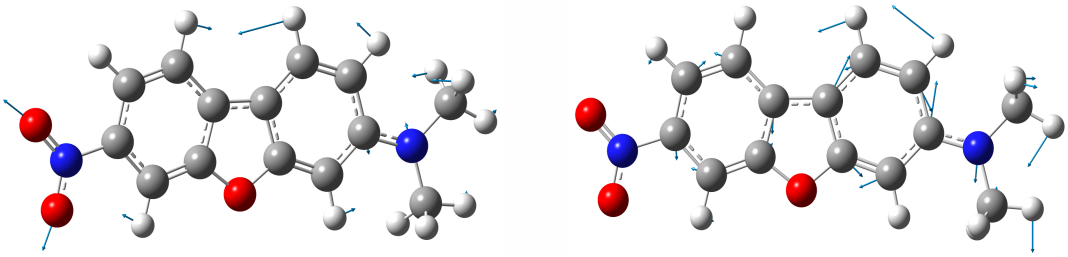

Figure 17: Displacement vectors of the NO_2 bend mode (left) and the ring mode (right) of DMA-NDBF obtained at the B3LYP/Def2-TZVP level in vacuum.

Fig. 18 shows the computed vibronic spectra with OPA along with VIPER excitations of the NO_2 bend and the ring mode. It is clearly visible looking at these computed spectra that the NO_2 bend mode yields the strongest M-0 transition in the two selected modes. Hence, the highest VIPER activity is of the NO_2 bend mode. The HT contributions do not affect the lineshape of the total FCHT spectra even in the case of pre-excitations as observed for 0K without pre-excitation.

Fig. 19 shows the computed vibronic spectra with TPA along with VIPER excitations of the NO_2 bend and the ring mode. The findings in TPA are seen to be the same as that of OPA. Here too, the NO_2 bend is the most VIPER-active mode showing the highest intensity at the point of pre-excitation. The ring mode shows a slightly different behaviour especially in HT spectra. The ring mode in the OPA HT spectra does not show any pre-excitation signal but in the TPA HT spectra, the pre-excitation could be clearly seen. The overall behaviour of the pre-excited modes is the same in both OPA and TPA.

Direct excitation of the vibrational modes makes the vibronic effects much more visible. The intensity of the higher energy tail of the spectrum increases. In general, an increase in width of the spectrum upon pre-excitation could be obtained. The VIPER excitation leads to additional contributions in the lower-energy region. The main inference to be drawn here is that there is a red-shift of the UV/vis or the electronic TPA spectrum and rather a broadening in both directions could be achieved.

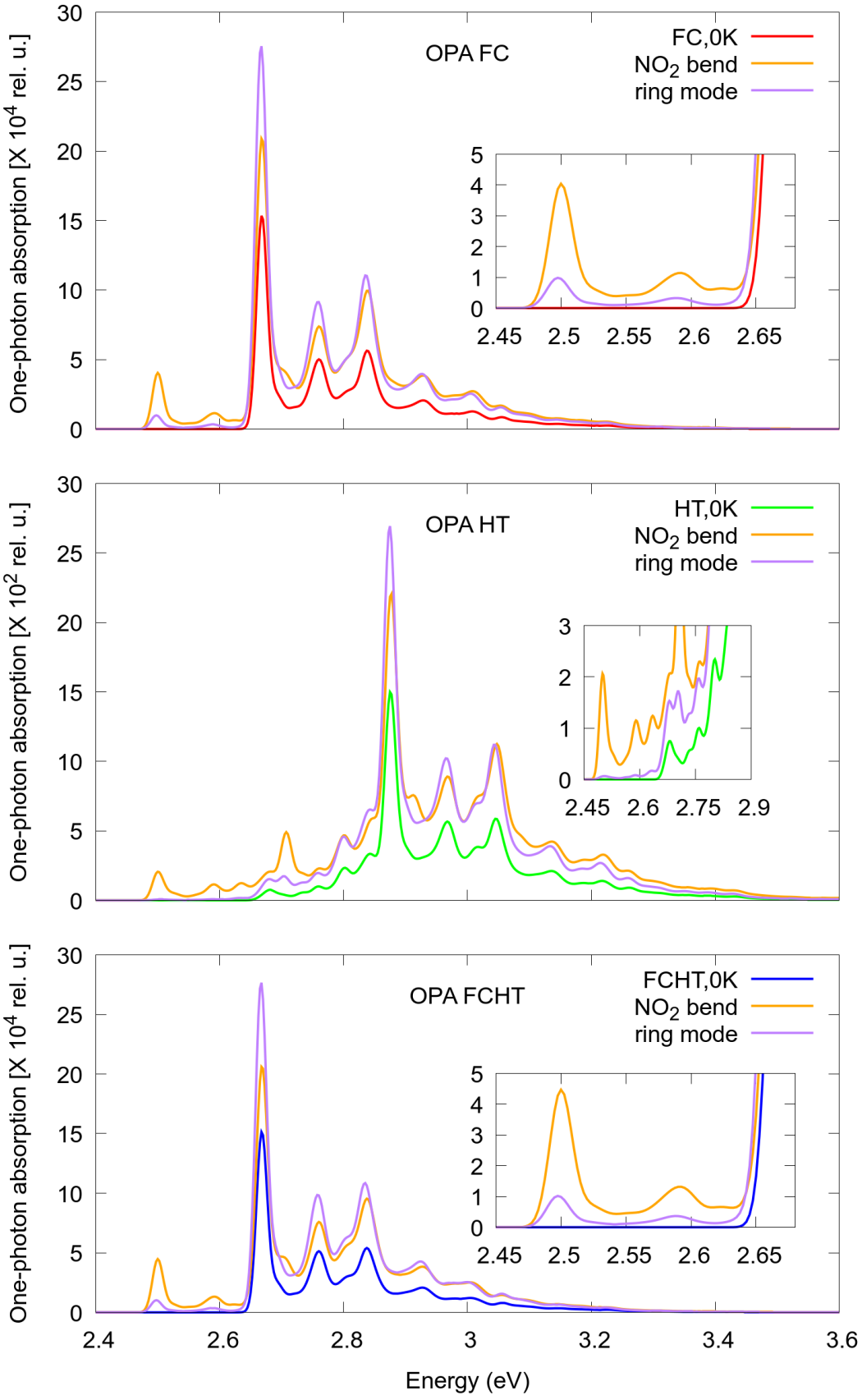

Figure 18: Computed OPA spectra of DMA-NDBF in vacuum obtained with the TI method with FC (top), HT (middle) and total FCHT (bottom) effects at the B3LYP/Def2-TZVP level with vibrational pre-excitation of NO_2 bend (orange) and ring mode (purple).

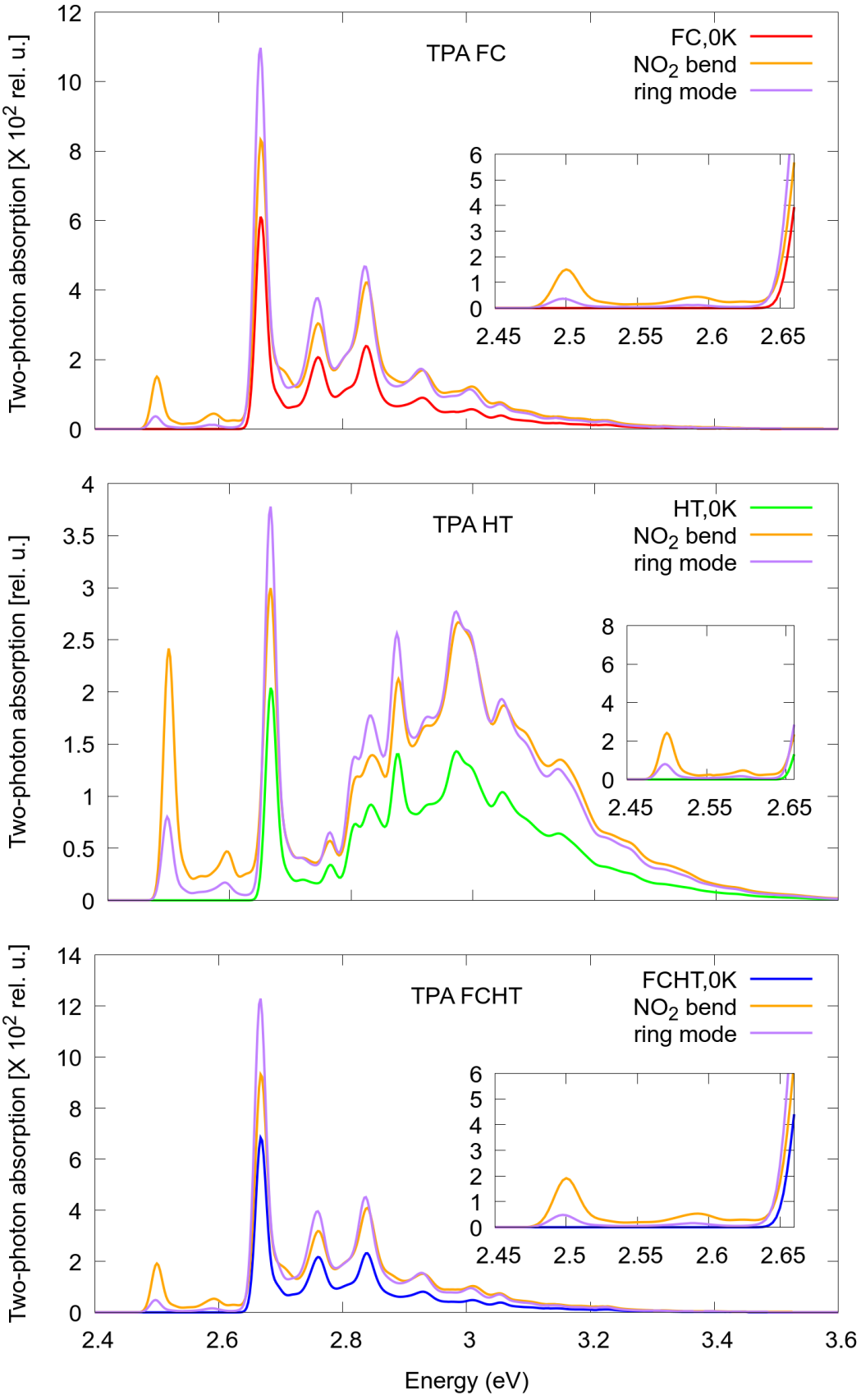

Figure 19: Computed TPA spectra of DMA-NDBF in vacuum obtained with the TI method with FC (top), HT (middle) and total FCHT (bottom) effects at the B3LYP/Def2-TZVP level with vibrational pre-excitation of NO_2 bend (orange) and ring mode (purple).

3.9.2 *Rhodamine*

The rhodamine whose molecular structure has been depicted in fig. 11 is also a two-photon active molecule of interest for the VIPER experiment with TPA. It is a large system to investigate where there are 73 atoms leading to 213 normal modes of vibrations. Due to its size, it becomes computationally challenging to investigate keeping in mind the process involved especially for calculating HT contributions.

The long-range corrected CAM-B3LYP functional with the 6-31G* basis set was employed in all electronic structure calculations on rhodamine. PCM solvation model was invoked to treat the solvent effects of water.

3.9.2.1 *Vibrational properties*

The optimized ground state geometry is confirmed to be corresponding to a real minimum without negative frequency by the frequency analysis. The IR spectrum computed for the ground state geometry of rhodamine is shown in fig. 20. As expected from the commonly observed trend, the normal modes of vibration with high IR absorption intensity lie in the 1000-2000 cm^{-1} region.

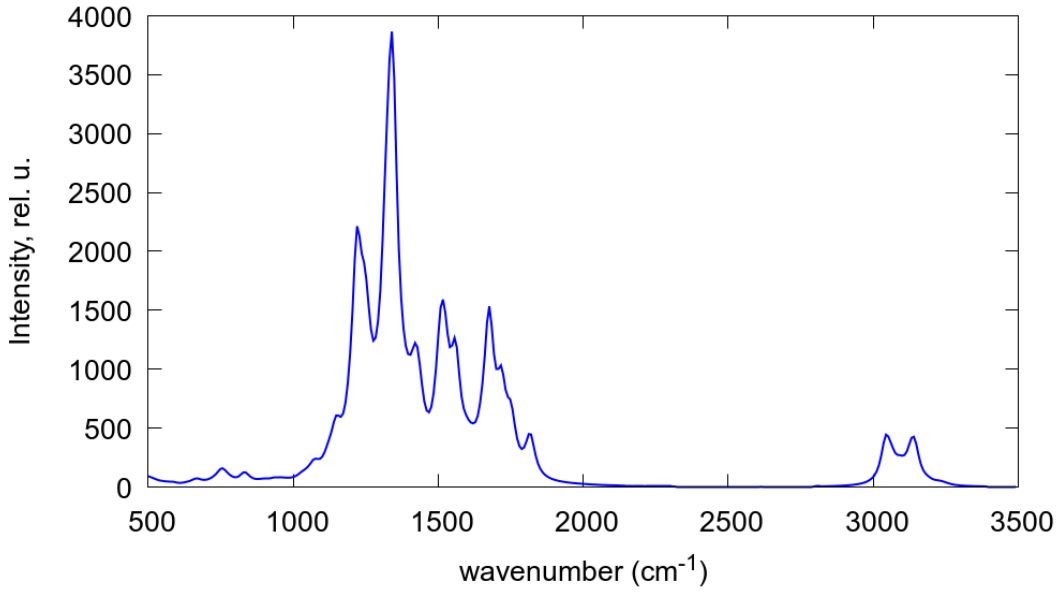

Figure 20: Computed IR spectrum of rhodamine obtained at the CAM-B3LYP/6-31G* level in water. Vibrational transitions were convoluted with a lorentzian broadening function with a HWHM of 20 cm^{-1}.

A closer look at the IR spectrum reveals several such prominent vibrational modes with distinctly high IR absorption. Table 5 lists out the vibrational modes with high IR absorption. The dimensionless displacements of the normal modes will be the determining factor when checking for suitability for VIPER excitation.

3.9.2.2 *Electronic excitations and quadratic response*

The lowest singlet excited state of rhodamine involves a $\pi - \pi^*$-transition within the conjugated π-system from the HOMO to the LUMO. As seen in fig. 21, the frontier

Table 5: Computed vibrational frequencies of the normal modes of rhodamine with high IR absorption intensity obtained at the CAM-B3LYP/6-31G* level in water.

Mode	Frequency (cm^{-1})
C-H bend 1	1219
ring mode 1	1246
C-H bend 2	1318
ring mode 2	1345
C-H bend 3	1559
ring mode 3	1675

orbitals are delocalized over the entire π-system with a lower contribution at the amino substituent groups in the LUMO. The lowest electronically excited state S_1 is a bright state with a high oscillator strength.

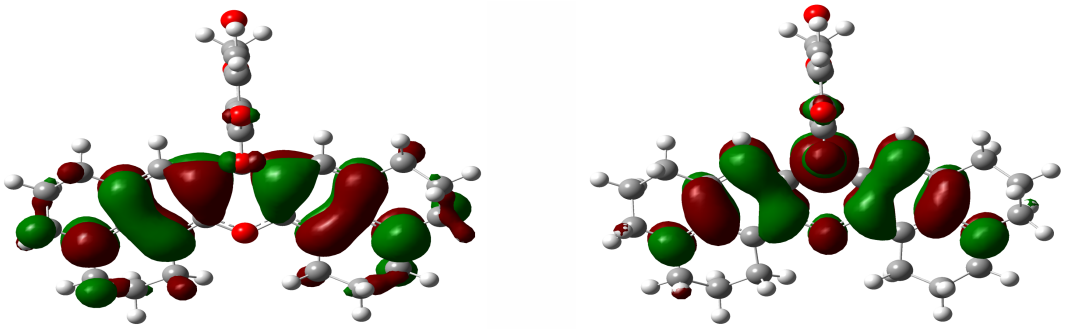

Figure 21: HOMO (left) and LUMO (right) of rhodamine obtained at the CAM-B3LYP/6-31G* level in water.

The following table lists the computed properties of the electronic $S_0 - S_1$-transition of rhodamine. An experimentally measured absorption maximum of 572 nm in methanol is known which then corresponds to an excitation energy of 2.16 eV. The oscillator strength increases substantially upon going to the excited state minimum which could be attributed to the use of the equilibrium solvation model.

Table 6: Electronic excitation energies (vertical E_V and adiabatic E_{ad}), oscillator strengths (at the ground f_g and excited state f_e equilibrium geometry, respectively) and the TPA cross-section of the lowest excited state of rhodamine obtained at the CAM-B3LYP/6-31G* level in water.

$E_V(eV)$	$E_{ad}(eV)$	f_g	f_e	σ_{TP} (GM)
2.89	2.47	1.03	1.24	23.1

When the optimized geometries of ground and excited state minima are aligned on visualization, a large root mean square deviation (RMSD) of around 0.47 Å is found. This means that the minima with respect to the states are situated quite far apart which makes it difficult to estimate the overlap integrals. This leads to the VG or the LVC model as the better choice to compute the vibrationally resolved electronic spectra rather than the adiabatic model. The vertical model as discussed

earlier has to do with the linear term in the expansion of the final state PES around the equilibrium geometry of the ground state.

3.9.2.3 *Vibrationally resolved electronic spectra*

The vibrationally resolved electronic OPA spectra of rhodamine computed in water are shown in fig. 22. The 0-0 transition is seen to be the strongest in case of FC approximation. The shoulder that occurs in the FC spectrum indicates a presence of a nonzero contribution from the FC term to the OPA spectrum. A negligible change is observed on inclusion of HT coupling as there is a very weak contribution by the HT term to the OPA spectrum. This is also evident in the fig. 22 as the intensities of the pure HT contributions had to be scaled up by a factor of 50 in order to make its effects visible. The total FCHT spectrum with FC and HT vibronic couplings together is pre-dominantly the FC spectrum with a slight enhancement in intensities.

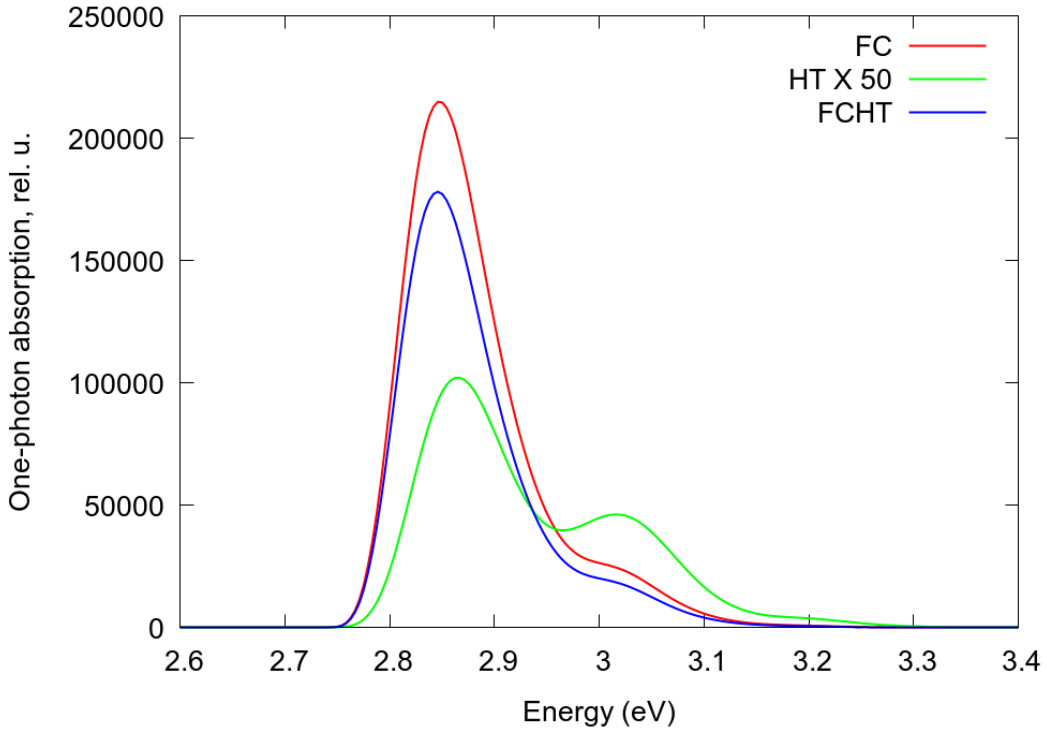

Figure 22: Vibronically resolved OPA spectra of rhodamine obtained at the CAM-B3LYP/6-31G* level in water with the TI apporoach using the VG model.

The TPA picture presents a totally different and unexpected behaviour from that of the OPA. The TPA spectrum with only FC terms is the same in terms of intensities and the lineshape as that of OPA FC spectrum. The 0-0 transition is the strongest in the FC vibronic spectrum and the non-zero contributions have an insignificant impact. However, the inclusion of HT coupling terms completely changes the picture. The HT only spectrum is dominated by two strong non-zero transitions as can be seen in fig. 23. The shoulder at around 2.98 eV appears to be a stronger transition than the preceding transition at 2.87 eV. The total FCHT spectrum is a replica of the HT only spectrum and it can be seen in fig. 23 again that the

HT only and the FCHT total spectra are similar. This comparison of contributions from the FC and HT vibronic couplings implies that the full understanding of the TPA spectrum is achievable through the use of HT vibronic coupling terms.

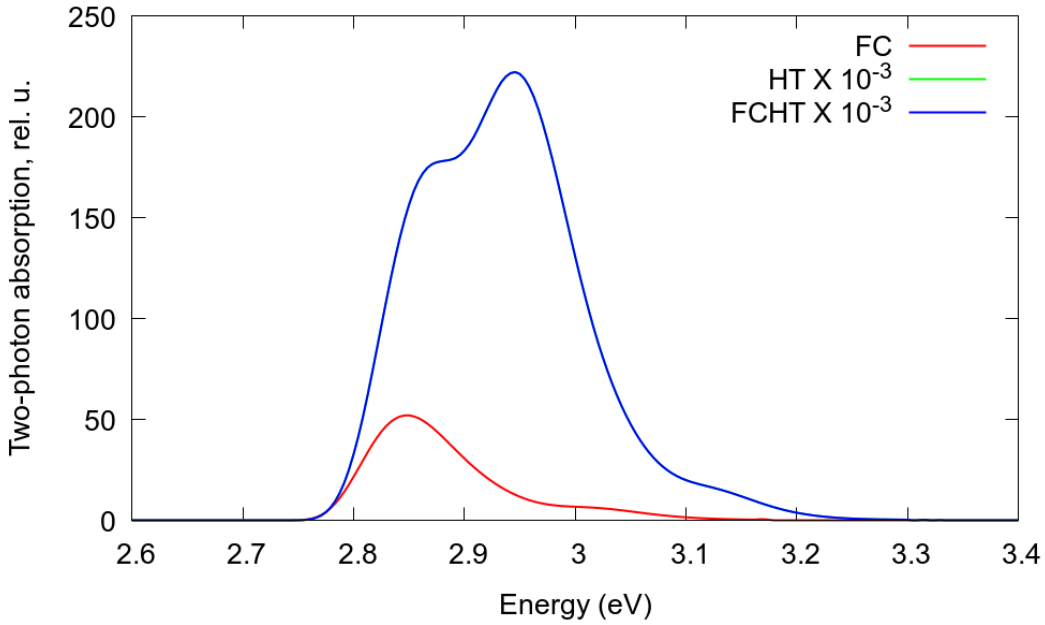

Figure 23: Vibronically resolved TPA spectra of rhodamine obtained at the CAM-B3LYP/6-31G* level in water with the TI approach using the VG model.

The interesting and unusual finding can now also be supported by a similar work by Milojevich *et al*. on the rhodamine 6G molecule [97]. In detail, the OPA and TPA vibronic spectrum are computed and complemented by the surface-enhanced hyper-Raman (SEHRS) spectra. With the help of these available findings, the mechanism of vibronic enhancement can be elucidated by the analysis of molecular orbital changes in the non-linear transitions. Referring back to the orbital visualizations in fig. 21, it could be seen that the LUMO appears symmetric whereas the HOMO appears anti-symmetric. Therefore, an excitation from HOMO to LUMO is one-photon allowed but not two-photon allowed due to the change in symmetry. In the $S_0 - S_1$-transition, one side of the xanthene ring acts as an electron-donating group and utilizes the π backbone of the of the xanthene structure to transfer electron density to the other side of the xanthene ring acting as an electron-accepting group. In this way, the rhodamine behaves like a push-pull chromophore where the presence of donating and accepting groups enhances the non-linear optical characteristics. The work by Milojevich & co-workers explains in greater detail the push-pull character of rhodamine 6G with the help of resonance hyper-Raman experiments.

3.9.2.4 *Influence of vibrational pre-excitation*

The measure of the dimensionless displacements reveals the VIPER activity of the normal modes of vibration. An analysis through the calculations with the TI method finds no significantly high dimensionless displacements of the normal modes in the high frequency region. There are two probable ring modes which could be VIPER-active enlisted in the following table 7.

Table 7: Dimensionless displacements and the IR frequencies of the probable VIPER-active modes of rhodamine obtained at the CAM-B3LYP/6-31G* level in water.

Mode	δ	$\nu(cm^{-1})$
Ring mode 1	0.1417	1547
Ring mode 2	0.2231	1563

The corresponding displacement vectors of the ring modes are depicted in fig. 24. These ring modes do not appear among the normal modes with high IR absorption discussed earlier in Section 3.9.2.1.

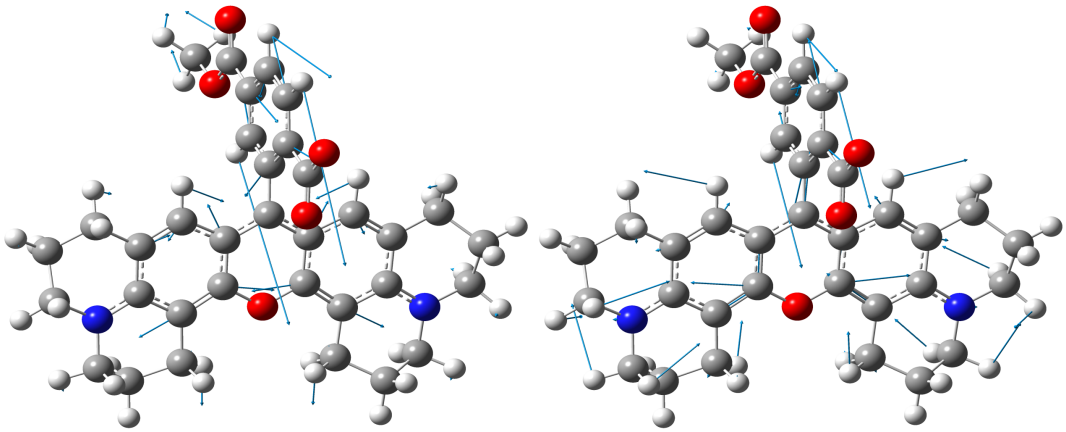

Figure 24: Displacement vectors of the ring distortion modes of rhodamine obtained at the CAM-B3LYP/6-31G* level in water.

Although they have very low IR absorption they have higher magnitude of the dimensionless displacements based on which the vibrationally resolved electronic absorption spectra of rhodamine has been calculated. The effects of pre-excitation of the ring modes have been simultaneously investigated. Fig. 25 shows the computed vibronic spectra with OPA along with vibrational pre-excitation of the ring modes. It can be seen that the intensities of the electronic absorption spectra have been enhanced manifold after the pre-excitation of the ring modes. The HT contributions do not effect any change in the lineshape of the total FCHT spectra in the case of pre-excitations too as already observed for 0K.

Fig. 26 depicts the computed vibronic spectra with TPA inclusive of the vibrational pre-excitation of the ring modes. As seen in the 0K picture, the TPA spectrum is essentially the TPA HT spectrum. However, the effect of pre-excitation is merely the manifold enhancement of the intensities of the transition. In both the OPA and TPA spectra, the intensities of the pre-excitation of the ring modes are very low. Hence, the conclusion to be drawn is that the ring modes display a very low VIPER activity.

Here too, like in the case of DMA-NDBF, it could be inferred that the direct excitation of the normal modes of vibration makes the vibronic effects much more visible. As detailed before, following observations are made for rhodamine as well: increase in intensity of the higher energy tail of the spectrum, increase in the width

of the spectrum upon pre-excitation, additional contributions in the lower energy region due to VIPER excitation.

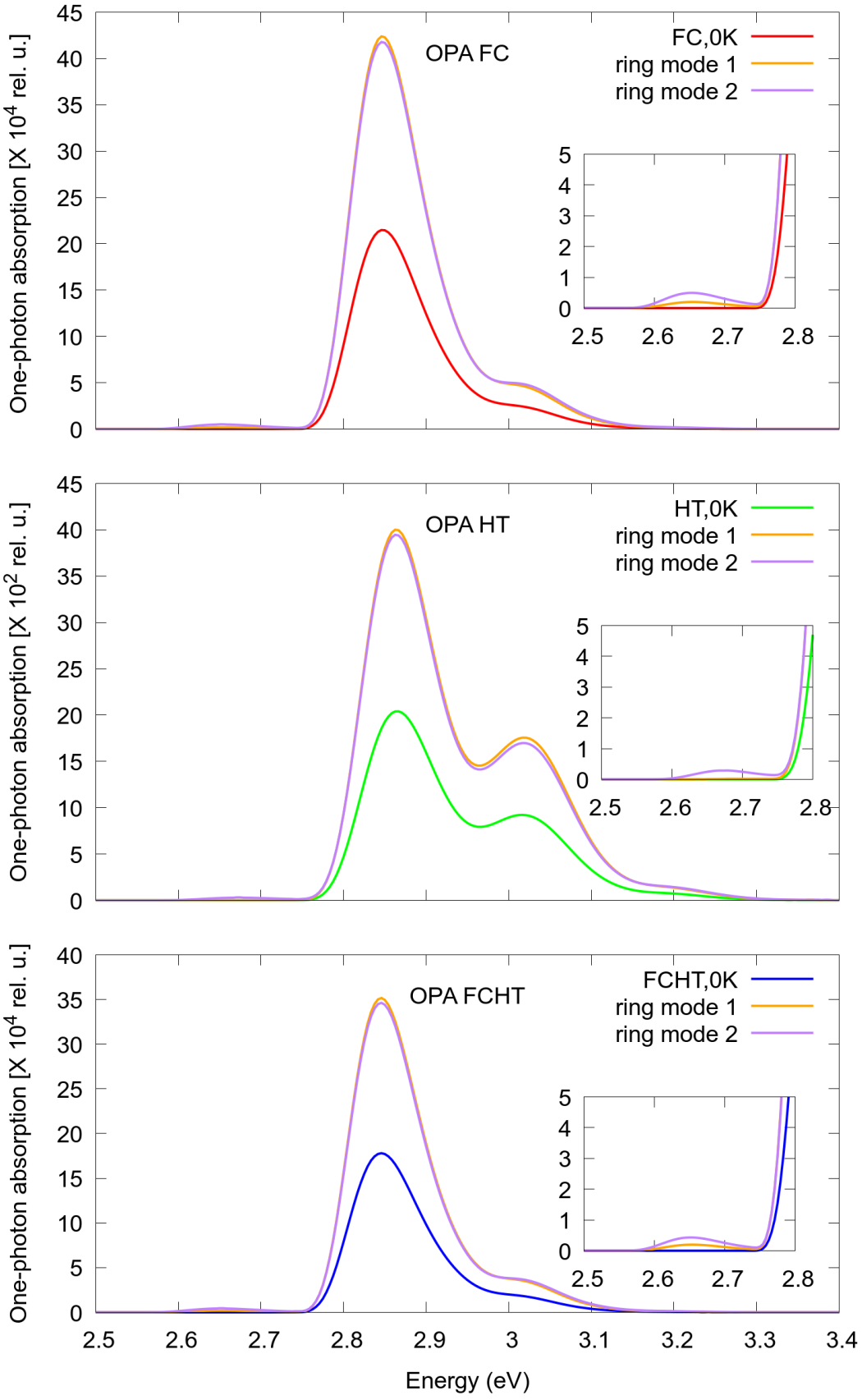

Figure 25: Computed OPA spectra of rhodamine in water obtained with the TI method with FC (top), HT (middle) and total FCHT (bottom) effects at the CAM-B3LYP/6-31G* level with vibrational pre-excitation of ring modes (orange and purple).

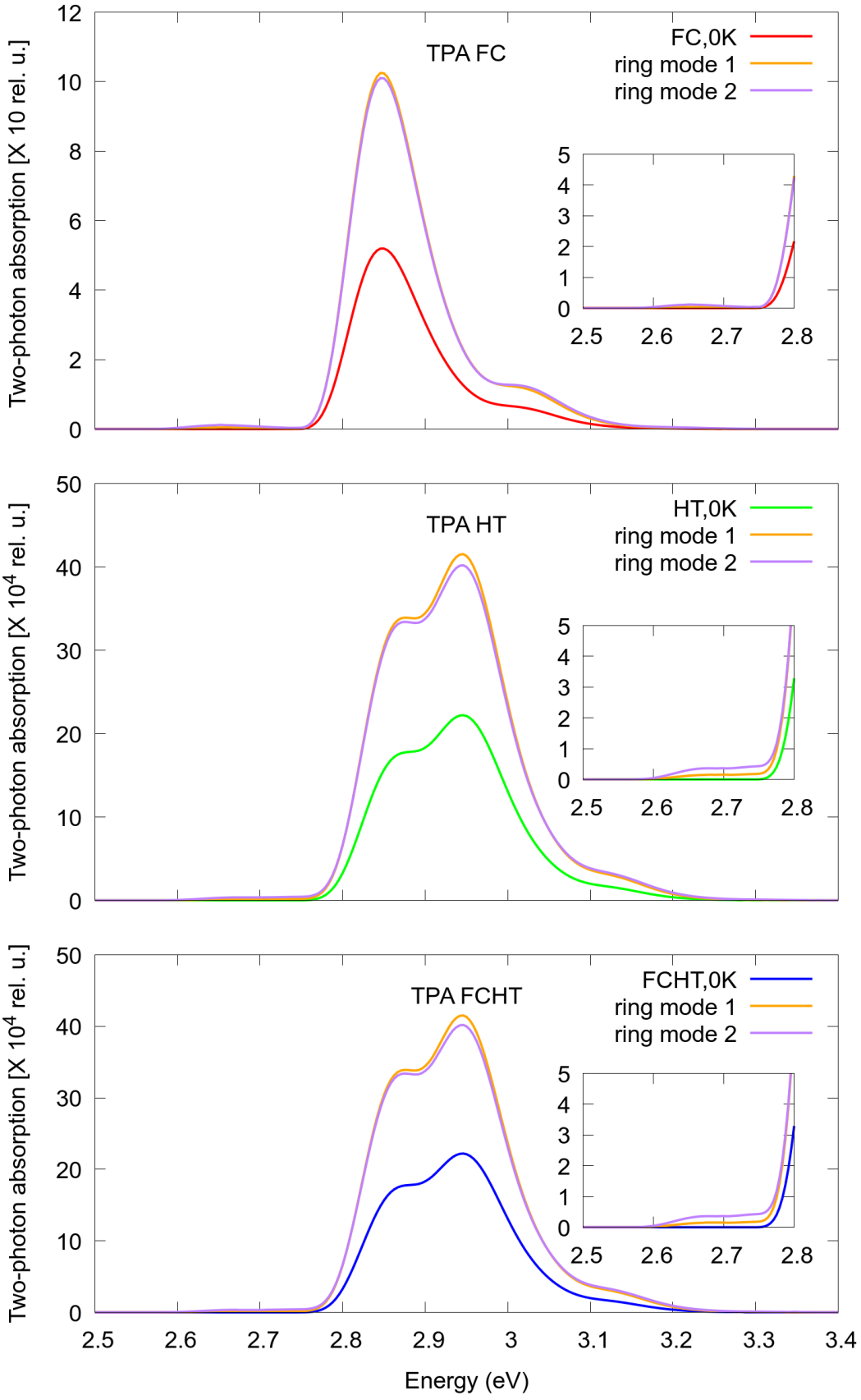

Figure 26: Computed TPA spectra of rhodamine in water with the TI method with FC (top), HT (middle) and total FCHT (bottom) effects at the CAM-B3LYP/6-31G* level with vibrational pre-excitation of ring modes (orange and purple).

3.10 DISCUSSION

The trends observed in the computed vibrationally resolved electronic absorption spectra are consistent for both OPA and TPA within FC approximation. Given that the results are also consistent with the available published work especially in the case of rhodamine, the implementation for the calculation of vibrationally resolved electronic absorption spectra including the first-order HT effects is found to be reliable. The role of non-Condon effects is found to be the absolute factor determining the TPA behaviour of the rhodamine [96, 97, 138].

Both the systems that were investigated showed a bright $\pi - \pi^*$-transition in an aromatic π-system (figs. 14 and 21). While in the case of DMA-NDBF, the NO_2 bend yields the strongest VIPER effect, the rhodamine has no vibrational modes showing any significant VIPER effect. Only the ring distortion modes could be probed based on the measure of their dimensionless displacements. The analysis leads to the conclusion that the strength of the VIPER effect depends on the structural changes that occur within the molecule upon electronic excitation. Further inferences can be drawn based on the availability of the experimental findings. The ring distortion mode of DMA-NDBF exhibits comparatively lower VIPER activity. In all the cases, it can be seen that the structural features within the molecular region are influenced mostly by the localized electronic transition. The main takeaway from this investigation should be that the measure of dimensionless displacements is the best indication of the strength of the VIPER activity of the vibrational modes.

4

EXCITATION ENERGY TRANSFER

A certain species gets excited and transfers energy to another species. This transfer of excitation energy phenomenon from a donor species D to the acceptor species A is characterized by the following equation:

$$D^* + A \rightarrow D + A^* \tag{115}$$

The processes of deactivation of D followed by excitation of A happens simultaneously or successively. The transfer mechanism mainly depends on the type of interaction between D and A [129].

Radiative Energy Transfer

Photons are emitted by the donor and then in turn absorbed by the acceptor.

$$D^* \rightarrow D + h\nu_D \tag{116}$$

$$A + h\nu_D \rightarrow A^* \tag{117}$$

Here, the donor acts as a "molecular lamp" capable of irradiating light into its environment. A net transfer of energy occurs between D and A when the emitted photons are absorbed by A. Radiative energy transfer occurs in the "far field" i.e., the average D-A distance is larger than the wavelength. Following criteria need to be met for this phenomenon to occur:

- D has a strong fluorescence quantum yield,
- A possesses a strong absorption coefficient in the emission region of D,
- Significant encounter between the photons emitted by D and the number of A molecules.

Radiationless energy transfer

The phenomenon of radiationless energy transfer takes place in the "near-field", i.e., at distances between D and A much shorter than the wavelength of the corresponding photon ($<$ 10 nm) [50]. In other terms, short-range interactions between the two species lead to the radiationless energy transfer.

Based on the interaction mechanism, interactions may be classified as Coulombic and/or due to intermolecular orbital overlap. In Coulombic interactions, there

could be long-range dipole-dipole interactions and short-range multi-polar interactions. The intermolecular orbital overlap led interactions are obviously short-range as these include electron exchange (described by Dexter's mechanism [34]) and charge resonance interactions.

The weak-coupling regime is now the core area of interest where perturbation theory can be applied to investigate the energy transfer. This approach was contributed by Forster [46] in 1946.

4.1 FÖRSTER THEORY FOR DONOR-ACCEPTOR PAIRS

For better understanding, consider a donor-acceptor (D-A) pair separated by a distance r_{DA}.

$$D^* + A \rightarrow D + A^* \tag{118}$$

In the weak-coupling limit, the rate of the radiationaless energy transfer between D and A can be expressed through the Fermi golden rule [36, 43]

$$\begin{aligned} k_{EET} &= \frac{1}{\hbar^2} |\langle \varphi_{D^*}(1)\varphi_A(2)|H|\varphi_D(1)\varphi_{A^*}(2)\rangle|^2 \\ &= \frac{1}{\hbar^2} V^2 \delta(\nu_D - \nu_A) \end{aligned} \tag{119}$$

where $\varphi_{D^*}(1)\varphi_A(2)$ represents the initial wavefunction of the coupled system (electrons are denoted by 1 and 2), $\varphi_D(1)\varphi_{A^*}(2)$ the final state and $\delta(\nu_D - \nu_A)$ the energy conservation term. Only if the deexcitation of D is isoenergetic with the excitation of A, the transition between the two states can take place. The transition between the states corresponds to the excitation energy transfer between D and A.

The Hamiltonian of the electrostatic interaction reads

$$\hat{H} = \frac{1}{4\pi\varepsilon_0 n^2} \frac{e^2}{r_{DA}} \tag{120}$$

where n is the refractive index of the medium. The matrix element V which represents the interaction between two transition charge densities of D and A respectively can be written as

$$V = \frac{e^2}{4\pi\varepsilon_0 n^2} \langle \varphi_{D^*}(1)\varphi_A(2)| \frac{1}{r_{DA}} |\varphi_D(1)\varphi_{A^*}(2)\rangle \tag{121}$$

At large D-A separation distances, the dipole-dipole approximation describes V quite well.

$$V = \frac{1}{4\pi\varepsilon_0 n^2} \frac{\vec{\mu}_D \cdot \vec{\mu}_A - 3\left(\vec{\mu}_D \cdot \hat{R}_{DA}\right)\left(\vec{\mu}_A \cdot \hat{R}_{DA}\right)}{R_{DA}^3} \tag{122}$$

where $\vec{\mu}_D$ and $\vec{\mu}_A$ are the transition dipole moment vectors of D and A respectively, R_{DA} is the distance between the two dipoles and $\hat{R}_{DA}$ the unit vector pointing to the direction between them. Fig. 27 depicts the visualization of the angles defining

the relative orientations of the donor and acceptor transition moments. Looking at the representation, the matrix element can also be written as

$$\begin{aligned} V &= \frac{1}{4\pi\varepsilon_0 n^2}\frac{|\vec{\mu}_D||\vec{\mu}_A|}{R_{DA}^3}\left(\cos\Theta_T - 3\cos\Theta_D\cos\Theta_A\right) \\ &= \frac{1}{4\pi\varepsilon_0 n^2}\frac{|\vec{\mu}_D||\vec{\mu}_A|}{R_{DA}^3}\kappa \end{aligned} \tag{123}$$

κ is called the orientational factor, which only depends on the orientations of the dipoles with respect to each other and with respect to the vector connecting them [74].

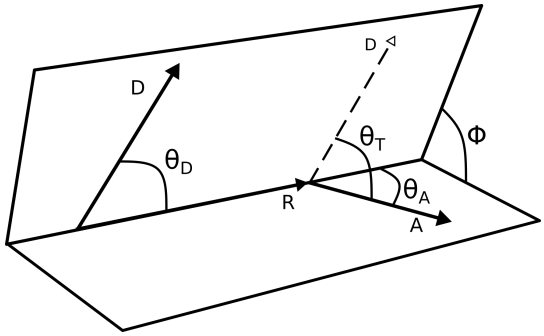

Figure 27: Visualization of the angles used to define the relative orientations of the donor and acceptor transition moments and the separation vector.

The rate of the radiationless energy transfer can then be calculated through:

$$k_{EET} = \frac{\kappa^2}{16\pi^2\varepsilon_0^2\hbar^2 n^4}\frac{|\vec{\mu}_D|^2|\vec{\mu}_A|^2}{R_{DA}^6}\delta(\nu_D - \nu_A) \tag{124}$$

4.1.1 *Dipole-dipole mechanism*

Eq. 124 implies that the rate of radiationaless energy transfer falls off as the inverse sixth power of $D-A$ separation, i.e., it is highly sensible to this parameter. To connect the transition dipole moments with the easily accessible spectral properties of D and A, a trick with delta functions can be exploited:

$$\delta(\nu_D - \nu_A) = \int \delta(\nu_D - \nu)\delta(\nu - \nu_A)d\nu \tag{125}$$

which leads to the rate equation

$$k_{EET} = \frac{1}{16\pi^2\varepsilon_0^2\hbar^2 n^4}\frac{\kappa^2}{R_{DA}^6}\int d\nu \left[|\vec{\mu}_D|^2\delta(\nu_D - \nu)\right]\left[|\vec{\mu_A}|^2\delta(\nu - \nu_A)\right] \tag{126}$$

Here, $|\vec{\mu}_D|^2\delta(\nu_D - \nu)$ and $|\vec{\mu}_A|^2\delta(\nu - \nu_A)$ are proportional to the emission spectrum of the donor and the absorption spectrum of the acceptor, respectively. The squared emission dipole moment is connected to the radiative decay rate (from the Fermi golden rule):

$$\frac{8\pi^2\nu^3|\vec{\mu}_D|^2}{3\varepsilon_0\hbar c^3} = k_r = \frac{\Phi_D}{\tau_D} \tag{127}$$

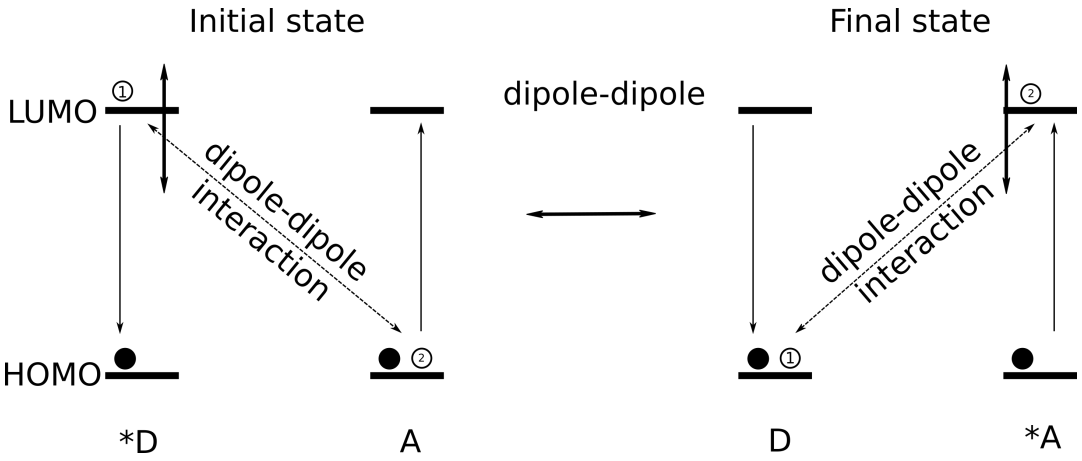

Figure 28: Excitation energy transfer through dipole-dipole mechanism. The vertical double-headed arrows represent the oscillating dipoles of D^* and A^*.

The radiative decay rate can be accessed by measuring the fluorescence lifetime (τ_D) and the fluorescence quantum yield (Φ).

Fig. 28 represents the dipole-dipole mechanism of energy transfer in a classical antenna. The flow of energy is between D and A where the distance of separation of the dipoles determines the efficiency of energy transfer [103]. The mechanism proceeds as follows: a creation of a coupled oscillating dipole field about A is triggered by the oscillating dipole field of D^* leading to the creation of A^*. When the oscillating dipole field of D^* has sufficient strength and is close enough to A to interact with it, a resonance condition for dipole-dipole energy transfer from D to A are met.

4.1.2 *Spectral overlap approach*

Time-dependent perturbation theory can be applied if the coupling between the molecules is sufficiently small [126]. Fermi's Golden rule then reads

$$\begin{aligned} \nu_{DA} =& \frac{2\pi}{\hbar} \sum_{m_D n_D} \sum_{m_A n_A} f^*_{D n_D} f_{A m_A} \\ & |\langle \Psi_{D m_D} \Psi^*_{A n_A} | \hat{V} | \Psi^*_{D n_D} | \Psi_{A m_A} \rangle|^2 \\ & \delta\left(E_{D m_D} - E^*_{D n_D} + E^*_{A n_A} - E_{A m_A}\right) \end{aligned} \tag{128}$$

where all vibrational quantum numbers of the neutral/ground state and the charged/excited state are designated by the tuples m and n, respectively. $f^*_{D n_D}$ and $f_{A m_A}$ are the distribution functions which account for the thermalized state manifold of the initial state with respect to the vibrational states for the vibrational equilibrium of the donor in the charged/excited state and the acceptor in the neutral/ground state, respectively.

On applying the Born-Oppenheimer [15] and the Condon [25–27] approximations, the coupling between the donor and acceptor becomes

$$\begin{aligned} \langle \Psi_{D m_D} \Psi^*_{A n_A} | \hat{V} | \Psi^*_{D n_D} \Psi_{A m_A} \rangle =& V_{DA} \langle \chi_{D m_D}\left(\vec{R}_D\right) | \chi^*_{D n_D}\left(\vec{R}_D\right) \rangle \\ & \langle \chi^*_{A n_A}\left(\vec{R}_A\right) | \chi_{A m_A}\left(\vec{R}_A\right) \rangle \end{aligned} \tag{129}$$

with the Coulomb matrix element

$$V_{DA} = \langle \psi_{D\vec{R}_D}(\vec{r}_D)\,\psi^*_{A\vec{R}_A} | \hat{V} | \psi^*_{D\vec{R}_D}(\vec{r}_D)\,\psi_{A\vec{R}_A}(\vec{r}_A) \rangle \tag{130}$$

where χ is the nuclear and ψ the electronic wave function with the nuclear coordinates $\vec{R}$ and the electronic coordinates $\vec{r}$.

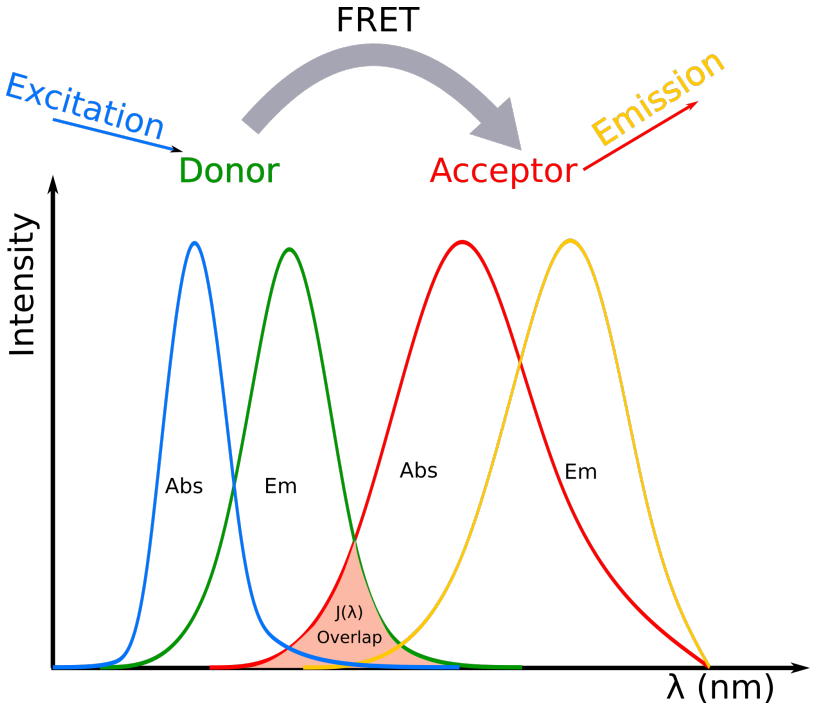

Figure 29: Spectral overlap illustration between the emission spectrum of the donor and the absorption spectrum of the acceptor.

An energy integral is introduced which can be divided into a donor and an acceptor part:

$$\delta\left(\left[E_{Dm_D} - E^*_{Dn_D}\right] + \left[E^*_{An_A} - E_{Am_A}\right]\right) = \int_{-\infty}^{\infty} dE\,\delta\left(E_{Dm_D} - E^*_{Dn_D} + E\right)\delta\left(E^*_{An_A} - E_{Am_A} - E\right) \tag{131}$$

Here E_D and E_A correspond to the energy terms with respect to the donor D and acceptor A groups. Through the definition of the auxiliary function

$$D_D(E) = \sum_{m_D n_D} f^*_{Dn_D} |\langle \chi_{Dm_D}\left(\vec{R}_D\right) | \chi^*_{Dn_D}\left(\vec{R}_D\right)\rangle|^2 \delta\left(E_{Dm_D} - E^*_{Dn_D} + E\right) \tag{132}$$

for the donor deexcitation/neutralization and the analogue equation for the acceptor/ionization respectively, the energy transfer rate, eq. 128 can be written as

$$\nu_{DA} = \frac{2\pi}{\hbar} V^2_{DA} \int_{-\infty}^{\infty} dE\, D_D(E) D_A(E) = \frac{2\pi}{\hbar} V^2_{DA} J_{DA} \tag{133}$$

with the *Franck-Condon weighted density of states* (FCWD) [25, 26, 48] which takes into account the vibrations of the molecules and contains the spectral overlap of the

densities of states D_D of the donor and the D_A of the acceptor. If there are external effects such as an external electric field or some other environmental effects, an energetic shift ΔE_{DA} can be included in $D_D(E)$ or $D_A(E)$.

$$\tilde{J} = \int dE\, D_D(E - E_{DA}) D_A(E) = \int dE\, D_D(E) D_A(E + E_{DA}) \tag{134}$$

4.2 TRANSITION DENSITY CUBES

The transition density cube (TDC) method developed by Krueger *et al.* [71] is a more reliable method than the dipole-dipole approximation to compute the Coulombic portion of the electronic coupling between two molecules. It utilizes the full three-dimensional details of the transition densities and therefore provides a highly accurate estimate allowed by the original quantum mechanical calculation. The trigger behind the development of this method was an experiment revealing the rapid timescales of electronic energy transfer between the pigment molecules involved in photosynthesis. It thus became necessary to understand the balance between several factors to model the results. The electronic coupling between the transition moments of the pigments was the main important factor.

As discussed in the earlier section, the Förster treatment [45] is based on the assumption that the total electronic coupling is dominated by the Coulombic coupling (eq. 122). There are several shortcomings with respect to the assumptions in the treatment.

1. Significant orbital overlap between the orbitals results in small errors indicating that the total coupling may not be well-represented by the Coulombic coupling. The TDC method calculates the Coulombic coupling and not the total coupling. Hence, orbital overlap effects must be considered separately [24].

2. The ideal dipole approximation (IDA) breaks down when R_{DA} is small i.e., roughly the same size or smaller than the molecules involved. This causes significant errors in many more cases because the molecular transition moments do not appear point-sized anymore. Also, the centers of the transition moments, from which R_{DA} is measured, become difficult to define.

Molecules with extended conjugation, e.g. carotenoids [72], or asymmetric transition densities exaggerate errors in the IDA, making it inappropriate for photosynthetic systems.

Therefore, a need arises for developing a practical method for accurate calculation of the Coulombic coupling between donor and acceptor transitions. In the TDC method, a quantum mechanical calculation is employed to determine wavefunctions for the initial and final states of the molecular transitions involved. The inverse product of these wavefunctions is the transition density

$$M_k(\mathbf{r}) = \int \Psi_{kg}(\vec{r}) \Psi^*_{ke}(\vec{r}) ds \tag{135}$$

where Ψ_{Ng} and Ψ_{Ne} denote the electronic ground and excited states of molecule N, respectively, and the integral is over only spin. The Coulombic interaction between

the donor and acceptor transition densities gives the exact Coulombic coupling (equivalent to retaining all terms in the multipole expansion).

$$V_{DA}^{Coul} = \frac{1}{4\pi\varepsilon_0} \int \frac{M_D(\vec{r}_i) M_A(\vec{r}_j)}{|\vec{r}_i - \vec{r}_j|} d\vec{r}_i d\vec{r}_j \tag{136}$$

Integrating the product of electronic ground and excited states into a three-dimensional grid of finite-sized volume elements makes up the cubes

$$M_N^{eq}(x,y,z) = V \int_z^{z+\delta z} \int_y^{y+\delta y} \int_x^{x+\delta x} \int_s \Psi_{Ng} \Psi_{Ne}^* ds dx dy dz \tag{137}$$

in which s represents the spin variables, the δ_α define the grid size of the density cubes, and V_δ is the element volume ($V_\delta = \delta_x \delta_y \delta_z$) needed as a practical means of converting charge density per unit volume into charge density per element. The set of finite-sized volume elements for a molecule is called the transition density cube. The elements are defined in terms of Cartesian coordinates in which the δ_x,δ_y and δ_z are non-divisible step sizes along the respective coordinate axes. Fig. 30 illustrates the transition densities of the donor and acceptor fragments.

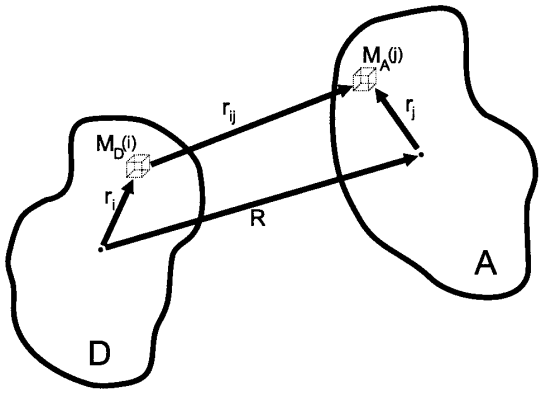

Figure 30: Depiction of two cells in the arbitrary donor D and acceptor A transition densities. The vectors $\mathbf{r}_i$ and $\mathbf{r}_j$ define the positions of TDC elements $M_D(i)$ and $M_A(j)$, relative to the centers of D and A, respectively. $\mathbf{R}$ is the center-to-center separation and $\mathbf{r}_{ij}$ is the separation between cells. Reprinted (adapted) with permission from [71]. Copyright 1998 American Chemical Society.

In the transition density formalism the Coulombic coupling is expressed by summing the Coulombic interactions between all the elements of each cube [92].

$$V_{DA}^{TDC} = \frac{1}{4\pi\varepsilon_0} \sum_{i,j} \frac{M_D(i) M_A(j)}{\vec{r}_{ij}} \tag{138}$$

where $M_D(i)$ and $M_A(j)$ are TDC elements i and j for the donor and acceptor and r_{ij} is their separation.

4.3 NONLINEAR CHROMOPHORES: RHODAMINES

Rhodamines are one of the most sought after molecules to modify as a two-photon dye, its applications being wide-ranging such as laser dyes, fluorescent probes,

sensitizers etc. Among the two-photon active systems, rhodamines are the most preferred choice as benchmark molecules. Structurally characterized as xanthene derivatives, rhodamines consist of a xanthene ring substituted by two amino groups and an *ortho*-carboxylphenyl at the 9-position carbon substituting the xanthene ring.

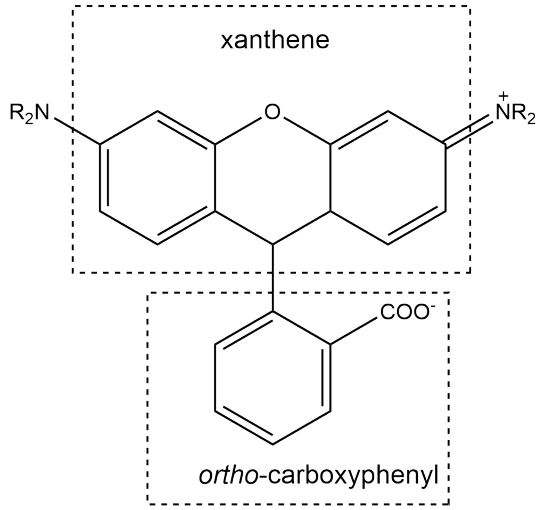

Figure 31: Core structure of rhodamine constituted of two main moieties: xanthene ring substituted by two amino groups and an *ortho*-carboxyphenyl at the 9-position carbon.

In solution, rhodamine can exist in two different forms, a lactone or zwitterionic one depending on the polarity of the solvent. The lactone form can exist in both protic as well as aprotic solvents whereas the zwitterionic form only exists in protic solvents. Depending on the solvent polarity and the hydrogen bond interactions, the equilibrium between lactone and zwitterion form varies as illustrated in fig. 32.

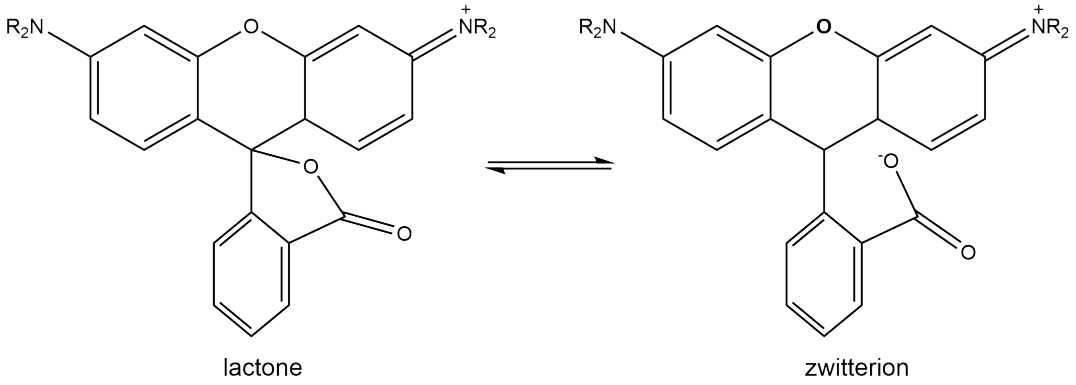

Figure 32: Representation of equilibrium between lactone and zwitterion structures of rhodamines.

Design and development of new rhodamines continues to be of interest in order to achieve better photochemical and photophysical properties for example, absorption maxima at longer wavelengths, higher quantum yields and tolerance to photobleaching. Here, the extent of TPA is the main objective for which the following modifications of rhodamines have been investigated for their TPA properties.

The wavelengths of electronic absorption have been measured by the spectroscopic collaborators and the rhodamines show variation in absorption maximum with respect to the amino substituents. Fig. 33 depicts the labelled rhodamines investigated theoretically in collaboration with the partners from synthesis and spectroscopy.

Barring the methylcarboxylate substituent at the *ortho*-carboxyphenyl ring, it is identifiable that the parent structures of Rho2, Rho3 and Rho4 resemble that of rhodamine B (Rho B), rhodamine 6G (Rho 6G) and rhodamine 101 (Rh 101), respectively. The structure of Rho1 basically derives from that of rhodamine 110 (Rh 110). However, the Rho 110 structure contains simple amine substituents instead of the methylamine ones. The experimentally measured wavelength of the absorption maximum λ_{abs} are: Rho1 = 542 nm, Rho2 = 549 nm, Rho3 = 519 nm and Rho4 = 572 nm.

4.4 COMPUTATIONAL PROCEDURE

All electronic structure calculations were performed with the *Gaussian16* series of programs, revision *B.01* [49] unless noted otherwise. Ground state calculations including geometry optimization and frequency analysis were performed using DFT while its time-dependent extension TDDFT was employed for the calculation of excited states. In ground state calculations, computation of equilibrium structures and vibrational frequencies is enabled by the availability of analytic first and second derivatives. The vibrational frequencies for the excited state could be computed by numerical differentiation of analytic gradients along atomic Cartesian coordinates due to the availability of only analytic first derivatives. PCM was employed with methanol as the solvent in accordance with its usage in the experiments. Solvent effects were accounted for as the analytic gradients for the ground as well as the excited states [119] are available with the employment of PCM [132]. Fine integration grids (`int=ultrafine`) were used and the tight optimzation criteria were assigned for geometry optimizations in all electronic structure calculations.

Quadratic response calculations in order to know the TPA cross-sections for the excited electronic states were performed using the 2018 version of DALTON package [2]. The reference structure for these calculations was the optimized ground state geometry from the *Gaussian16* calculations.

For computation of the spectra, the PES of the excited state was modeled using the VG approach [44], where it is expanded around the equilibrium geometry of the ground state and approximated by a mere shift in the ground state PES. The VG method is preferred here as the excited state is found to be displaced from the ground state minimum making the adiabatic approach unreliable. The time-independent (TI) and analytic time-dependent (TD) spectra were computed with a development version of the *FCclasses* code [111]. The resulting spectra were convoluted with a Gaussian lineshape with a Half Width at Half Maximum (HWHM) of 0.01 eV, unless noted otherwise. The TI spectra calculations were done with $N_{max} = 10^8$ FC integrals per class and a maximum quantum number for classes C_1 and C_2 of $w_{max}^{(C_1)} = 30$ and $w_{max}^{(C_2)} = 25$, respectively.

For the calculation of Coulombic coupling through the TDC approach, transition density cubes (TDCs) are generated using the Q-Chem [120] electronic structure package. This involves excited states calculation with the TDDFT. A stand-alone

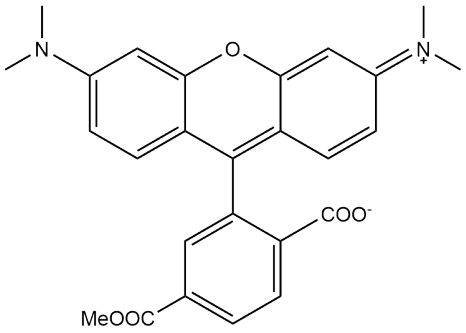

Rho1

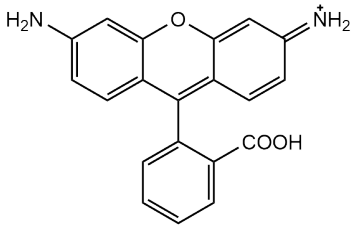

Rho110

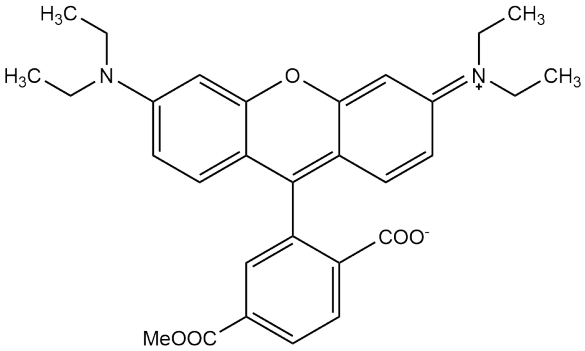

Rho2

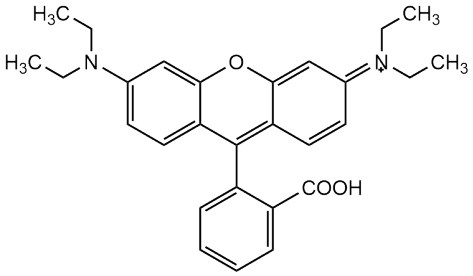

RhoB

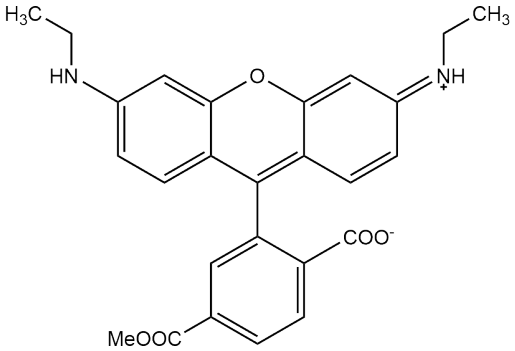

Rho3

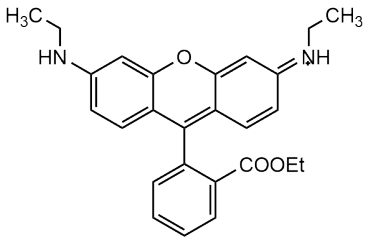

Rho6G

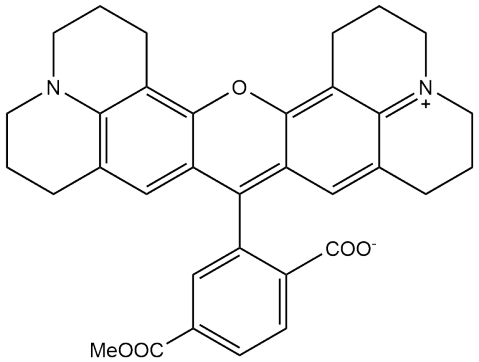

Rho4

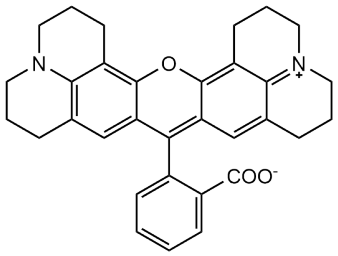

Rho101

Figure 33: Structures of the rhodamine derivatives under investigation for TPA properties.

code developed by Jan von Cosel reads the cube elements of the states involving transitions within the donor and acceptor fragments respectively and then computes the Coulombic coupling V_{DA}^{TDC} needed further for the calculation of the rate of energy transfer. This code has been tested for the reported calculations of the exciton coupling elements between the DNA bases by Czader *et al.* [32]. The results obtained are plausible but do not agree well with the published results.

4.5 RESULTS FOR RHODAMINES

In this section, the results of the electronic structure calculations and subsequently the quadratic response simulations of rhodamines are described. The TPA cross-sections through the means of quadratic response calculations will be discussed and then compared with the experimental two-photon excitation fluorescence (TPEF) measurements. The objective is to determine the most suitable sensitized two-photon system among the given set of rhodamines shown in fig. 33.

4.5.1 *Electronic structure calculations*

The ground state geometries of the given rhodamines were fully optimized with tight optimization criteria and using fine integration grids employing DFT method with a hybrid B3LYP functional based on GGA and 6-31G* basis set. The solvent effects of methanol were modeled solely with the PCM solvation model. Frequency analysis was performed to confirm correspondence of the optimized ground state geometry to a real minimum without negative frequency.

At this optimized geometry with the methodology mentioned above, the vertical excitation energies were calculated using linear-response TDDFT with B3LYP as well as the long-range corrected CAM-B3LYP and a "half-and-half" functional BHandHLYP. The purpose behind this procedure is to avoid the formation of the lactone structures as illustrated in Section 4.3. Using the same optimized ground state geometry, the quadratic response calculations to calculate TPA cross-sections were performed with the same B3LYP, CAM-B3LYP and BHandHLYP functionals. A proper benchmark is obtained which leads to the selection of a suitable functional for further calculations on intramolecular energy transfer within a molecular dyad.

4.5.2 *Electronic excitations and quadratic response*

Rho 1

Fig. 34 depicts the orbitals in the first two electronic states of Rho 1. The lowest excited singlet state, S_1, of Rho 1 corresponds to a $\pi - \pi^*$ - transition within the conjugated π- system from the HOMO to the LUMO and possesses a high oscillator strength. Both frontier orbitals are delocalized over the entire π- system, where the LUMO has a slightly lower contribution at the dimethyl amino substiuent groups.

The second singlet excited state, S_2, of Rho 1 involves a mix of a localized orbital transition within the conjugated π-system and charge transfer to the *ortho*-carboxyphenyl ring from the HOMO - 1 to the LUMO. The frontier orbitals of

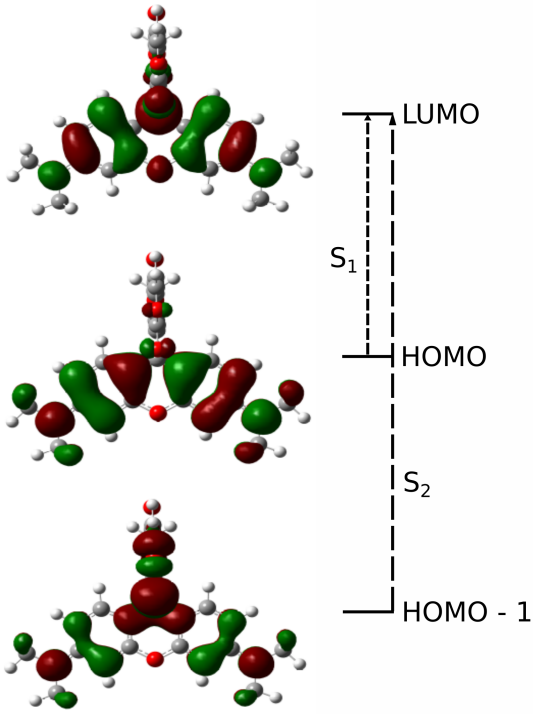

Figure 34: Frontier molecular orbitals in the first two electronic states of Rho1 obtained at CAM-B3LYP/6-31G* level in methanol.

HOMO - 1 are not as much delocalized within the π-system and rather has more contributions from the *o*-carboxyphenyl ring. The quadratic response calculations show that the S_2 state is the two-photon active state as reflected from its high TPA cross-section.

The experimentally observed absorption maximum of 542 nm in methanol corresponds to an excitation energy of 2.28 *eV*. Table 8 enlists the vertical excitation energies along with the oscillator strengths, f and TPA cross-sections, σ_{TP} in Göppert-Mayer (GM) units for the first two states obtained with different functionals.

Table 8: Electronic excitation energies, oscillator strengths f and TPA cross-sections σ_{TP} of the first two electronic states at the ground state equilibrium geometry of Rho 1 computed with different functionals with 6-31G* basis set in methanol.

DFT functional	State	Energy (*eV*)	f	σ_{TP} (GM)
B3LYP	S_1	2.75	0.75	17.7
	S_2	2.89	0.08	29
BHandHLYP	S_1	3.14	1.03	26.2
	S_2	3.89	0.29	295
CAM-B3LYP	S_1	3.04	0.97	25.1
	S_2	3.56	0.30	126

The dark S_2 state has a higher TPA cross-section than the bright S_1 state. It appears that S_1 is both one- and two-photon allowed due to its high oscillator

strength. The S_2 on the other hand is a one-photon forbidden and two-photon allowed state.

Rho 2

The orbital transitions in the first two electronic states are depicted in the fig. 35. S_1, the lowest excited state of Rho 2 exhibits a $\pi - \pi^*$- transition from the HOMO to the LUMO as seen also in the case of Rho 1. The LUMO similarly has the lower contribution at the diethyl amino substituent groups while both the frontier orbitals are delocalized over the entire π-system.

The low oscillator strength indicates that S_2 is a dark state. As seen in Rho 1, there is again a mixture of a localized orbital transition within the conjugated π-system and charge transfer to the *o*-carboxyphenyl ring represented by HOMO - 1 $\rightarrow$ LUMO transition. HOMO - 1 consists of more contributions from the *o*-carboxyphenyl ring and hence it is seen that the frontier orbitals are not as much delocalized over the π-system and has more contributions from the *o*-carboxyphenyl ring. It has a higher TPA cross-section than that of S_1 state indicated by the quadratic response calculations.

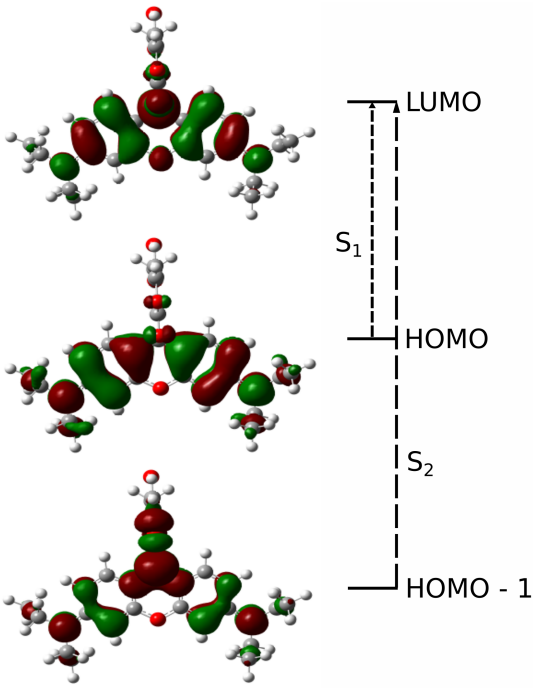

Figure 35: Frontier molecular orbitals in the first two electronic states of Rho2 obtained at CAM-B3LYP/6-31G* level in methanol.

Here, the experimentally observed absorption maximum of 549 nm in methanol corresponds to an excitation energy of 2.25 eV. The benchmark with different functionals of the vertical excitation energies together with their oscillator strengths f and TPA cross-sections σ_{TP} in GM units are enlisted in table 9.

The oscillator strengths and the TPA cross-sections imply that the S_1 state seems to be both one- and two-photon allowed whereas the S_2 is one-photon forbidden indicated by its low oscillator strength but two-photon allowed.

Table 9: Electronic excitation energies, oscillator strengths f and TPA cross-sections σ_{TP} of the first two electronic states at the ground state equilibrium geometry of Rho 2 computed with different functionals with 6-31G* basis set in methanol.

DFT functional	State	Energy (eV)	f	σ_{TP} (GM)
B3LYP	S_1	2.72	0.82	20.0
	S_2	2.85	0.08	32.9
BHandHLYP	S_1	3.10	1.11	29.0
	S_2	3.88	0.28	354
CAM-B3LYP	S_1	3.00	1.04	27.7
	S_2	3.53	0.30	150

Rho 3

As seen in the cases of Rho 1 and Rho 2, Rho 3 also exhibits similar orbital pictures for the first two electronic states. The lowest excited state, S_1 is a bright state consisting of a $\pi - \pi^*$- transition from the HOMO to the LUMO within the conjugated π-system. Both the frontier orbitals are delocalized over the entire π-system, however, the LUMO has the lower contribution at the amino substituent groups.

The next lowest excited state, S_2 is a dark state as indicated by its low oscillator strength. The HOMO - 1 to the LUMO transition in this state is a mixture of localized orbital transition within the conjugated π-system and charge transfer to the *ortho*-carboxyphenyl ring. HOMO - 1, in particular, does not show delocalization of frontier orbitals over the π-system and rather shows more contribution from the *ortho*-carboxyphenyl ring. In this case, only the TDDFT calculation with the CAM-B3LYP functional shows higher TPA cross-section than for the S_1 state. Otherwise, the two-photon activity of the S_2 state does not seem to be different from the S_1 state. Fig. 36 shows the orbitals involved in the first two electronic states of Rho 3.

The experimentally measured absorption maximum of 519 nm corresponds to an excitation energy of 2.38 eV. The following table 10 contains the vertical excitation energies, oscillator strengths f and TPA cross-sections σ_{TP} in GM units calculated with different functionals.

Table 10: Electronic excitation energies, oscillator strengths f and TPA cross-sections σ_{TP} of the first two electronic states at the ground state equilibrium geometry of Rho 3 computed with different functionals with 6-31G* basis set in methanol.

DFT functional	State	Energy (eV)	f	σ_{TP} (GM)
B3LYP	S_1	2.85	0.72	15.2
	S_2	2.88	0.08	17.2
BHandHLYP	S_1	3.21	1.01	22.9
	S_2	3.94	0.17	5.77
CAM-B3LYP	S_1	3.11	0.95	22.2
	S_2	3.57	0.27	57.3

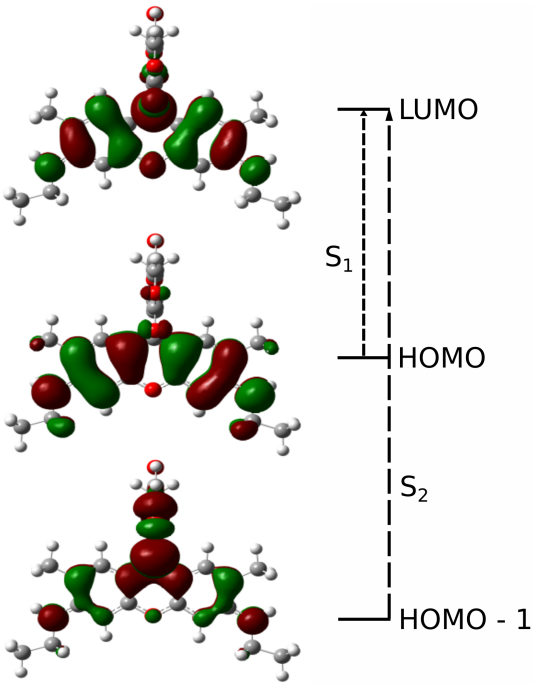

Figure 36: Frontier molecular orbitals in the first two electronic states of Rho3 obtained at CAM-B3LYP/6-31G* level in methanol.

As seen in the cases before, the S_1 state seems to be both one-and two-photon allowed whereas S_2 is one-photon forbidden and two-photon allowed indicated by the magnitudes of the oscillator strengths and TPA cross-sections.

Rho 4

Fig. 37 depicts the orbitals involved in the first two electronic states of Rho 4. It now becomes clear that the types of orbitals involved in the first two electronic states of interest in the given moeities of rhodamines is the same. So in Rho 4 also, the bright S_1 state consists of a $\pi - \pi^*$-transition within the conjugated π-system from the HOMO to the LUMO. Both the frontier orbitals are delocalized over the entire π-system. The LUMO has a lower contribution at the amino substituent groups.

The S_2 state, as expected is a dark state with low oscillator strength. In HOMO - 1, the frontier orbitals are not delocalized over the π-system and rather there are orbital contributions from the *o*-carboxyphenyl ring. Hence, the HOMO - 1 $\rightarrow$ LUMO transitions of the S_2 state of the rhodamines involve a mixture of localized orbital transition within the conjugated π-system and charge transfer to the *o*-carboxyphenyl ring. The quadratic response calculations show a significantly higher TPA cross-section of the S_2 state compared to the S_1 state.

The experimentally measured absorption maximum of 572 nm in methanol corresponds to an excitation energy of 2.16 eV. Table 11 enlists the benchmark of the vertical excitation energies, oscillator strength f and the TPA cross-section σ_{TP} in GM units for different DFT functionals.

The oscillator strengths and the TPA cross-sections lead to the inference that the S_1 state is both one- and two-photon allowed whereas the S_2 state is one-photon

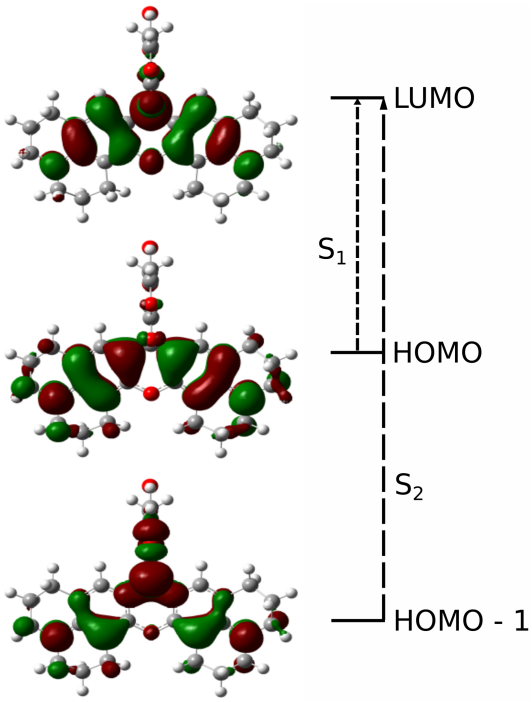

Figure 37: Frontier molecular orbitals in the first two electronic states of Rho4 obtained at CAM-B3LYP/6-31G* level in methanol.

Table 11: Electronic excitation energies, oscillator strengths f and TPA cross-sections σ_{TP} of the first two electronic states at the ground state equilibrium geometry of Rho 4 computed with different functionals with 6-31G* basis set.

DFT functional	State	Energy (eV)	f	σ_{TP} (GM)
B3LYP	S_1	2.61	0.84	15.7
	S_2	2.79	0.10	44.2
BHandHLYP	S_1	2.95	1.09	24.9
	S_2	3.66	0.00	148
CAM-B3LYP	S_1	2.85	1.03	23.6
	S_2	3.48	0.20	194

forbidden and two-photon allowed. In the following section involving a brief description of the TPEF measurements, a comparison is made with the above theoretical investigations.

4.5.3 *TPEF measurements of rhodamines*

Spectroscopic characterization of the four rhodamines was carried out with the fluorescence measurements with OPA followed by TPEF experiments. Fig. 38 shows the plots obtained in the fluorescence measurements. The left panel represents the fluorescence experiment with OPA. An estimate of wavelengths of the absorption for the first three electronic states is attempted. While the transition for the $S_0 \rightarrow S_1$

could be clearly observed, the detection of $S_0 \rightarrow S_2$ transition seems very difficult. The band of absorption following that is assumed to be for the $S_0 \rightarrow S_3$ transition.

The right panel of fig. 38 represents the TPEF measurements performed in the phototherapeutic window of 800-870 nm. The reference compund for the same has been the commonly available rhodamine 6G. As reported by Milojevich *et al*, the S_1 state is both one- and two-photon allowed whereas the S_2 state is one-photon forbidden but two-photon allowed. The same conclusion can be applied to the same measurements on the rhodamines. Since the right panel shows the TPA picture, the corresponding one-photon transition is expected to be in half the wavelength range of the TPEF spectrum. Based on this, the TPEF spectrum shows the TPA activity of the rhodamines in the S_2 state.

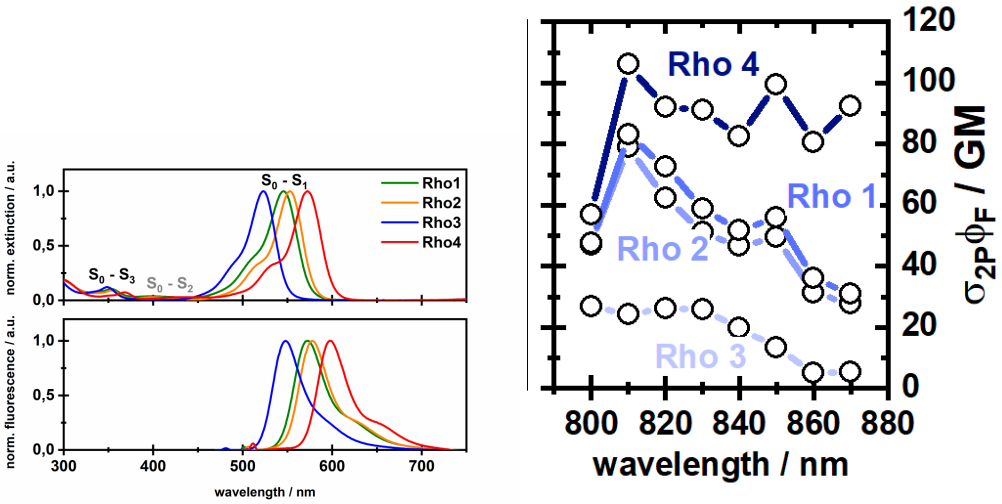

Figure 38: Left: OPA fluorescence measurements on the rhodamines. Right: TPEF values of the rhodamines in the phototherapeutic window of the range 800-870 nm.

The main inference from this collaborative experimental work is that Rho 4 exhibits the highest TPEF response while Rho 3 displays the least response in the TPEF results. This finding is supported by the electronic structure and quadratic response simulations reported earlier. Taking the values obtained with the CAM-B3LYP functional in particular, Rho 4 has the highest and Rho 3 has the least TPA cross-section. Hence, it is finally desirable to design and synthesize a molecular dyad with Rho 4 as the donor fragment.

4.6 BODIPY-BASED FLUOROPHORES

BODIPY is the commonly known short form of boron-dipyrromethenes. They are a very important class of organic fluorophores in which boron difluoride is attached to conjugated dipyrromethene. The first synthesis of BODIPY was reported by Treibs *et al.* in 1968 [133]. BODIPYs are used in a wide range of applications such as photodynamic therapy [5, 65], laser dyes [39, 81], fluorescent switches [53], electroluminescent films [73] etc. due to their excellent photophysical properties especially, their high quantum yields and extinction coefficients. Extensive efforts

have been invested in the design and synthesis of BODIPYs with desirable near IR absorptions and emissions [13, 117, 144]. The main objective considering the energy transfer in the larger picture is to impart significant changes on the absorption and emission wavelengths either by altering the size and number of rings in the core BODIPY system or substituting different functional groups.

As part of design and synthesis of BODIPY as the acceptor fragment in the molecular dyad [35], two derivatives of the BODIPY were synthesized. Fig. 39 shows the BODIPY with methyl substituents on both the sides of the core. For simplicity, this could be named as BODIPY 1. In the later stage of the organic synthesis, this BODIPY 1 has been successfully linked to Rho 1 (see fig. 33) through an acetylene bond.

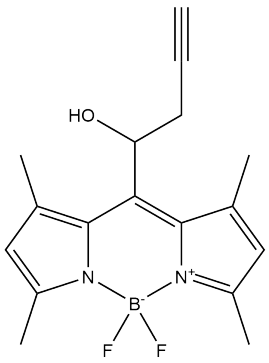

Figure 39: Structure of BODIPY 1 with the acetylene bond linker.

To achieve a red-shift in the absorption wavelength of the BODIPY, further substitutions have been made on one side of the core with anisole groups linked with a double bond. Fig. 40 shows the BODIPY substituted with anisole groups through double bonds. This could be named as BODIPY 2 for simplicity. BODIPY 2 has been successfully linked with Rho 4 (see fig. 33) through an acetylene bond in organic synthesis.

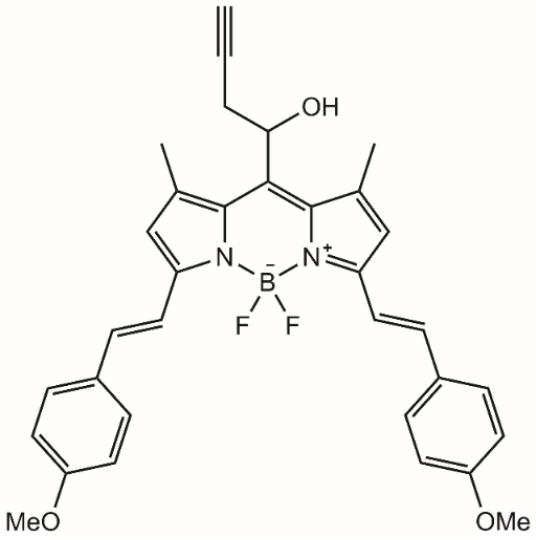

Figure 40: Molecular structure of BODIPY 2 substituted with conjugated groups to achieve a red-shift.

4.7 RESULTS FOR BODIPYS

4.7.1 *Electronic structure calculations*

The ground state geometries of the BODIPY structures were entirely optimized with tight optimization criteria using fine integration grids. A DFT method with the GGA based hybrid B3LYP functional along with 6-31G* basis set was employed for the optimization where the solvent effects of methanol were modeled solely with PCM solvation model. The correspondence of the optimized ground state geometry to a real minimum without negative frequency was confirmed with frequency analysis.

At the B3LYP/6-31G* optimized geometry, linear-response TDDFT was used to calculate vertical excitation energies with three DFT functionals: B3LYP, long-range corrected CAM-B3LYP and "half-and-half" BHandHLYP. At this same optimized ground state geometry, quadratic response calculations with the same B3LYP, CAM-B3LYP and BHandHLYP functionals were performed to calculate TPA cross-sections of the electronic states. A proper benchmark along the lines of the benchmark for rhodamines was obtained.

4.7.2 *Electronic excitations and quadratic response*

BODIPY 1

Fig. 41 depicts the orbitals in the first electronic state. The lowest excited singlet state, S_1, of BODIPY 1 corresponds to a $\pi - \pi^*$-transition within the conjugated π-system from the HOMO to the LUMO and has a significant oscillator strength. Both frontier orbitals are delocalized over the entire conjugated π-system, where the LUMO has a higher contribution at the side chain with the -OH functional group attached.

The experimentally observed absorption maximum of 511 nm corresponds to an excitation energy of 2.42 eV. The vertical excitation energy, oscillator strength and the TPA cross-section in GM units for the bright state, S_1 calculated with different functionals has been listed in table 12.

Table 12: Electronic excitation energies, oscillator strengths f and TPA cross-section σ_{TP} of the lowest excited singlet state of BODIPY 1 obtained at different functionals with 6-31G* basis set in methanol.

DFT functional	Energy (eV)	f	σ_{TP} (GM)
B3LYP	2.88	0.55	1.63
BHandHLYP	2.92	0.64	2.36
CAM-B3LYP	2.86	0.60	2.20

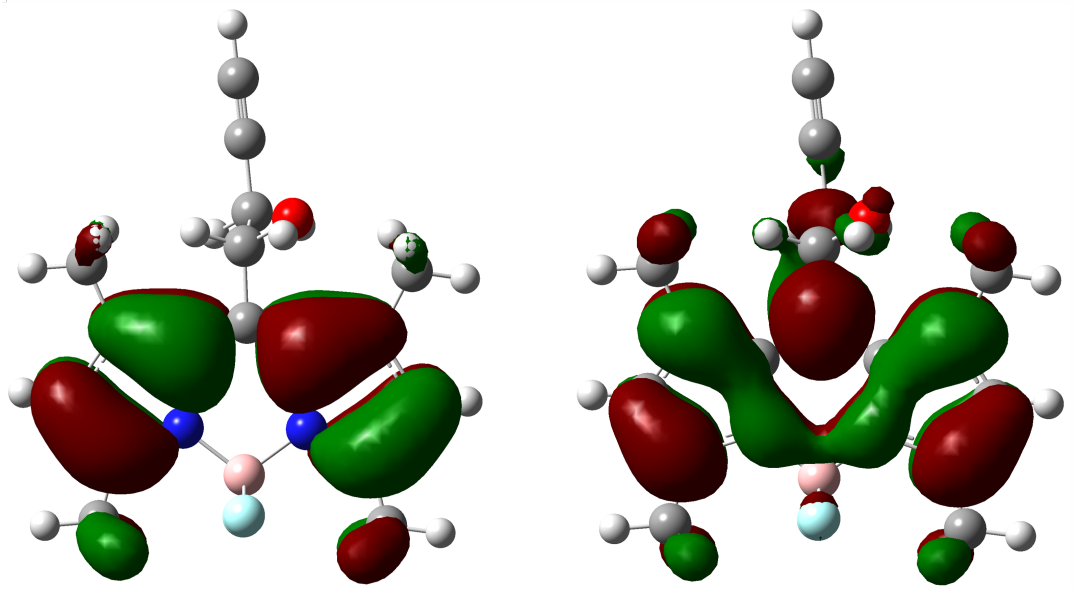

Figure 41: HOMO (left) and LUMO (right) of BODIPY obtained at the CAM-B3LYP/6-31G* level in methanol.

BODIPY 2

The lowest excited singlet state, S_1, of BODIPY 2 similarly shows a $\pi - \pi^*$-transition within the conjugated π-system from the HOMO to the LUMO. Umlike BODIPY 1, the S_1 state has a higher oscillator strength in BODIPY 2 overtly specifying it to be a bright state. Fig. 42 depicts the orbitals in the electronic state. Here it could be seen that both frontier orbitals are delocalized over the entire conjugated π-system, however, the LUMO has a much lower contribution at the phenyl substituents.

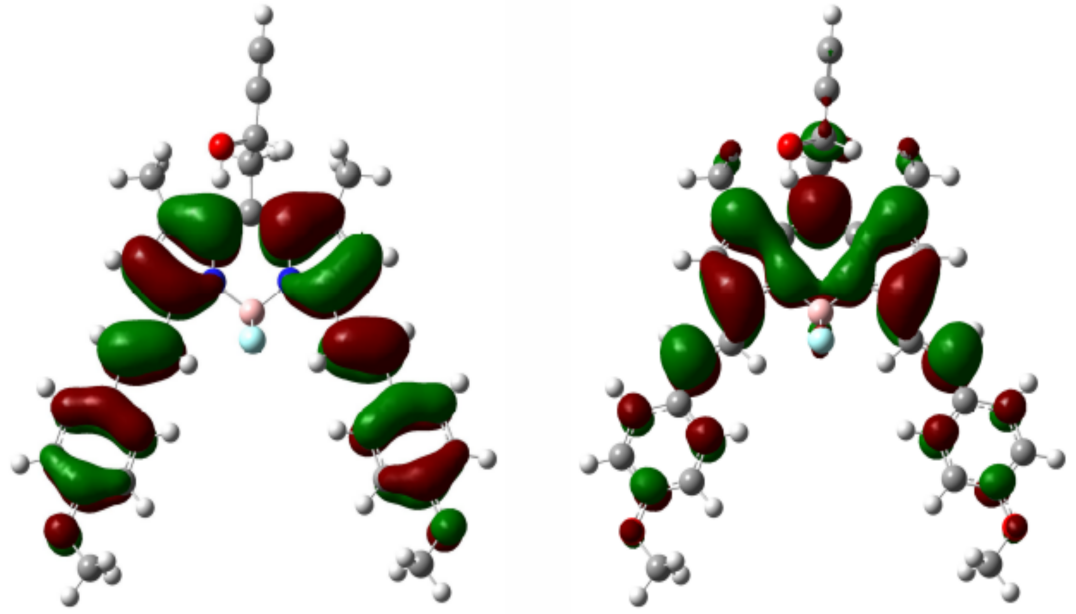

Figure 42: HOMO (left) and LUMO (right) of BODIPY substituted with conjugated groups obtained at the CAM-B3LYP/6-31G* level in methanol.

As an intended purpose of addition of the phenyl or rather specifically the anisole substituents, the experimentally measured absorption maximum of BODIPY 2 is at 649 nm which corresponds to an excitation energy of 1.91 eV. The following table 13 lists the vertical excitation energy, oscillator strength and the TPA cross-section in GM units for the bright S_1 state calculated with different functionals.

Table 13: Electronic excitation energies, oscillator strengths f and TPA cross-section σ_{TP} of the lowest excited singlet state of BODIPY 2 obtained at different functionals with 6-31G* basis set in methanol.

DFT functional	Energy (eV)	f	σ_{TP} (GM)
B3LYP	1.98	1.01	51.0
BHandHLYP	2.18	1.14	32.2
CAM-B3LYP	2.16	1.09	35.2

4.8 RHO1-BODIPY1 MOLECULAR DYAD

Fig. 43 depicts the molecular structure of the first synthesized molecular dyad where the Rho1 moiety has been linked together with the BODIPY1 through an acetylene bond. The systems in which multiple dyes are linked together as donor and acceptor groups are sometimes also referred to as cassette molecules[51]. They have wide range of applications as energy harvesters in photoelectronics and as fluorescent chemosensors in chemical biology. The design of a suitable linker to join the dyes together is fundamental challenges posed when it comes to synthesis. Based on the linker, there exists several possibilities of mechanisms of energy transfer. The expected mechanism in the following case is the "through-space" EET which is in accordance with the recognized principle of FRET. The other recently developed concept of through-bond energy transfer (TBET) is also now known which has its own specific advantages.

4.9 RESULTS FOR RHO1-BODIPY1 DYAD

4.9.1 *Electronic structure calculations*

The ground state geometry of the Rho1-BODIPY1 molecular dyad was optimized with tight optimization criteria using fine integration grids. The GGA based hybrid B3LYP functional of the DFT method was employed along with 6-31G* basis set for the optimization. PCM solvation model was invoked to model the solvent effects of methanol. The frequency analysis confirmed the correspondence of the ground state geometry to a real minimum without negative frequency.

At this ground state optimized geometry, the linear-response TD-DFT was employed to estimate the vertical excitation energies. Continuing the same methodologies followed in individual rhodamines and BODIPYs before, a proper benchmark could be made with the hybrid B3LYP, the long-range corrected CAM-B3LYP and the "half-and-half" functional BHandHLYP. The same is followed for the quadratic

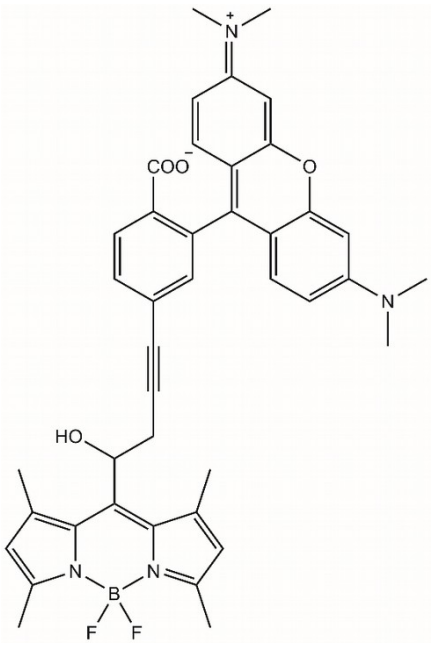

Figure 43: Molecular structure of Rho1-BODIPY1 molecular dyad.

response calculations to estimate the TPA cross-sections to attain a benchmark with the same set of DFT functionals.

4.9.1.1 *One-dimensional PES Scans*

Scans along certain dihedrals were performed in order to investigate selected points along the potential surface scans and manually check for local minima structures to be compared with the overall global minimum in order to have a thermodynamic estimate of the relevance of the conformers. This is another way to ensure complete correspondence of the optimized ground state equilibrium geometry to a minimum. The relevant dihedrals and the directions of one-dimensional PES scans have been highlighted in fig. 44.

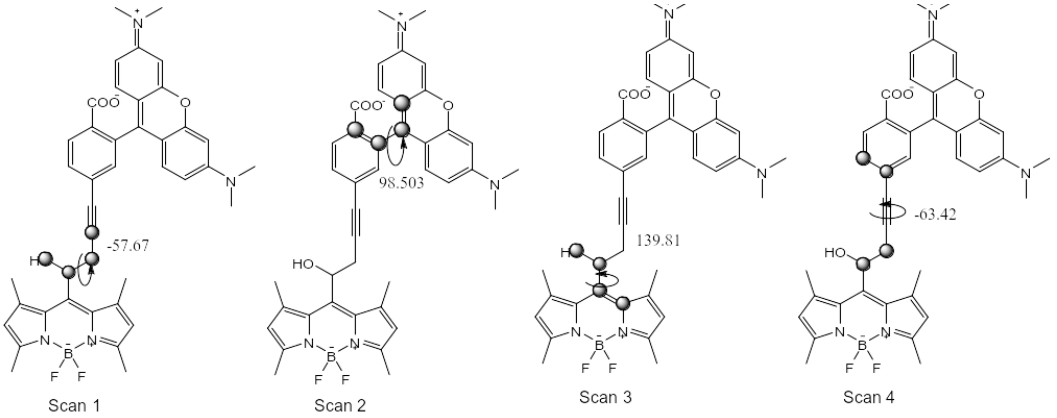

Figure 44: The dihedrals (highlighted by the bigger dots) and the direction of the 1D-PES scans. The angles of the dihedral in the ground state equilibrium geometry are mentioned.

The first 1D-PES scan is along the dihedral of -57.67° as indicated in Scan 1 in the left panel of fig. 44. After a rigid scan, the points along the scan coordinates having relative energies less than $25 kcal\,mol^{-1}$ are taken up for reoptimization. The reoptimization of these scan coordinates leads to the global minimum geometry with the dihedral of -57.67°.

The second 1D-PES scan is along the dihedral of 98.5° as indicated in Scan 2 in the left panel of fig. 44. The scan coordinates showing relative energies less than 25 $kcal\,mol^{-1}$ fall back to the global minima with the original dihedral of 98.5 ° upon reoptimization.

The third 1D-PES scan was performed from the global minima along the dihedral measuring 139.81° as indicated in Scan 3 in the right panel of fig. 44. The reoptimization of the scan coordinates having relative energies less than 25 $kcal\,mol^{-1}$ fall back to the global minima with the original dihedral of 139.81 °.

The final 1D-PES scan was performed along the dihedral consisting of the acetylene bond linker. The dihedral in the ground state equilibrium geometry is -63.42° as indicated in Scan 4 in the right panel of fig. 44. In this scan, all the scan coordinates have very low relative energies ($< 1 kcal\,mol^{-1}$). The reoptimization of all the scan coordinates resulted in several points of local minima. Subsequent analysis by TDDFT calculations shows no significant change or deviation in the vertical excitation energies from that of the geometry on the global minimum.

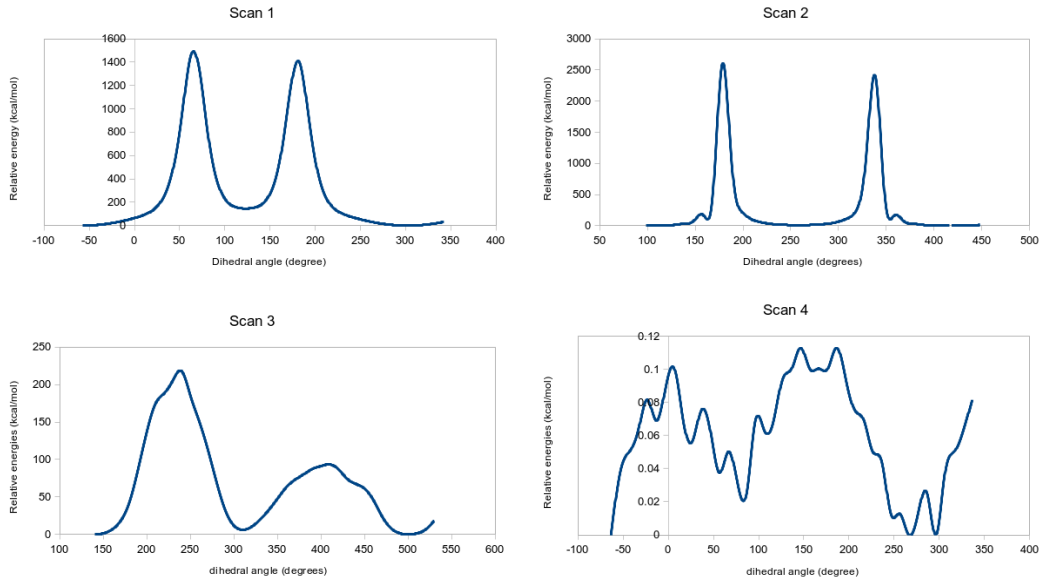

Figure 45: 1D-PES scans along the respective dihedrals obtained with B3LYP/6-31G* in methanol. The reference point is the global minimum or the ground state equilibrium structure.

Fig. 45 depicts the plots of the PES scans performed along the important dihedrals. All the scans point towards the confirmation of the optimized ground state equilibrium geometry to a global minimum.

4.9.2 *Electronic excitations and quadratic response*

The experimentally measured absorption spectrum of the isolated free rhodamine Rho1 and BODIPY1 as well as the Rho1-BODIPY1 dyad is depicted in fig. 46. The absorption maxima of Rho1 at 543 nm and that of BODIPY1 at 511 nm correspond to the vertical excitation energies of 2.28 eV for Rho1 and 2.42 eV for BODIPY1, respectively. The higher absorption energy of BODIPY1 than Rho1 makes the application of the dyad for intramolecular energy transfer undesirable.

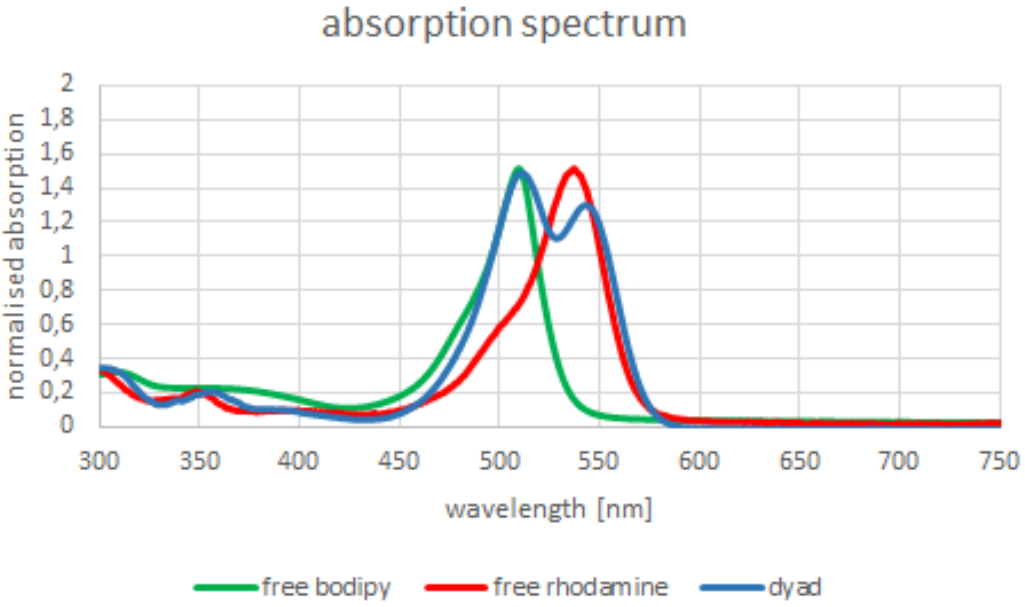

Figure 46: Experimental absorption spectra of Rho1-BODIPY1 dyad as well as that of the isolated free Rho1 and BODIPY1 moieties in methanol.

Electronic structure calculations involving the TDDFT analysis show two possible scenarios. One scenario represents the experimental observation where BODIPY1 has higher absorption energy than Rho1 when calculated with the hybrid B3LYP functional. The other analysis through TDDFT calculations with CAM-B3LYP functional represents the desirable scenario in which the excitation energy of Rho1 is higher than BODIPY1. Fig. 47 depicts the orbitals involved in the first three electronic states of Rho1-BODIPY1 dyad with B3LYP and CAM-B3LYP functionals. The molecular orbital picture is very important as this forms the basis in the process of calculating the rate of energy transfer. To supplement this, table 14 enlists the vertical excitation energies, oscillator strengths f along with the TPA cross-sections σ_{TP} in GM units.

The order and type of orbitals involved in the first three electronic states are the same from the calculations with both BHandHLYP and CAM-B3LYP. Fig. 47 depicts the orbitals involved in the transitions in the first three electronic states of Rho1-BODIPY1 dyad.

In case of calculations with B3LYP, the lowest singlet state S_1 consists of HOMO to LUMO charge transfer from the rhodamine to the BODIPY fragment. The second singlet excited state S_2 consists of the $\pi - \pi^*$ orbital transitions within the

Table 14: Electronic excitation energies, oscillator strengths f and TPA cross-section σ_{TP} of the first three electronic states at the ground state equilibrium geometry of Rho1-BODIPY1 computed with different functionals with 6-31G* basis set in methanol.

DFT functional	State	Energy (*eV*)	f	σ_{TP} (GM)
B3LYP	S_1	2.65	0.00	1.18
	S_2	2.76	0.72	20.2
	S_3	2.87	0.45	2.51
BHandHLYP	S_1	2.92	0.60	3.20
	S_2	3.16	1.02	28.8
	S_3	3.88	0.36	325
CAM-B3LYP	S_1	2.86	0.57	3.00
	S_2	3.06	0.96	27.5
	S_3	3.56	0.34	175

rhodamine fragment from HOMO to the LUMO + 1. The third singlet excited state S_3 has to do with a $\pi - \pi^*$ orbital transition from the HOMO - 1 to the LUMO within the BODIPY fragment. In agreement with the experimental absorption spectra, the BODIPY fragment undesirably has the higher excitation energy than the rhodamine fragment.

Considering the calculations with CAM-B3LYP presents a different picture of the excited states. The lowest singlet excited state S_1 consists of a $\pi - \pi^*$ orbital transition within the BODIPY fragment from the HOMO - 1 to the LUMO. The next higher singlet excited state S_2 consists of the $\pi - \pi^*$ orbital transition from the HOMO to the LUMO + 1 within the rhodamine fragment. The third lowest singlet excited state S_3 involves an orbital transition from the HOMO - 2 to the LUMO + 1 again within the rhodamine fragment with a mix of charge transfer to the *o*-carboxyphenyl ring.

Referring back to the earlier sections on rhodamines and BODIPYs, it can be seen that the lowest singlet excited states of the isolated Rho1 and BODIPY1 are reflected in the $\pi - \pi^*$ excitations in the Rho1-BODIPY1 molecular dyad, respectively. In other words, the HOMO $\rightarrow$ LUMO $\pi - \pi^*$ transition of the isolated Rho1 (S_1 state) is the HOMO $\rightarrow$ LUMO + 1 (S_2 state in B3LYP) or the HOMO $\rightarrow$ LUMO + 1 (S_2 state in CAM-B3LYP) $\pi - \pi^*$ transition in Rho1-BODIPY1 dyad. Similarly, the HOMO $\rightarrow$ LUMO $\pi - \pi^*$ transition of the isolated BODIPY1 (S_1 state) is the HOMO - 1 $\rightarrow$ LUMO (S_3 state in B3LYP) or the HOMO - 1 $\rightarrow$ LUMO (S_1 state in CAM-B3LYP) in the Rho1-BODIPY1 dyad.

The S_2 excited state of the isolated Rho1 which exhibits HOMO - 1 $\rightarrow$ LUMO transfer appears as the S_3 electronic state in the Rho1-BODIPY1 dyad in the CAM-B3LYP calculations. This state is also observed to be a two-photon active state owing to its high TPA cross-section. Based on the TDDFT analysis made with the CAM-B3LYP functional, an assumption can be made that if an energy transfer process is to be initiated through the means of two-photon excitation, the S_3 electronic state relating to the rhodamine will be first excited. This will be followed by an internal conversion to the S_2 state within the rhodamine fragment. Finally, the EET would

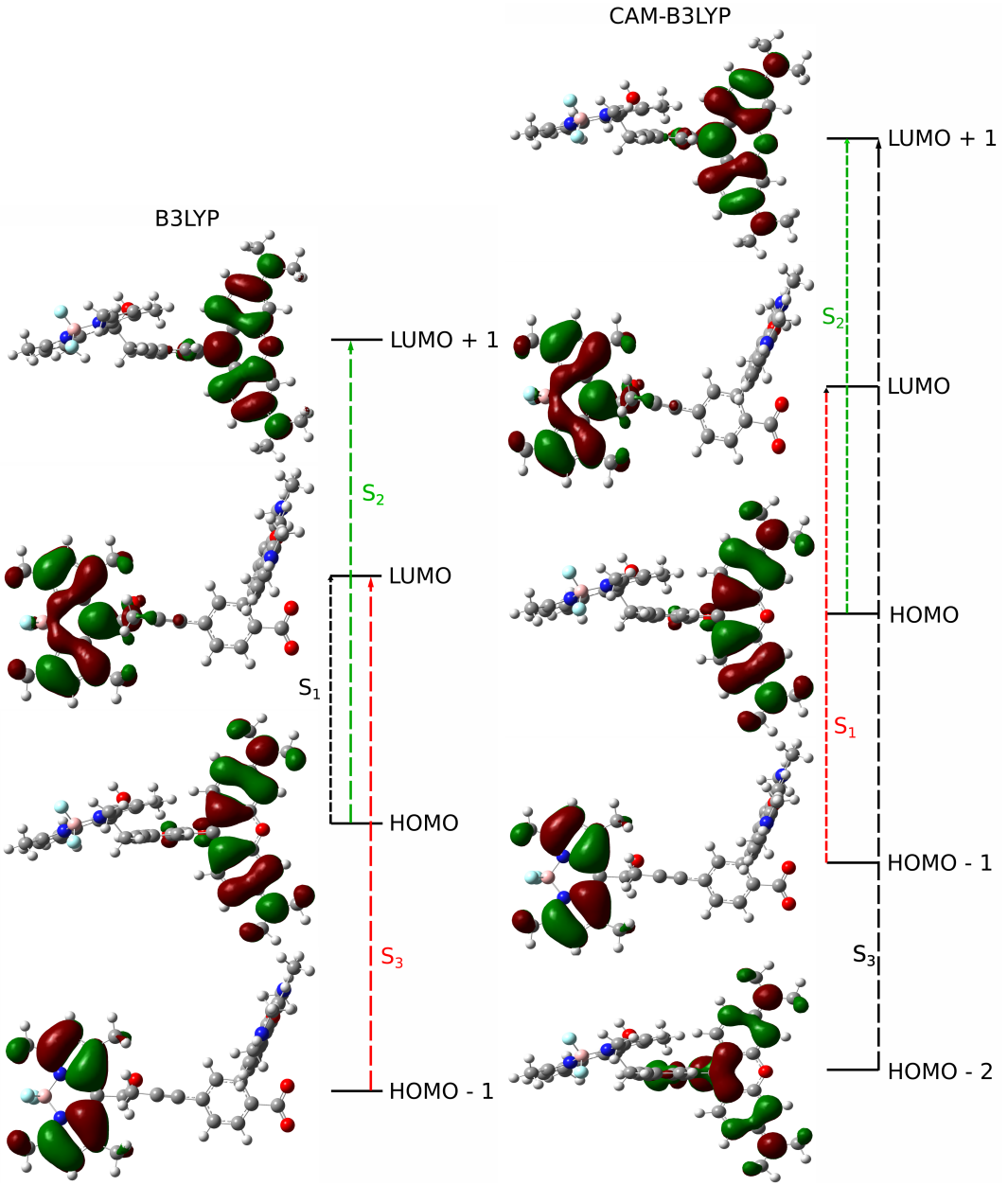

Figure 47: Frontier orbitals involved in the first three electronic states of Rho1-BODIPY1 dyad obtained at B3LYP/6-31G* (left) and CAM-B3LYP/6-31G* (right) in methanol. The orbital transitions within BODIPY1 fragment is highlighted in red and that within Rho1 fragment in green.

occur from the S_2 state to the S_1 state i.e., from the rhodamine to the BODIPY fragment. The following sections will describe the investigation of intramolecular energy transfer for both the scenarios.

4.9.3 *Spectral overlap*

Based on the molecular orbital picture above, the vibrationally resolved electronic absorption spectra of the respective electronic states involving $\pi - \pi^*$ orbital transitions within Rho1 and BODIPY1 fragments were computed with the analytical time-dependent (TD) method using the VG model. Fig. 48 shows the overlap between the computed vibronic emission and absorption spectra of Rho1 and BODIPY1 respectively. Specifically, the emission spectrum of Rho1 corresponds to the S_2 excited state and the absorption spectrum of BODIPY1 corresponds to the S_3 excited state. A significantly large overlap is observed from the calculations with B3LYP functional.

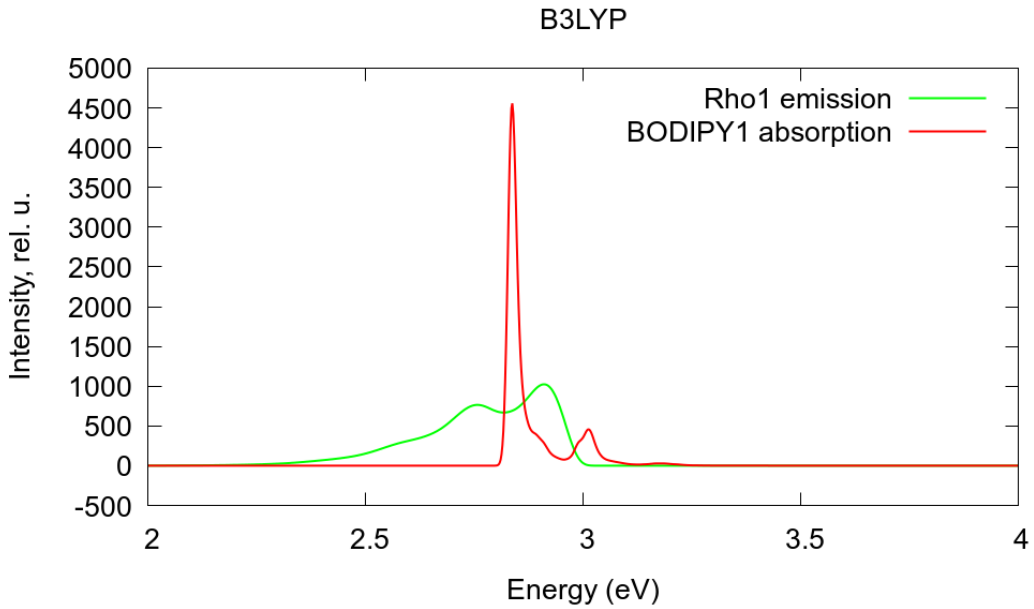

Figure 48: Overlap of the Rho1 emission and BODIPY1 absorption spectra obtained at the B3LYP/6-31G* level in methanol. Spectra computed with the TD analytical method.

The other scenario in which Rho1 has higher excitation energy than BODIPY1 is brought out through calculations with CAM-B3LYP functional. The overlap between the emission and absorption spectra of Rho1 and BODIPY1 respectively is depicted in fig. 49. In this scenario specifically, the emission spectra of Rho1 corresponds to the S_2 excited state and the absorption spectra of BODIPY1 corresponds to the S_1 excited state. Here too, the overlap between the emission and absorption is seen to be significantly large.

After normalization of the spectra, the overlap integrals calculated are tabulated in table 15.

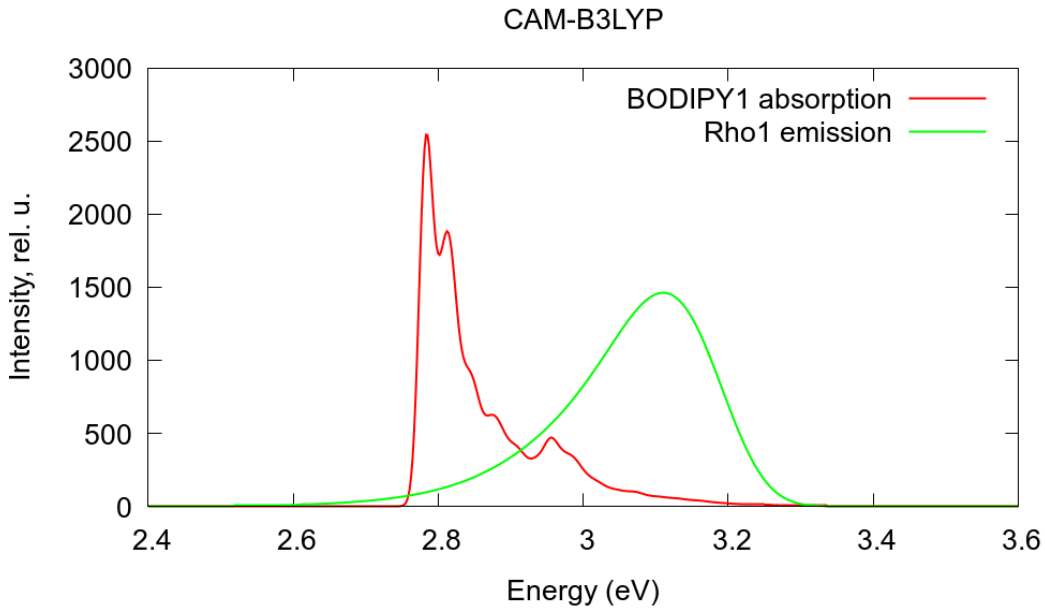

Figure 49: Overlap of the Rho1 emission and BODIPY1 absorption spectra obtained at the CAM-B3LYP/6-31G* level in methanol. Spectra computed with the TD analytical method.

Table 15: Overlap integral calculated with respect to the computed spectra obtained at 6-31G* basis in methanol with B3LYP and CAM-B3LYP functionals.

DFT functional	J_{DA}
B3LYP	2.1533
CAM-B3LYP	0.8417

4.9.4 *Dipole-dipole and Coulombic coupling*

The couplings were calculated through the dipole-dipole approximation using the Förster theory (ref. eq. 122) and the TDC method. The generation of TDCs requires a definition of 3D- mesh points. A $20 \times 20 \times 20$ mesh box is created which is centered at the molecular coordinate origin. The suitablility of the grid points is determined by checking for the convergence of the Coulombic coupling with respect to the number of grid points. The box length divided by the grid points gives out the grid spacing. Coulombic couplings were found to be consistent on checking for convergence from 80 to 130 grid points with the intervals of 10 grid points each time. The final couplings with respect to both dipole-dipole approximation and TDC method are listed in table 16.

Table 16: Calculated couplings with dipole-dipole approximation and TDC method at 6-31G* basis in methanol with B3LYP and CAM-B3LYP functionals.

DFT functional	$V_{DA}^{dip}(eV)$	$V_{DA}^{TDC}(eV)$
B3LYP	0.0091	0.0028
CAM-B3LYP	0.0103	0.0391

4.9.5 *Rate of intramolecular energy transfer*

Finally, with the required values of the overlap integral and the couplings available, the rate of EET is then calculated by the following equation.

$$k_{EET} = \frac{2\pi}{\hbar} V_{DA}^2 J_{DA} \tag{139}$$

The inverse of this EET rate gives out the timescale of energy transfer as expressed in the following equation.

$$\tau_{EET} = \frac{1}{k_{EET}} \tag{140}$$

Accordingly, the rates of intramolecular energy transfer can be calculated for the couplings obtained from the IDA and TDC methods as well as with the DFT functionals is listed in table 17. A benchmark or a comparison is obtained in this regard.

Table 17: Calculated rates and timescales of EET at 6-31G* basis in methanol with B3LYP and CAM-B3LYP functionals according to IDA and TDC method.

DFT functional	Theory	$k_{EET}(s^{-1})$	τ_{EET}
B3LYP	IDA	1.7021×10^{12}	585.56 fs
	TDC	1.6115×10^{11}	6.18 ps
CAM-B3LYP	IDA	8.5250×10^{11}	1.17 ps
	TDC	1.2284×10^{13}	81.4 fs

4.9.6 *Quantum dynamics*

Using ML-MCTDH method, quantum dynamical simulations on the Rho1-BODIPY1 dyad were performed as applied to a two-fragment based LVC Hamiltonian using 266 vibrational modes. For this separate electronic structure calculations were performed on the dyad briefly detailed as follows: Ground state geometry was optimized at CAM-B3LYP/6-31G* level of DFT using the *Gaussian16* package. Solvent effects of methanol were embedded by employing PCM. Excited state analysis with TDDFT at the ground state optimized geometry obtained at CAM-B3LYP/6-31G* level using the constraint `freeze` in order to prevent the formation of a lactone structure brings out information as tabulated in table 18.

Table 18: Electronic excitation energies of the important electronic states of Rho1-BODIPY1 obtained at CAM-B3LYP/6-31G* level in methanol.

State	Energy (*eV*)	Orbital transitions
S_1	2.89	within BODIPY1
S_2	3.15	within Rho1
S_3	3.71	within Rho1

The S_3 state particularly is the two-photon active state owing to its high TPA cross-section which is also a reflection of the corresponding transition to two-photon active S_2 state of the isolated Rho1 moiety. The excited state analysis here can be considered to be the same as reported earlier in Section 4.9.2. The earlier assumption can be reaffirmed i.e., if an energy transfer is to be initiated by a two-photon excitation, the molecule would be first directly excited to the S_3 state. This is followed by an internal conversion to the S_2 state and then the energy is transferred to the S_1 state.

A proper description of the dynamics of the dyad is attained by the LVC model that is parameterized based on the former electronic structure calculations. Mass- and frequency-weighted coordinates are used throughout.

$$\begin{aligned}\hat{H} = &\sum_{i=1}^{N}\left(-\frac{\omega_i}{2}\left(\hat{q}_i^2+\hat{p}_i^2\right)+\sum_j \kappa_{i,j}\,q_i\,|LE^j\rangle\langle LE^j|\right)\\ &+j_{DA}\left(|LE^A\rangle\langle LE^D|+|LE^D\rangle\langle LE^A|\right)+\Delta E\end{aligned} \tag{141}$$

where $\hat{q}_i$ is the position operator, $\hat{p}_i = -i\hbar\frac{\partial}{\partial q_i}$ the momentum operator, $\kappa_{i,j}$ the vibronic couplings, j_{DA} the Coulombic EET coupling and ΔE is the electronic offset.

The S_2 and S_1 states of the Rho1-BODIPY1 dyad as well as 266 normal modes (N in the Hamiltonian) of which 117 are coupled to the S_1 and thus to the BODIPY1 fragment and 149 are coupled to the S_2 and thus to the Rho1 fragment, respectively are depicted in fig. 50. The vibronic coupling constants $\kappa_i^{(\alpha)}$ are computed by projecting the gradient of the two relevant excited states at the FC geometry onto the normal modes, the normal modes and their respective frequencies ω_i were obtained by normal mode analysis for the donor and acceptor fragment respectively. Analysis of the spectral densities (that can be computed from the vibronic couplings and is an indicator as to how efficient the energy can be absorbed in a certain spectral region, computed as $J_{k,l} = \sum_i^N \frac{\bar{\Delta}\kappa_i^{(k)}\kappa_i^{(l)}}{2((\omega-\omega_i)^2+\bar{\Delta}^2)}$, where $\bar{\Delta}$ is the average difference of frequencies scaled by 0.2) show, that it is sufficient for the description of the dyad to only consider the couplings $\kappa_i^{(\alpha)}$ between the normal modes ond one of the fragments. The electronic coupling is derived by the TDC method (ref. eq. 138) and is calculated to be 0.024 eV. In order to describe the dayd as accurately as possible the energy difference between the two considered electronic states $\varepsilon_m = 0.25eV$ was adapted from the experimental UV/vis absorption spectra.

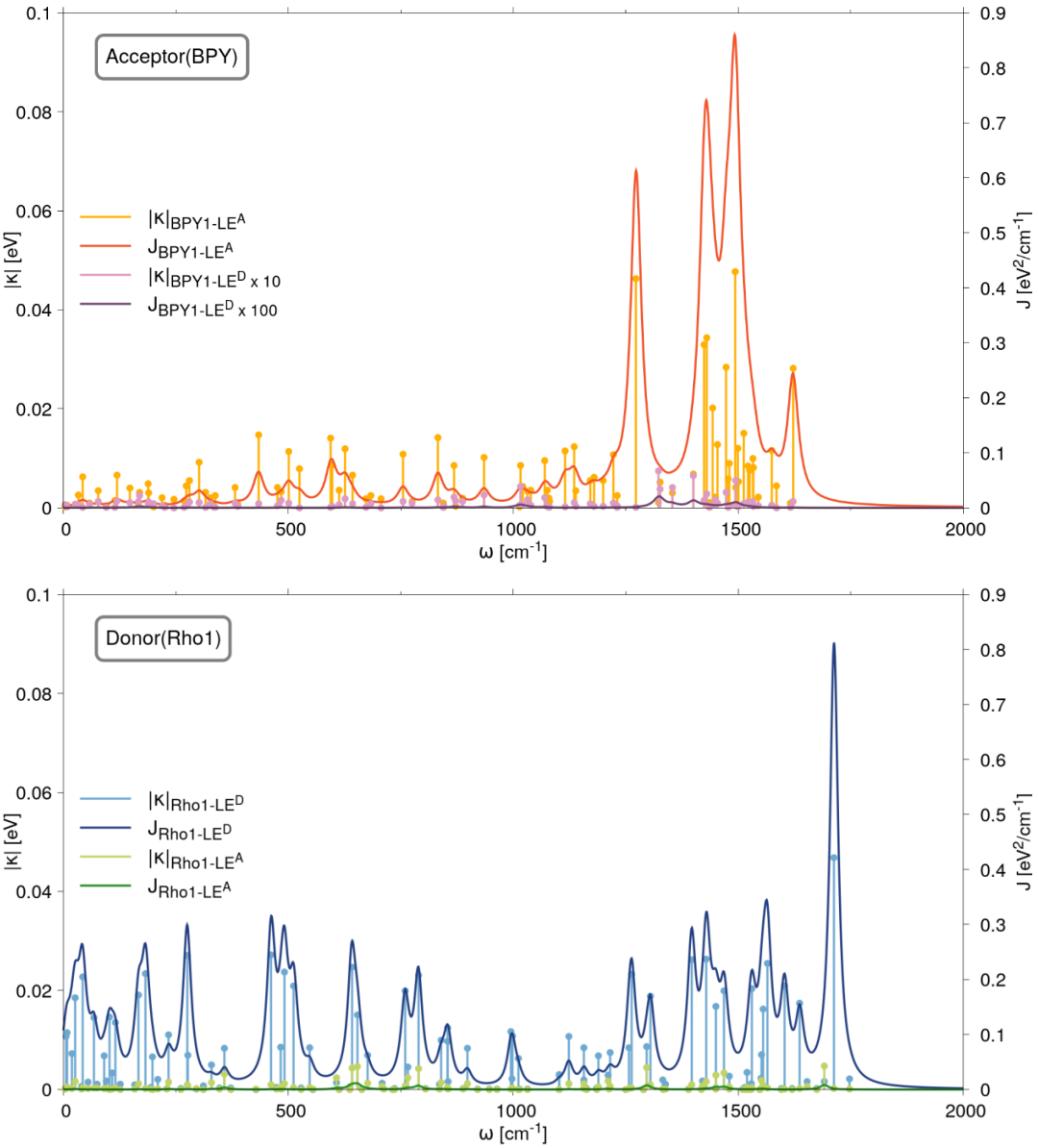

Figure 50: Coupling of the vibrational modes to the electronic states with orbital transitions within Rho1 and BODIPY1 fragment obtained at CAM-B3LYP/6-31G* level in methanol.

Through quantum dynamics as depicted in fig. 51, an initial decay to the S_1, mainly 'localized' on the acceptor fragment, is found until 200 fs. Although a bit faster than the experiment this is in good agreement with the time-resolved spectroscopic measurements where the energy transfer dynamics occurs on a 300 fs timescale. As the spectroscopic findings indicate, the simulations also get to a stationary superposition in the population transfer, which is also supported by the non-negligible real part of the coherence. The imaginary part (transient coherence) on the other hand determines the energy transfer and decays to zero. This decay is along the same timescales as that of the population transfer.

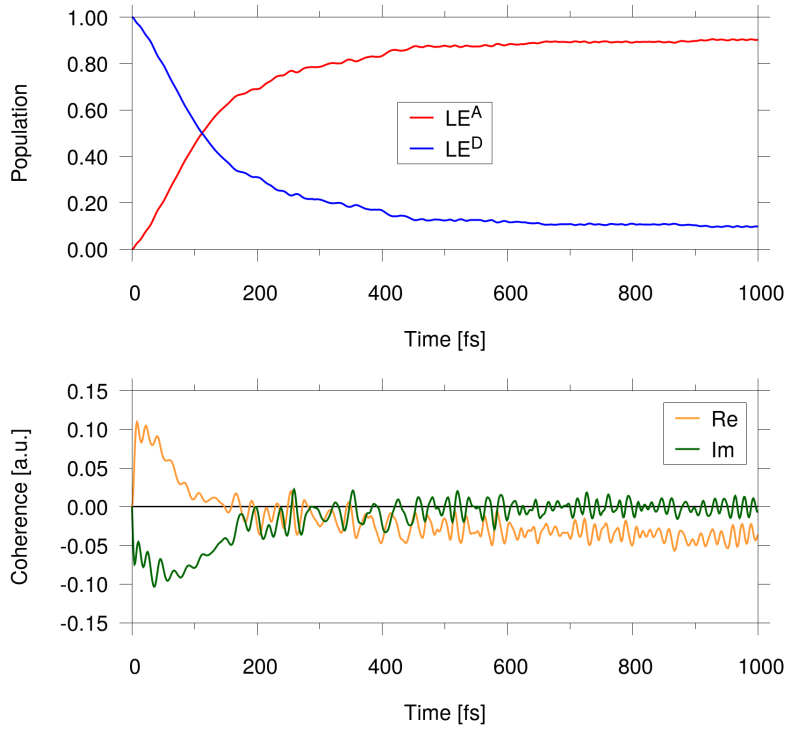

Figure 51: Population and coherence phenomena of the electronic states corresponding to orbital transitions within Rho1 and BODIPY1 fragments.

4.10 RHO4-BODIPY2 MOLECULAR DYAD

Fig. 52 depicts the molecular structure of the synthesized molecular dyad where the Rho4 moiety has been linked together with the BODIPY2 through the same acetylene bond. Here, this seems as the desirable dyad consisting of Rho4 moiety which has the highest TPA response as the donor fragment and the BODIPY2 exhibiting the desirable red-shift in the absorption maximum as the acceptor fragment. As discussed in section 4.8, the synthesis of Rho4-BODIPY2 molecular dyad is an important step in achieving the characteristics for the potential applications. The investigation of intramolecular energy transfer in this dyad is intended to examine the through-space EET mechanism.

The approach to evaluate the rate of energy transfer would be through the same IDA as well as the TDC method.

4.11 RESULTS FOR RHO4-BODIPY2 DYAD

4.11.1 *Electronic structure calculations*

The optimization of the ground state geometry of Rho4-BODIPY2 molecular dyad was done with tight optimzation criteria using fine integration grids. The ground state equilibrium geometry was optimized employing the GGA based hybrid B3LYP functional of the DFT method along with 6-31G* basis set. The solvent effects of methanol were modeled with PCM solvation model. The correspondence of the

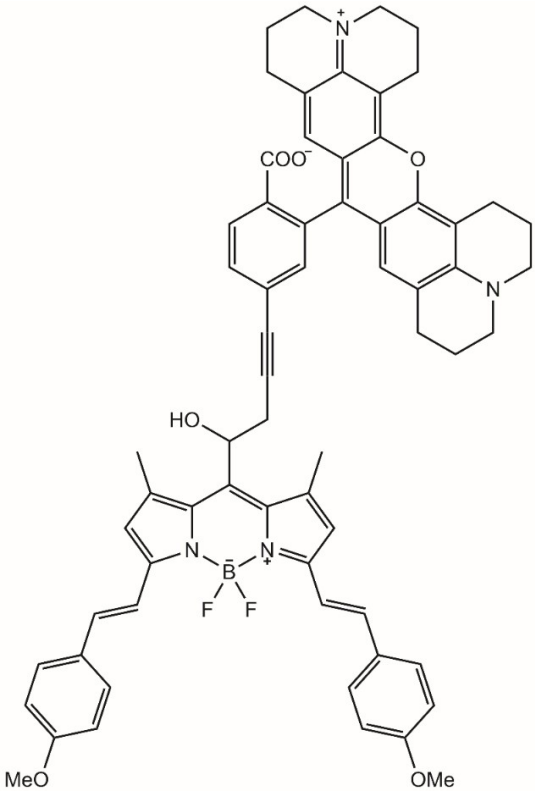

Figure 52: Molecular structure of Rho4-BODIPY2 molecular dyad.

ground state equilibrium geometry to a real minimum without negative frequency was confirmed by the frequency analysis.

At the same ground state equilibrium geometry at the B3LYP level, the vertical excitation energies were estimated by employing the linear-response TDDFT. Following the same methodology as that for the Rho1-BODIPY1 molecular dyad, a proper benchmark was obtained with the hybrid B3LYP, the long-range corrected CAM-B3LYP and the "half-and-half" BHandHLYP functionals of the DFT method. Since the correspondence of the ground state equilibrium geometry for the Rho1-BODIPY1 dyad to the global minimum was thoroughly checked for with the help of 1D-PES scans, the same correspondence of the ground state equilibrium geometry for the Rho4-BODIPY2 dyad to the global minimum could be safely assumed given the exactly same geometric architecture. The analysis of results for the Rho4-BODIPY2 dyad begins directly with the excited electronic states.

4.11.2 *Electronic excitations*

Fig.53 depicts the experimentally measured absorption spectra of the Rho4-BODIPY2 dyad along with that of the isolated free Rho4 and BODIPY2 molecular fragments in methanol. The absorption maxima of Rho4 at 575 nm and BODIPY2 at 649 nm correspond to the vertical excitation energies of 2.15 eV for Rho4 and 1.91 eV for BODIPY2, respectively. The dyad has the desirable characteristics where the rhodamine fragment as the donor group has the higher excitation energy than the BODIPY fragment as the acceptor group.

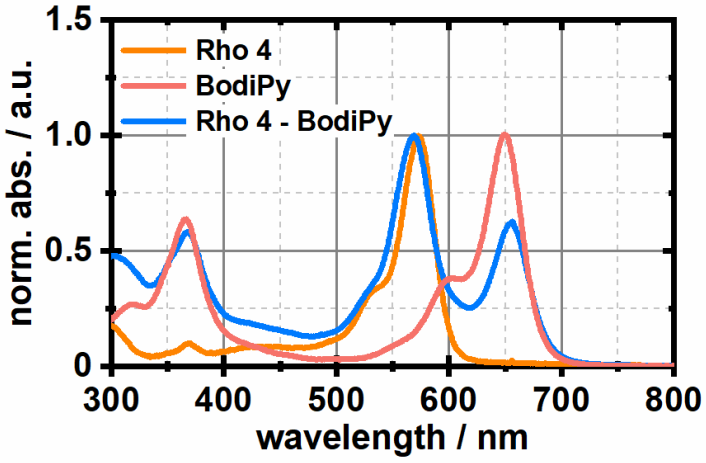

Figure 53: Experimental absorption spectra of the Rho4-BODIPY2 molecular dyad as well as that of the isolated free Rho4 and BODIPY2 moieties in methanol.

The excited state involving transition within Rho4 fragment has higher excitation energy than that of transitions within BODIPY2 fragment in the dyad in all calculations. The calculations with CAM-B3LYP present more or less the same picture, the difference being the order of the excited states. Here too, the lowest singlet excited state S_1 is a bright state consisting of $\pi - \pi^*$ HOMO to LUMO transition within the BODIPY2 fragment. The next higher singlet excited state S_2, also a bright state consists of a $\pi - \pi^*$ transition from the HOMO - 1 to the LUMO + 1 within the Rho4 fragment. The next higher singlet excited state of interest S_4 is a TPA-allowed dark state involving transitions within the Rho4 fragment which has a mixture of charge transfer to the *o*-carboxylphenyl ring from the HOMO - 4 to the LUMO + 1.

Table 19 enlists the vertical excitation energies along with the oscillator strengths f of the excited states of interest in a benchmarking process with different functionals of the DFT method. Referring back to the earlier sections on rhodamines and BODIPYs, the lowest singlet excited states of the isolated free Rho4 and BODIPY2 reflect in the $\pi - \pi^*$ excitations in the Rho4-BODIPY2 molecular dyad, respectively. The HOMO $\rightarrow$ LUMO $\pi - \pi^*$ transition of the isolated Rho4 (S_1 state) is the HOMO - 1 $\rightarrow$ LUMO + 1 (S_2 in CAM-B3LYP) $\pi - \pi^*$ transition in Rho4-BODIPY2 dyad. Likewise, the HOMO $\rightarrow$ LUMO $\pi - \pi^*$ transition of the isolated BODIPY2 (S_1 state) is the HOMO $\rightarrow$ LUMO (S_1 state in CAM-B3LYP) $\pi - \pi^*$ transition of the Rho4-BODIPY2 dyad.

The S_2 excited state of the isolated Rho4 showing transition from HOMO - 1 $\rightarrow$ LUMO appears as the S_7 and S_4 excited state in calculations with B3LYP and CAM-B3LYP, respectively. Hence, these are also the two-photon allowed state due to the high TPA cross-sections. Based on the entire TDDFT analysis, an assumption can be made that if the dyad undergoes an initial two-photon excitation, the S_4 (CAM-B3LYP) state relating to the Rho4 fragment would be first excited. An internal conversion to the S_2 (CAM-B3LYP) state involving $\pi - \pi^*$ transition within the Rho4 fragment follows after the two-photon excitation. Subsequently, the EET would take place from the S_2 state to the S_1 excited state i.e., from the Rho4 to the BODIPY2 fragment. The investigation of the intramolecular energy transfer is detailed in the following sections.

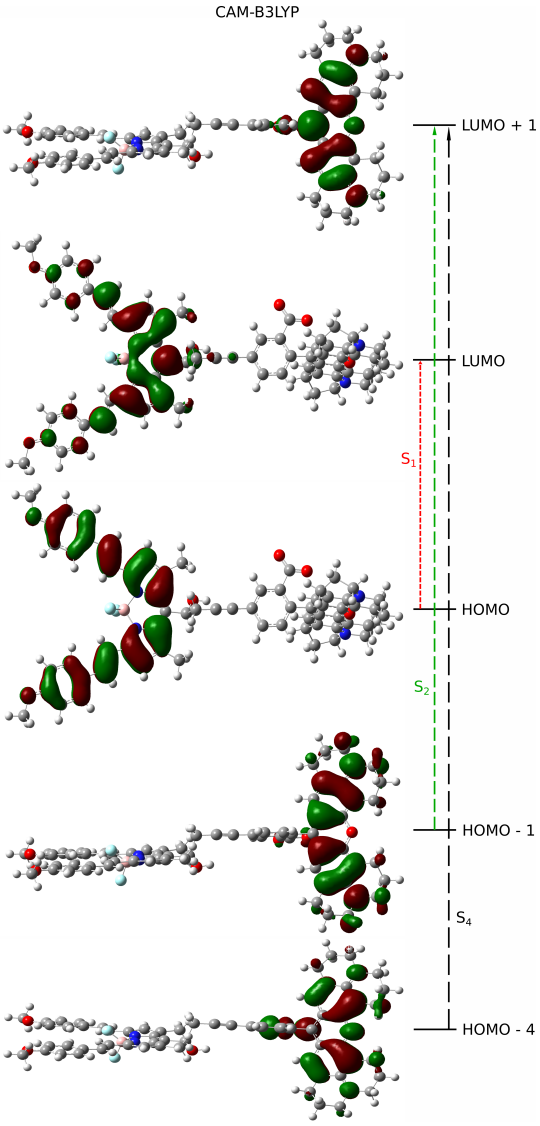

Figure 54: Frontier orbitals involved in the transitions of interest, precisely the orbital transitions within BODIPY2 (indicated by red dashed arrow), Rho4 (indicated by green dashed arrow) and TPA-active Rho4 excited state (indicated by black dashed arrow). The frontier orbitals of Rho4-BODIPY2 are obtained at CAM-B3LYP/6-31G* in methanol.

4.11.3 *Spectral overlap*

Based on the molecular orbital picture above, the vibrationally resolved electronic spectra of the respective electronic states consisting of $\pi - \pi^*$ orbital transitions within Rho4 and BODIPY2 fragments were simulated with the analytical TD method using the VG model. Fig. 55 depicts the overlap between the computed vibronic emission and absorption spectra of Rho4 and BODIPY2 respectively. Here specifically, the emission spectra of Rho4 corresponds to the S_2 excited state and the absorption spectra of BODIPY2 corresponds to the S_1 excited state. The overlap appears to be very low.

The overlap between the computed vibrationally resolved electronic spectra is very low when compared to the experimentally measured absorption spectra. The

Table 19: Electronic excitation energies, oscillator strengths f of the electronic excited states of interest at the ground state equilibrium geometry of Rho4-BODIPY2 computed with different functionals with 6-31G* basis set in methanol.

DFT functional	State	Energy (eV)	f
B3LYP	S_1 (BODIPY2)	1.97	1.06
	S_5 (Rho4)	2.63	0.86
	S_7 (Rho4)	2.80	0.10
BHandHLYP	S_1 (BODIPY2)	2.16	1.16
	S_2 (Rho4)	2.95	1.11
	S_3 (Rho4)	3.71	0.01
CAM-B3LYP	S_1 (BODIPY2)	2.14	1.13
	S_2 (Rho4)	2.95	1.11
	S_6 (Rho4)	3.71	0.01

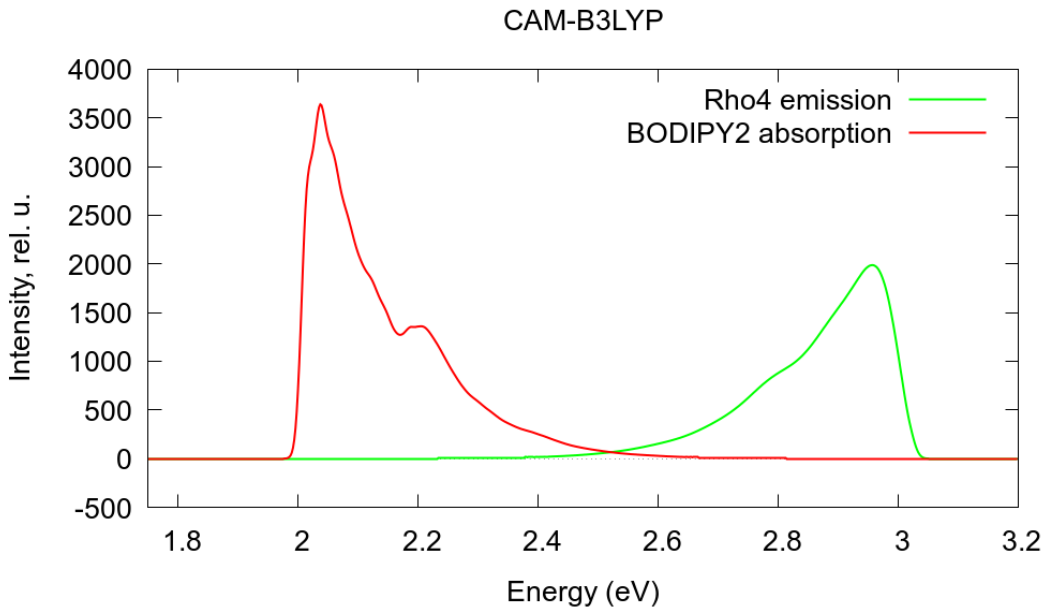

Figure 55: Overlap of the Rho4 emission and BODIPY2 absorption spectra obtained at the CAM-B3LYP/6-31G* level in methanol. Spectra computed with the TD analytical method.

overlap between the experimentally measured absorption spectra of Rho4 and BODIPY2 is quite significant. This could be attributed to the differences between the individual maxima of the excitation for the Rho4 and BODIPY2 fragments. In the experimental absorption spectrum, the difference between the maxima is 0.25 *eV* whereas it is 0.81 *eV* in the TDDFT approximations. Due to this difference in the computed and experimental spectral overlap, a benchmark is attempted in the process of calculating the rate of energy transfer by introducing an energy offset. This offset is the difference between the absorption maxima of the Rho4 and BODIPY2 fragments in the absorption spectrum of the dyad (refer fig. 53). In this way, a

shift in either the absorption or emission spectra is created which in turn results in greater spectral overlap.

The overlap integral after the inclusion of an offset or a shift is calculated as:

$$J_{DA}(\text{shift}) = \int_{-\infty}^{\infty} dE\, F_D(\Delta E)\varepsilon_A(E) \tag{142}$$

where ΔE is the energy offset or the shift in energy, $F_D(\Delta E)$ and $\varepsilon_A(E)$ represent the donor emission and acceptor absoprtion, respectively. To bring the theoretically calculated vibronic spectra in line of agreement with the experiment, it would be appropriate to introduce an energy offset of 0.56 eV so that the difference between the maxima of excitation of the Rho4 and BODIPY2 fragments also becomes 0.25 eV. Fig. 56 depicts the overlap comparison without including the shift (solid line) and after including the shift (dashed line) between the computed emission and absorption spectra of Rho4 and BODIPY2 respectively.

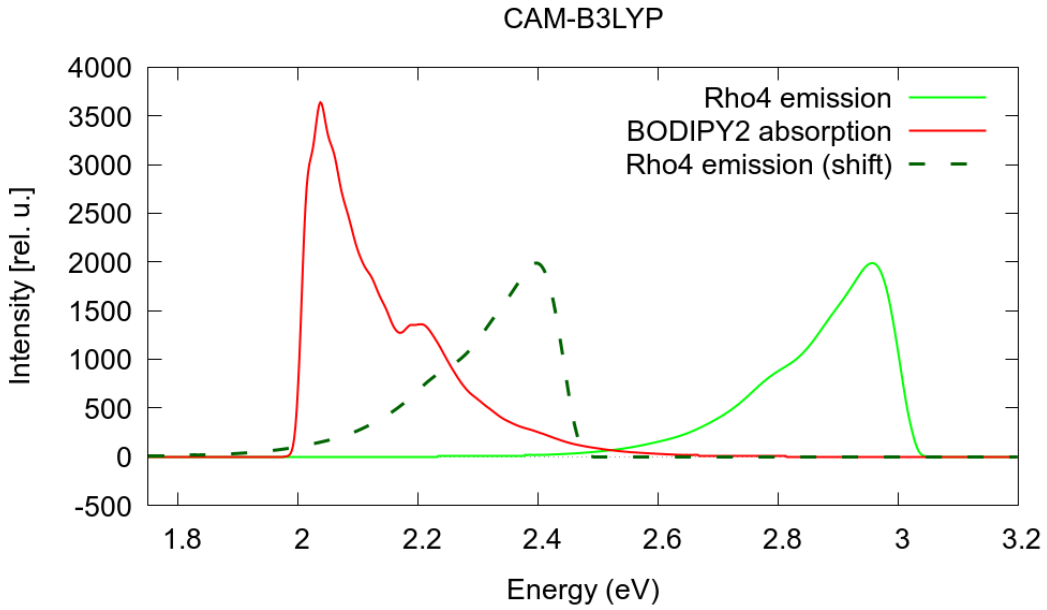

Figure 56: Overlap of the Rho4 emission and BODIPY2 absorption spectra without and with shift obtained at the CAM-B3LYP/6-31G* level in methanol. Spectra computed with the TD analytical method.

It is clearly visible that the overlap between the emission and the absorption spectra increases after the inclusion of the energy offset or the shift of 0.56 eV. The overlap integrals are listed in the table 20 after the normalizing the spectra.

4.11.4 *Dipole-dipole and Coulombic coupling*

The coupling between the donor and acceptor groups were calculated using the IDA (ref. eq. 122) and the TDC method. For the generation of TDCs, a 3D-mesh of $40 \times 40 \times 40$ along each axes was defined. The box is centered at the molecular coordinate origin. By checking for convergence of the Coulombic coupling with respect to the number of grid points, the suitable number of grid points was arrived

Table 20: Overlap integral calculated with respect to the computed vibronic spectra obtained at CAM-B3LYP/6-31G* level in methanol. J_{DA} represents the overlap without any shift and J_{DA} (shift) represents the overlap after inclusion of a shift in the spectra.

J_{DA}	J_{DA} (shift)
0.2723	31.0691

at. The grid spacing is the box length divided by the grid points. On checking for convergence from 150 to 200 grid points with intervals of 10 points each time, the Coulombic couplings were found to be consistent. The final couplings with respect to both dipole-dipole approximation and TDC method are listed in table 20.

Table 21: Calculated couplings with dipole-dipole approximation and TDC method at CAM-B3LYP/6-31G* in methanol.

$V_{DA}^{dip}(eV)$	$V_{DA}^{TDC}(eV)$
0.0041	0.0033

4.11.5 *Rate of intramolecular energy transfer*

With the availablility of the values of the necessary variables i.e., the couplings and the overlap integral, the EET rate could be calculated with eq. 139. The inverse of the rate gives out the timescale of energy transfer as already expressed in eq. 140. The rates and timescales of intramolecular energy transfer for the respective overlap without and with the shifts are listed in table 22.

Table 22: Calculated rates and timescales of EET at CAM-B3LYP/6-31G* level in methanol according to IDA and TDC method for the spectral overlap without and with the shifts.

Shift (eV)	Theory	$k_{EET}(s^{-1})$	τ_{EET}
0	IDA	1.6236×10^9	615.89 ps
	TDC	1.0511×10^9	951.35 ps
0.56	IDA	1.8552×10^{11}	5.39 ps
	TDC	1.2004×10^{11}	8.33 ps

4.11.6 *Time-resolved spectroscopy of Rho4-BODIPY2 dyad*

The experimental investigation of the ultrafast dynamics of the Rho4-BODIPY2 molecular dyad was performed by employing UV/vis transient absorption spectroscopy. The Rho4 fragment was initially excited with a pump pulse at a central wavelength of 560 nm. The negative signal around 550-620 nm indicates bleaching of the Rho4 ground state (GSB1). The excited state absorption (ESA1) at the central wavelength of 470 nm is due to the population of the excited state of Rho4. The

decay occurs on the 200-500 fs as it can be seen in fig. 57 that the amplitudes of these signals already decreases in the < 500fs range. On the other hand, there is a simultaneous ground state absorption of the BODIPY2 indicated by an additional bleaching signal (GSB2) centered at 670 nm.

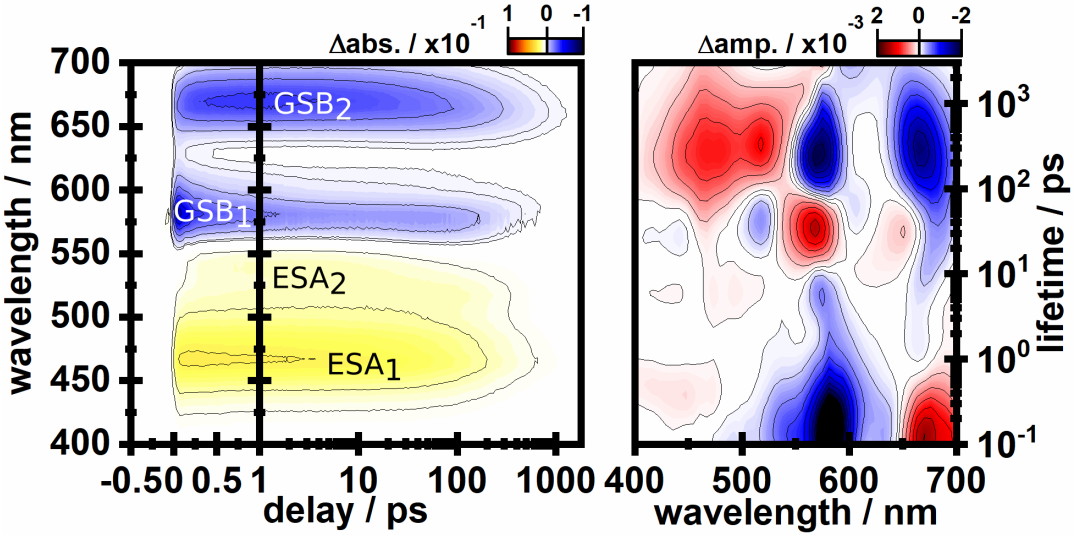

Figure 57: Time-resolved measurements of the Rho4-BODIPY2 molecular dyad.

Fig. 58 displays the excited state dynamics at selective wavelengths of 575 and 670 nm corresponding to the excitations of Rho4 and BODIPY2, respectively. In comparison to the transients where the bleaching signal at 575 nm decreases by 50 % of its initial value in the first 300 fs after photoexcitation and GSB2 reaches more than 90 % of its maximum value on the same timescale, a conclusion is reached that an efficient EET from Rho4 to BODIPY2 occurs. This EET levels off on reaching an equilibrium with the locally excited Rho4. The excited state decays completely in less than 1 ns.

The overall transient absorption spectroscopic investigation reveals that the EET dynamics happen on the timescale of 150-500 fs range.

4.12 DISCUSSION

The theoretical as well as the experimental estimation of the two-photon activity of the rhodamines is found to be complementary to each other. The BODIPY groups show change in properties especially with respect to BODIPY2 which has additional conjugated substituent groups. These substituent groups not only lead to a red-shift in the wavelength of the absorption maximum but also a multi-fold increase in the TPA cross-sections in the excited state corresponding to the localized orbital transition within the π-system.

The timescales of EET within the Rho1-BODIPY1 dyad has been estimated theoretically by several methods: IDA, TDC and quantum dynamics. The coupling between the Rho1 and the BODIPY1 fragments calculated through the dipole-dipole approximation and the TDC method is very weak. The spectral overlap between their respective emission and absorption spectra is significantly good indicating probability of efficient EET. The calculated timescales range from 80 fs to 10 ps. On

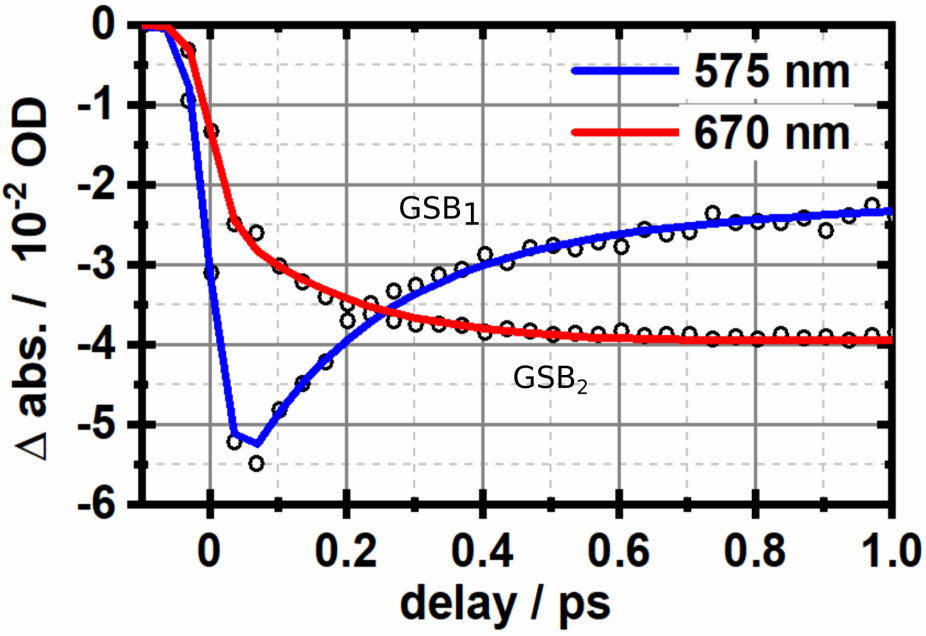

Figure 58: Transient absorption spectra of the Rho4-BODIPY2 dyad.

the other hand, quantum dynamical investigations on the adapted Rho1-BOIDPY1 reveal ultrafast EET dynamics occuring on a timescale of 200 fs. The explanation behind this finding is based on the phenomenon of transient coherence.

In the case of Rho4-BODIPY2 dyad where the time-resolved spectroscopic displays an ultrafast EET dynamics within the 150-500 fs range, the conventional approach of the Förster approximation or the TDC method fail to reach an agreement with the experimental findings. Even after the inclusion of an energetic shift in the spectral overlap taking into consideration the probable shortcomings of the TDDFT calculations, the estimated timescales fall in the range of $5\ ps - 1ns$. For this dyad too, the quantum dynamical investigations on the Rho1-BODIPY1 dyad are more reliable than the conventional Förster theory to complement the experimental findings. Therefore, it can be concluded that it is the transient coherence which determines the energy transfer within the dyad and it cannot be described by Förster theory.

5

PHOTOCHEMISTRY OF DEACM UNCAGING

In Section 3.7, the role of PPGs for precise and selective spatiotemporal release of molecular compunds has been extensively illustrated. The [7-(dimethylamino)coumarin-4-yl]methyl (DEACM) class of photocages exhibit promising features including absorption in the visible range (350 - 450 nm) of the spectrum [60, 68, 79, 101, 102, 109]. The parent coumarin compound exhibits low solubility in water so the addition of leaving groups (LG) can lead to improved aqueous solubility.

In the following theoretical study, an attempt to interpret the LG-specific kinetics for the three DEACM species i.e., DEACM-SCN, DEACM-N_3 and DEACM-Carb has been made (ref fig. 59). To understand the origin of the early photocleavage steps of these DEACM species, excited-state PES scans are performed. The PES scans also include the dihedral angle of the LG relative to the coumarin scaffold besides the dissociative DEACM-LG distance coordinate.

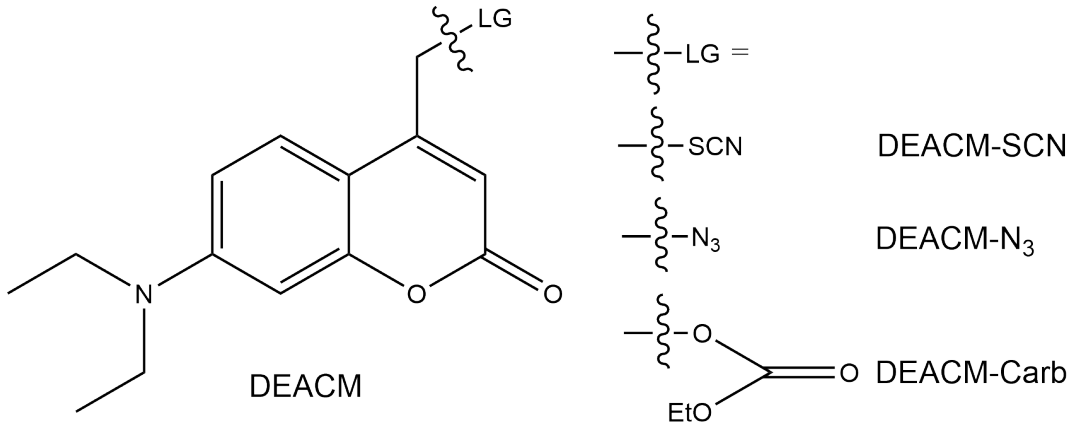

Figure 59: Left: Structure of the DEACM parent compund. Right: Leaving groups attached to the DEACM scaffold. The wiggly line denotes the cleavage site after absorption of a visible photon.

5.1 COMPUTATIONAL PROCEDURE

All electronic structure calculations were performed with the *Gaussian16* program, revision *B.01* [49] unless noted otherwise. Ground state structures were optimized and their frequencies analyzed using DFT whereas excited state calculations were performed at the TDDFT level of theory using the ωB97XD long-range corrected functional in combination with the 6-31G* basis set. Fig. 60 shows the main reaction coordinates for the analysis of photochemical pathways. 1D- and 2D- PESs were simulated by performing "semi-relaxed" scans along the reaction coordinate indicated in fig. 60 in the electronic ground state followed by TDDFT single point calculations at each point along the relaxed surface scan. Solvent effects were treated with the PCM model.

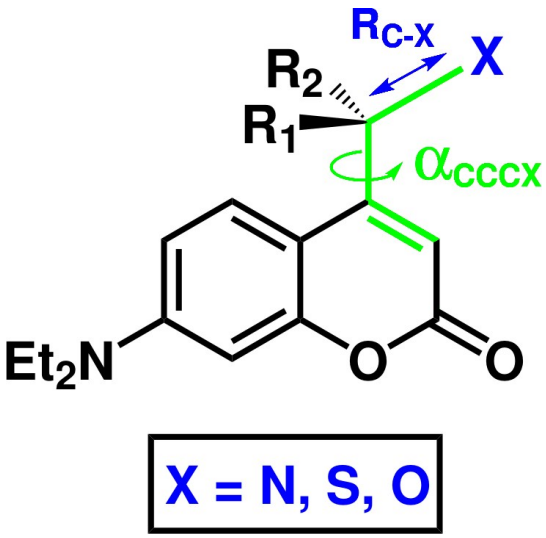

Figure 60: Relevant reaction coordinates for coumarin uncaging: the R_{C-X} bond and the dihedral angle α_{CCCX}. Reproduced from [55] with permission from the Royal Society of Chemistry.

5.2 RESULTS

5.2.1 *Excited state analysis*

The first excited singlet state S_1 is identified to be the spectroscopically bright state in all three systems. The $\pi - \pi^*$ transition from HOMO to LUMO within the conjugated π-system localized exclusively on the DEACM coumarin moiety is the associated excitation pattern corresponding to the S_1 state. Table 23 enlists the excitation energies E and oscillator strengths f of the first singlet excited state of the three DEACM species.

Table 23: Excitation energies E and oscillator strengths f of the S_1 state of the DEACM species obtained at ωB97XD/6-31G* level of theory.

System	E (*eV*)	f
DEACM-SCN	4.14	0.48
DEACM-N_3	4.21	0.47
DEACM-Carb	4.18	0.49

5.2.2 *1D PES scans*

Fig. 61 shows 1D- relaxed PES scans of the higher excited states of the three DEACM moieties. In all the systems, a dissociative character is adopted by the S_1 state beyond a S_1-S_2 crossing point and/or additional S_1-S_n crossing points at larger distances. An indication of the stabilization of the several dissociative states is brought out by multiple state crossings within the singlet manifold. At bond extensions of approximately 0.3-0.5 Å from the respective FC geometries lies the region of multiple state crossings.

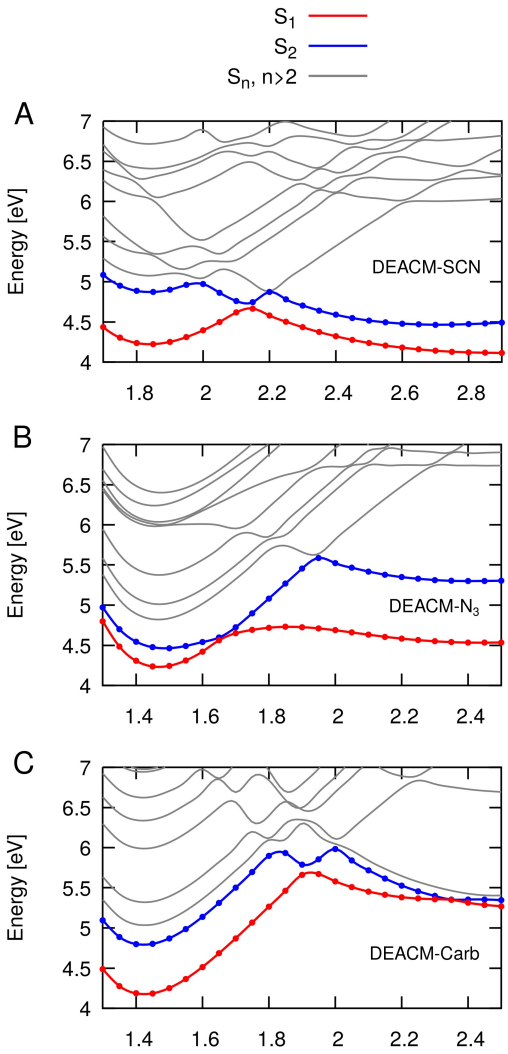

Figure 61: 1D relaxed scans in vaccum obtained at the TD-ωB97XD/6-31G* level of theory displaying the singlet state manifold of DEACM-SCN (panel A), DEACM-N_3 (panel B) and DEACM-Carb (panel C) respectively. Reproduced from [55] with permission from the Royal Society of Chemistry.

The main interpretation to drawn in all systems is that the dissociation cannot occur from the S_1 (DEACM) state of $\pi - \pi^*$ character upon reaching photoexcitation. In order to induce a dissociative character to the S_1 state a barrier needs to be overcome. Hence, dissociation could be expected to proceed adiabatically or else involve nonadiabatic state crossings, depending on the proximity of the neighbouring S_2 and S_n states.

5.2.3 *2D PES scans*

The 2D PES scans of the S_1 state including the dihedral angle can be observed in fig. 62. There are slight differences in the ground-state equilibrium structures of the three systems with respect to the dihedral angle α_{CCCX}. The global minimum of the DEACM-N_3 and DEACM-Carb systems lies at the linear geometry with a non-negligible admixture of the twisted species at the room temperature. DEACM-SCN

on the other hand has a twisted ground-state geometry with a small admixture of the linear structure.

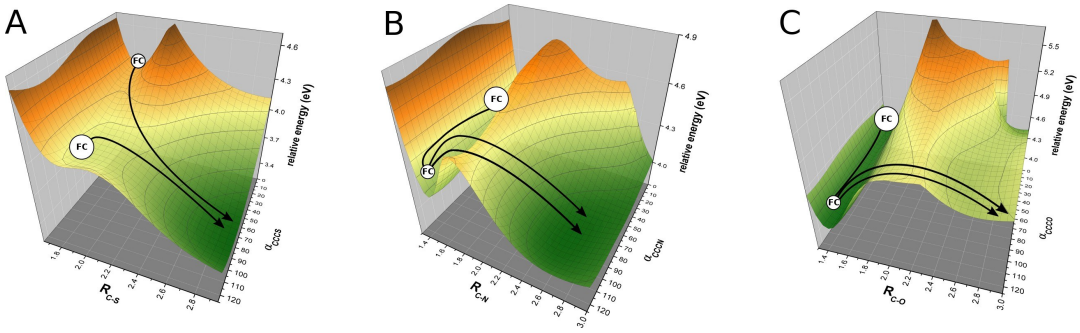

Figure 62: 2D relaxed scans in vacuum obtained at the TD-ωB97XD/6-31G* level of theory displaying the S_1 state surfaces of DEACM-SCN (panel A), DEACM-N_3 (panel B) and DEACM-Carb (panel C), respectively. Reproduced from [55] with permission from the Royal Society of Chemistry.

Observation of fig. 62 reveals a correlation between motion in the R_{C-X} and α_{CCCX} coordinates on the S_1 PES in all cases such that a typical reaction path as depicted in fig. 62 necessarily involves a concerted motion in these coordinates. Large conformational displacements up to almost perpendicular orientations are possible due to the flat PES topology as a function of the dihedral angle α_{CCCX}. Fig. 62 indicates two types of initial photoexcited states originating in the twisted or linear ground-state conformations, are initially well separated. The linear subensemble of the S_1 PES shows evolution towards twisted conformations owing to its conformational flexibility along with a delay due to the torsional motion. Extension of R_{C-X} bond coordinated is facilitated with a much reduced barrier height upon reaching strongly twisted conformations in the S_1 state. In the case of DEACM-SCN, there exists a barrierless excited-state path in a strongly twisted geometry. The DEACM-N_3 and DEACM-Carb by contrast retain a reduced barrier height away from the mainly populated linear geometry.

The differences in dissociation barriers could be related to the intrinsic stability of the respective R_{C-X} bond that is to be cleaved. The R_{C-S} bond of the DEACM-SCN caged compound is significantly elongated in its electronic ground state leading to more pronounced energetic stabilization from π-conjugation of the methylene carbon atom that bears the thiocyanate group with the coumarin systems. The formation of a more sp^2 type electronic configuration in which the methylene carbon atom features its vacant p orbital perpendicular to the coumarin plane to maximize the π-overlap is facilitated by the pre-labilization of the R_{C-S} bond. This makes it evident the rotation around the α_{CCCX} angle affecting the DEACM-SCN S_1 surface in a very pronounced fashion. As a result, there is a rapid drop in the high energy barrier even with small rotational displacements from the FC conformation.

5.3 DISCUSSION

The TDDFT calculations lead to the following inferences:

- A cross-over between an initially excited S_1 $(\pi - \pi^*)$ state localized on the DEACM moiety and a dissociative state localized on the LG whose electronic

character dominates the S_1 state at larger bond distances mediates the dissociaton.

- The R_{C-X} bond length and the α_{CCCX} dihedral angle are the two geometric parameters mediating the excited-state uncaging.

In all cases the rigid DEACM scaffold plays the role of a spectator after serving as a light harvesting antenna upon S_1 $(\pi - \pi^*)$ bright state after excitation. In the 2D relaxed PES scans of the S_1 surface as a function of the R_{C-X} and α_{CCCX} coordinates, the bond cleavage in all systems is preceded by a rotation of the dihedral angle upto an almost perpendicular orientation of the LG with respect to the DEACM plane. Rotation in the S_1 state at the FC bond distance is barrierless in contrast to the S_0 ground state. The DEACM-SCN species undergoes barrierless dissociation whereas the DEACM-N_3 and DEACM-Carb moieties remain trapped in a comparatively steep potential valley necessitating thermal activation.

CONCLUSION AND OUTLOOK

The objective of this work has been the theoretical investigation of the vibrationally promoted electronic resonance (VIPER) two-dimensional infrared (2DIR) experiment and the extension to two-photon absorption (TPA) and the intramolecular energy transfer within a molecular dyad consisting of a two-photon active donor group. Additionally there is a computational study to elucidate the photochemical mechanism of uncaging in [7-(dimethylamino)coumarin-4-yl]methyl (DEACM) class of photocages with respect to different leaving groups (LG).

The setup for the theoretical investigation of the VIPER experiment in continuation to the approach implemented by Jan von Cosel has been extended to include the computation of a two-photon vibrationally resolved electronic absorption spectrum inclusive of the first-order effects Herzberg-Teller (HT) effects. In the real experimental scenario, a near-infrared (NIR) pulse would replace the off-resonant UV/vis pump pulse. The lineshape of one-photon absorption (OPA) and TPA spectra is the same within the zero-order Franck-Condon (FC) approximation. To get more information, HT effects which are dependent on the changes in the nuclear coordinates are included as well. The aspect of the vibrational normal mode to be pre-excited was also dealt with in detail. The extent of the VIPER activity of the vibrational mode is determined mainly by the measure of the dimensionless displacement. Hence, the electronic absorption spectrum that is probed by the UV/vis or the near-infrared (NIR) pulse is modified by the vibrational pre-excitation.

For the DMA-NDBF molecule, the vibronic spectrum is dominated by the FC contributions and the effects of HT couplings are insignificant as is typically the case for electronically-allowed transitions. The NO_2 bend shows the highest VIPER activity than the one followed by a ring distortion mode in the high frequency range of the IR spectrum which is evident from the magnitude of the dimensionless displacements. The greater the dimensionless displacement, the larger the influence on the equilibrium structure of the molecule upon vibrational pre-excitation. In rhodamine, the one-photon vibronic absorption spectrum is described almost entirely by the FC contributions and the HT terms provide a very weak contribution to the spectrum. The two-photon vibronic absorption spectrum of the rhodamine is in principle the spectrum obtained from HT contributions. This can be explained on the basis of molecular orbital changes in the non-linear transitions. One side of the xanthene ring of the rhodamine acts as an electron-donating group to transfer electron density utilizing the π-backbone of its structure to its other side acting as the electron-accepting group. This kind of enhanced non-linear optical characteristics can be attributed to the presence of the donating and accepting groups in rhodamine. As a measure of the dimensionless displacements of the vibrational modes, two ring-distortion modes were probed for their VIPER activity. Both the ring modes were found to have no significant intensity among vibrational pre-excitation.

The extended setup implememented in this work has also been verified with the reported calculations on conjugated molecules like pyrimidines. Apart from the investigations on the two-photon active photolabile protecting groups (PPGs) like

DMA-NDBF or a laser dye like rhodamine, an extensive work on Coumarin6 is also in progress. These theoretical simulations when complemented with the experimental measurements could serve as a good benchmark for future development of two-photon active photocages.

The second part of this thesis deals with chromophores which can be linked together to exhibit an intramolecular energy transfer with further possible applications in uncaging with the help of a LG. Rhodamines are naturally very good candidates as the donor group due to their excellent TPA characteristics. They are well-known for their applications as laser dyes and hence can facilitate absorption through TPA. Electronic structure calculations and two-photon excitation fluorescence (TPEF) measurements show very good agreements about the two-photon activity of the rhodamine derivatives. It is confirmed that the Rho4 moiety which is the derivative of the commercially available rhodamine 101 (Rh101) compound shows the highest two-photon activity in the second electronically singlet excited state. Lots of literature is available which explains the overestimation of excitation energies by TDDFT which is evident in the calculations for the rhodamine and BODIPY derivatives in this work.

The setup for the investigation of the intramolecular energy transfer within the rhodamine-BODIPY dyad has also been implemented. From the electronic structure calculations, an assumption can be made that if the energy transfer within the molecular dyad is to be initiated with two-photon excitation, the molecule would be excited to the electronic state corresponding to the orbital transitions within the rhodamine fragment. An internal conversion (IC) to the state corresponding to the orbital transitions within the same fragment follows and finally the energy transfer to the BODIPY fragment occurs which can then trigger cleavage of the leaving group.

The time-resolved spectroscopic measurements indicate timescales of between 150-500 fs for the excitation energy transfer (EET) within the Rho4-BODIPY2 dyad. The conventional approach to theoretically estimate the timescale through the Förster theory lags behind the experimental observations at least by a factor of 10. Hence, it can be concluded that the conventional approach of theoretical estimation of the rate of intramolecular energy transfer fails to reach an agreement with the experimental results. On the other hand, the quantum dynamical simulations on the Rho1-BODIPY1 molecular dyad show that it is the transient coherence which determines the ultrafast energy transfer. Therefore, the inference is also that Förster theory cannot describe the ultrafast energy transfer in the rhodamine-BODIPY dyads.

The last part of the work elucidates the photochemical mechanism behind uncaging in the DEACM class of photocages in which the thiocyanate (-SCN), azide ($-N_3$) and carbonate act as the different leaving groups (LG). The one- (1D) and two-dimensional (2D) potential energy surface (PES) scans help in understanding the excited-state kinetics in which the dissociative DEACM-LG bond length along with the dihedral angle of the LG relative to the coumarin scaffold are the geometric parameters mediating the dissociation kinetics. The time-dependent density functional theory (TDDFT) calculations reveal some important factors influencing the dissociation kinetics. One is a cross-over between an initially excited S_1 ($\pi - \pi^*$) state localized on the DEACM moiety and a dissociative state localized on the LG whose electronic character dominates the S_1 state at larger bond distances and the

other factors are the geometric parameters i.e., the dissociative DEACM-LG bond length and the dihedral angle of the LG relative to the coumarin scaffold. The DEACM-SCN species dissociates very fast as compared to the DEACM-N_3 and DEACM-Carb species. The reason behind this phenomenon is attributed to the steepness in the potential energy barriers in the three species. The DEACM-N_3 and the DEACM-Carb moieties have higher energy barrier whereas the DEACM-SCN moiety has a barrierless pathway enabling an ultrafast dissociation. This theoretical study could be helpful in rational design of coumarin caged systems to enhance uncaging rates and quantum yields.

EXTERNAL CONTRIBUTIONS

Except where stated otherwise by reference or acknowledgement, the work presented was generated by myself under the supervision of my advisors during my doctoral studies. All contributions from colleagues are explicitly referenced in the thesis. The material listed below was obtained was obtained in the context of collaborative research:

- The experimentally measured absorption spectra of Rho1-BODIPY1 dyad presented in fig. 46 in Section 4.9.2 were provided by Rebekka Weber from the group of Prof. Dr. Alexander Heckel (Institute for Organic Chemistry and Chemical Biology, Goethe University Frankfurt, Max-von-Laue-Str. 7, 60438 Frankfurt, Germany).
- The experimentally measured one-photon and two-photon fluorescence spectra of the rhodamine derivatives in fig. 38 in Section 4.5.3, the absorption spectra of the Rho4-BODIPY2 in fig. 53 in Section 4.11.2 and the time-resolved spectroscopic measurements of the Rho4-BODIPY2 dyad presented in figs. 57 and 58 in Section 4.11.6 were provided by Marvin Asido from the group of Prof. Dr. Josef Wachtveitl (Institute for Physical and Theoretical Chemistry, Goethe University Frankfurt, Max-von-Laue-Str. 7, 60438 Frankfurt, Germany).
- The quantum dynamical investigations on the slightly adapted Rho1-BODIPY1 dyad presented in figs. 50 and 51 were performed by Maximiliane Horz within the group of Prof. Dr. Irene Burghardt (Institute for Physical and Theoretical Chemistry, Goethe University Frankfurt, Max-von-Laue-Str. 7, 60438 Frankfurt, Germany).

Frankfurt am Main, Januar 2022

Madhava Shyam
Niraghatam

BIBLIOGRAPHY

[1] M. Abe, Y. Chitose, S. Jakkampudi, P. T. T. Thuy, Q. Lin, B. T. Van, A. Yamada, R. Oyama, M. Sasaki, C. Katan, *Synthesis* **2017**, *49*, 3337–3346.

[2] K. Aidas, C. Angeli, K. L. Bak, V. Bakken, R. Bast, L. Boman, O. Christiansen, R. Cimiraglia, S. Coriani, P. Dahle, E. K. Dalskov, U. Ekström, T. Enevoldsen, J. J. Eriksen, P. Ettenhuber, B. Fernández, L. Ferrighi, H. Fliegl, L. Frediani, K. Hald, A. Halkier, C. Hättig, H. Heiberg, T. Helgaker, A. C. Hennum, H. Hettema, E. Hjertenæs, S. Høst, I.-M. Høyvik, M. F. Iozzi, B. Jansík, H. Aa. Jørgen, Jensen, D. Jonsson, P. Jørgensen, J. Kauczor, S. Kirpekar, T. Kjærgaard, W. Klopper, S. Knecht, R. Kobayashi, H. Koch, J. Kongsted, A. Krapp, K. Kristensen, A. Ligabue, O. B. Lutnæs, J. I. Melo, K. V. Mikkelsen, R. H. Myhre, C. Neiss, C. B. Nielsen, P. Norman, J. Olsen, J. M. H. Olsen, A. Osted, M. J. Packer, F. Pawlowski, T. B. Pedersen, P. F. Provasi, S. Reine, Z. Rinkevicius, T. A. Ruden, K. Ruud, V. V. Rybkin, P. Sałek, C. C. M. Samson, A. S. de Merás, T. Saue, S. P. A. Sauer, B. Schimmelpfennig, K. Sneskov, A. H. Steindal, K. O. Sylvester-Hvid, P. R. Taylor, A. M. Teale, E. I. Tellgren, D. P. Tew, A. J. Thorvaldsen, L. Thøgersen, O. Vahtras, M. A. Watson, D. J. D. Wilson, M. Ziolkowski, H. Ågren, "The Dalton quantum chemistry program system," *WIREs Comput. Mol. Sci.* **2014**, *4*, 269–284.

[3] P. Atkins, R. Friedman, *Molecular Quantum Mechanics*, 5th ed., Oxford University Press, **2011**.

[4] P. Atkins, J. de Paula, J. Keeler, *Physical Chemistry*, 11th ed., Oxford University Press, **2018**.

[5] S. G. Awuah, Y. You, *RSC Adv.* **2012**, *2*, 11169–11183.

[6] A. Baiardi, J. Bloino, V. Barone, *J. Chem. Theory Comput.* **2009**, *9*, 4097–4115.

[7] W. Barford, *J. Chem. Phys.* **2007**, *126*, 134905.

[8] V. Barone, *J. Chem. Phys.* **2005**, *122*, 014108.

[9] V. Barone, J. Bloino, M. Biczysko, F. Santoro, *J. Chem. Theory Comput.* **2009**, *5*, 540–554.

[10] M. H. Beck, A. Jäckle, G. A. Worth, H.-D. Meyer, *Phys. Rep.* **2000**, *324*, 1–105.

[11] Y. Becker, E. Unger, M. A. H. Fichte, D. A. Gacek, A. Dreuw, J. Wachtveitl, P. J. Walla, A. Heckel, *Chem. Sci.* **2018**, *9*, 2797–2802.

[12] M. Beija, C. A. M. Afonso, J. M. G. Martinho, *Chem. Soc. Rev.* **2009**, *38*, 2410–2433.

[13] S. A. Berhe, M. T. Rodriguez, E. Park, V. N. Nesterov, H. Pan, W. J. Youngblood, *Inorg. Chem.* **2014**, *53*, 2346–2348.

[14] M. Biczysko, J. Bloino, F. Santoro, V. Barone, *Computational Strategies for Spectroscopy: From Small Molecules to Nano Systems*, John Wiley & Sons, **2012**, Chapter 8, pp. 361–443.

[15] M. Born, R. Oppenheimer, *Ann. Phys.* **1927**, *389*, 457–484.

[16] J. Bredenbeck, J. Helbing, P. Hamm, *J. Am. Chem. Soc.* **2004**, *126*, 990–991.

[17] J. Bredenbeck, J. Helbing, K. Nienhaus, G. U. Nienhaus, P. Hamm, *Proc. Natl. Acad. Sci.* **2007**, *104*, 14243–14248.

[18] J. Bredenbeck, J. Helbing, C. Kolano, P. Hamm, *ChemPhysChem* **2007**, *8*, 1747–1756.

[19] C. Brieke, F. Rohrbach, A. Gottschalk, G. Mayer, A. Heckel, *Angew. Chem. Int. Ed.* **2012**, *51*, 8446–8476.

[20] M. E. Casida, D. Jacquemin, H. Chermette, "Time-dependent density-functional theory for molecules and molecular solids," *J. Mol. Struct. (THEOCHEM)* **2009**, *914*, 1–2.

[21] M. Casida, D. P. Chong, *Time-Dependent Density-Functional Response Theory for Molecules*, *Vol. 1*, Singapore: World Scientific, **1995**, Chapter 5, pp. 155–192.

[22] J. Cerezo, F. Santoro, *J. Chem. Theory Comput.* **2016**, *12*, 4970–4985.

[23] V. Cervetto, J. Helbing, J. Bredenbeck, P. Hamm, *J. Chem. Phys.* **2004**, *121*, 5935–5942.

[24] A. H. A. Clayton, G. D. Scholes, K. P. Ghiggino, M. N. Paddon-Row, *J. Phys. Chem.* **1996**, *100*, 10912–10918.

[25] E. U. Condon, *Phys. Rev.* **1926**, *28*, 1182–1201.

[26] E. U. Condon, *Phys. Rev.* **1928**, *32*, 858–872.

[27] E. U. Condon, *Phys. Rev.* **1930**, *36*, 1121–1133.

[28] J. von Cosel, J. Cerezo, D. Kern-Michler, C. Neumann, L. J. G. W. van Wilderen, J. Bredenbeck, F. Santoro, I. Burghardt, *J. Chem. Phys.* **2017**, *147*, 164116.

[29] E. A. Coutsias, C. Seok, K. A. Dill, *J. Comput. Chem.* **2004**, *25*, 1850.

[30] C. J. Cramer, *Essentials of Computational Chemistry: Theories and Models*, 2nd ed., John Wiley & Sons, **2004**.

[31] C. Curutchet, A. Franceschetti, A. Zunger, G. D. Scholes, *J. Phys. Chem. C* **2008**, *112*, 13336–13341.

[32] A. Czader, E. R. Bittner, *J. Chem. Phys.* **2008**, *128*, 035101.

[33] M. J. Davis, C. H. Kragor, K. G. Reddie, H. C. Wilson, Y. Zhu, T. M. Dore, *J. Org. Chem.* **2009**, *74*, 1721–1729.

[34] D. L. Dexter, *J. Chem. Phys.* **1953**, *21*, 836–850.

[35] M. Di Donato, A. Iagatti, A. Lapini, P. Foggi, S. Cicchi, L. Lascialfari, S. Fedeli, S. Caprasecca, B. Mennucci, *J. Phys. Chem. C* **2014**, *118*, 23476–23486.

[36] P. A. M. Dirac, *Proc. R. Soc. A.* **1927**, *114*, 243–265.

[37] E. Doktorov, I. Malkin, V. Man'ko, *J. Chem. Phys.* **1977**, *64*, 302–326.

[38] A. Dreuw, M. A. Polkehn, R. Binder, A. Heckel, S. Knippenberg, *J. Comput. Chem.* **2012**, *33*, 1797–1805.

[39] G. Duran-Sampedro, A. R. Agarrabeitia, I. Garcia-Moreno, A. Costela, J. Bañuelos, T. Arbeloa, I. n. López Arbeloa, J. L. Chia, M. J. Ortiz, *Eur. J. Org. Chem.* **2012**, *2012*, 6335–6350.

[40] F. Duschinsky, *Acta Physicochimica U. R. S. S.* **1937**, *7*, 551–566.

[41] C. Eckart, *Phys. Rev.* **1935**, *47*, 552–558.

[42] E. Fermi, *Rend. Accad. Naz. Lincei* **1927**, *6*, 602–607.

[43] E. Fermi, *Nuclear Physics*, University of Chicago Press, Chicago, **1950**.

[44] F. J. A. Ferrer, F. Santoro, *Phys. Chem. Chem. Phys.* **2012**, *14*, 13549–13563.

[45] T. Förster, *Discuss. Faraday Soc.* **1959**, *7*, 7–17.

[46] T. Förster, *Ann. Physik.* **1948**, *2*, 55–75.

[47] L. Fournier, I. Aujard, T. Le Saux, S. Maurin, S. Beaupierre, J.-B. Baudin, L. Jullien, *Chem. - Eur. J.* **2013**, *19*, 17494–17507.

[48] J. Franck, E. G. Dymond, *Trans. Faraday Soc.* **1926**, *21*, 536–542.

[49] M. J. Frisch, G. W. Trucks, H. B. Schlegel, G. E. Scuseria, M. A. Robb, J. R. Cheeseman, G. Scalmani, V. Barone, G. A. Petersson, H. Nakatsuji, X. Li, M. Caricato, A. V. Marenich, J. Bloino, B. G. Janesko, R. Gomperts, B. Mennucci, H. P. Hratchian, J. V. Ortiz, A. F. Izmaylov, J. L. Sonnenberg, D. Williams-Young, F. Ding, F. Lipparini, F. Egidi, J. Goings, B. Peng, A. Petrone, T. Henderson, D. Ranasinghe, V. G. Zakrzewski, J. Gao, N. Rega, G. Zheng, W. Liang, M. Hada, M. Ehara, K. Toyota, R. Fukuda, J. Hasegawa, M. Ishida, T. Nakajima, Y. Honda, O. Kitao, H. Nakai, T. Vreven, K. Throssell, J. A. Montgomery, Jr., J. E. Peralta, F. Ogliaro, M. J. Bearpark, J. J. Heyd, E. N. Brothers, K. N. Kudin, V. N. Staroverov, T. A. Keith, R. Kobayashi, J. Normand, K. Raghavachari, A. P. Rendell, J. C. Burant, S. S. Iyengar, J. Tomasi, M. Cossi, J. M. Millam, M. Klene, C. Adamo, R. Cammi, J. W. Ochterski, R. L. Martin, K. Morokuma, O. Farkas, J. B. Foresman, D. J. Fox, Gaussian 16 Revision B.01, Gaussian Inc. Wallingford CT, **2016**.

[50] G. Gabor, *Biopolymers* **1968**, *6*, 809–816.

[51] L. Gartzia-Rivero, H. Yu, J. Bañuelos, I. n. López-Arbeloa, A. Costela, I. Garcia-Moreno, Y. Xiao, *Chem. Asian. J.* **2013**, *8*, 3133–3141.

[52] M. Goeldner, R. Givens, *Dynamic Studies in Biology: Phototriggers, Photoswitches and Caged Biomolecules*, Wiley-VCH, Weinheim, **2005**.

[53] T. A. Golovkova, D. V. Kozlov, C. N. Douglas, *J. Org. Chem.* **2005**, *70*, 5545–5549.

[54] M. Göppert-Mayer, *Ann. Phys.* **1931**, *9*, 273–295.

[55] C. Hamerla, C. Neumann, K. Falahati, J. von Cosel, L. J. G. W. van Wilderen, M. S. Niraghatam, D. Kern-Michler, N. Mielke, M. Reinfelds, A. Rodrigues-Correia, A. Heckel, J. Bredenbeck, I. Burghardt, *Phys. Chem. Chem. Phys.* **2020**, *22*, 13418–13430.

[56] P. Hamm, M. Lim, R. M. Hochstrasser, *J. Phys. Chem. B* **1998**, *102*, 6123–6138.

[57] P. Hamm, M. T. Zanni, *Concepts and Methods of 2DIR Spectroscopy*, Cambridge University Press, **2011**.

[58] C. A. Hammer, K. Falahati, A. Jakob, R. Klimek, I. Burghardt, A. Heckel, J. Wachtveitl, *J. Phys. Chem. Lett.* **2018**, *9*, 1448–1453.

[59] G. S. He, L.-S. Tan, Q. Zhen, P. N. Prasad, *Chem. Rev.* **2008**, *108*, 1245–1330.

[60] L. M. Herzig, I. Elamri, H. Schwalbe, J. Wachtveitl, *Phys. Chem. Chem. Phys.* **2017**, *19*, 14835–14844.

[61] P. Hohenberg, W. Kohn, *Phys. Rev.* **1964**, *136*, B864–B871.

[62] Jan von Cosel, Goethe University, Frankfurt, **2018**.

[63] F. Jensen, *Introduction to Computational Chemistry*, 2nd ed., John Wiley & Sons, **2007**.

[64] W. Kaiser, G. B. C. Garrett, *Phys. Rev. Lett.* **1961**, *7*, 229–231.

[65] A. Kamkaew, S. H. Lim, H. B. Lee, L. V. Kiew, L. Y. Chung, K. Burgess, *Chem. Soc. Rev.* **2013**, *42*, 77–88.

[66] D. Kern-Michler, C. Neumann, N. Mielke, L. J. G. W. van Wilderen, M. Reinfelds, J. von Cosel, F. Santoro, A. Heckel, I. Burghardt, J. Bredenbeck, *J. Am. Chem. Soc.* **2018**, *140*, 926–931.

[67] P. Klán, T. Šolomek, C. G. Bochet, A. Blanc, R. Givens, M. Rubina, V. Popik, A. Kostikov, J. Wirz, *Chem. Rev.* **2013**, *113*, 119–191.

[68] M. Klausen, V. Dubois, G. Clermont, C. Tonnelé, F. Castet, M. Blanchard-Desce, *Chem. Sci.* **2019**, *10*, 4209–4219.

[69] W. Koch, M. C. Holthausen, *A Chemist's Guide to Density Functional Theory*, 2nd ed., Wiley-VCH, **2001**.

[70] W. Kohn, L. J. Sham, *Phys. Rev.* **1965**, *140*, A1133–A1138.

[71] B. P. Krueger, G. D. Scholes, G. R. Fleming, *J. Phys. Chem. B* **1998**, *102*, 5378–5386.

[72] B. P. Krueger, G. D. Scholes, I. R. Gould, G. R. Fleming, *PhysChemComm* **1999**, *8*.

[73] R. Y. Lai, A. J. Bard, *J. Phys. Chem. B* **2003**, *107*, 5036–5042.

[74] J. R. Lakowicz, *Principles of Fluorescence Spectroscopy*, 3rd ed., Springer, **2006**.

[75] J. H. Lee, C. S. Lim, Y. S. Tian, J. H. Han, B. R. Cho, *J. Am. Chem. Soc.* **2010**, *132*, 1216–1217.

[76] J. Liang, H. Li, *Mol. Phys.* **2005**, *103*, 3337–3342.

[77] N. Lin, Y. Luo, K. Ruud, X. Zhao, F. Santoro, A. Rizzo, *ChemPhysChem* **2011**, *12*, 3392–3403.

[78] N. Lin, X. Zhao, A. Rizzo, Y. Luo, *J. Chem. Phys.* **2007**, *126*, 244509.

[79] Q. Lin, L. Yang, Z. Wang, Y. Hua, D. Zhang, B. Bao, C. Bao, X. Gong, L. Zhu, *Angew. Chem. Int. Ed.* **2018**, *57*, 3722–3726.

[80] S. H. Lin, Y. Fujimura, H. J. Neusser, E. W. Schlag, *Multiphoton Spectroscopy of Molecules*, Academic Press Inc., Orlando, **1984**.

[81] F. López Arbeloa, J. Bañuelos, V. Martínez, T. Arbeloa, I. L'opez Arbeloa, *Int. Rev. Phys. Chem.* **2005**, *24*, 339–374.

[82] Y. Luo, H. Ågren, S. Knuts, P. Jørgensen, *Chem. Phys. Lett.* **1993**, *213*, 356–362.

[83] P. Macak, Y. Luo, H. Ågren, *Chem. Phys. Lett.* **2000**, *330*, 447–456.

[84] P. Macak, Y. Luo, P. Norman, H. Ågren, *J. Chem. Phys.* **2000**, *113*, 7055–7061.

[85] U. Manthe, H.-D. Meyer, L. S. Cederbaum, *J. Chem. Phys.* **1992**, *97*, 3199–3213.

[86] R. M. Marglin, R. B. J. Merrifield, *J. Am. Chem. Soc.* **1966**, *88*, 5051–5052.

[87] R. M. Martin, L. Reining, D. M. Ceperley, *Interacting Electrons: Theory and Computational Approaches*, 1st ed., Cambridge University Press, **2016**.

[88] J. N. Mastron, A. Tokmakoff, *J. Phys. Chem. A* **2006**, *120*, 9178–9187.

[89] G. Mayer, A. Heckel, *Angew. Chem. Int. Ed.* **2006**, *45*, 4900–4921.

[90] W. M. McClain, *J. Chem. Phys.* **1971**, *55*, 2789–2796.

[91] D. A. McQuarrie, *Quantum Chemistry*, Viva Student Edition, **2003**.

[92] R. McWeeny, *Methods of Molecular Quantum Mechanics*, 2nd ed., Academic Press, London, **1992**.

[93] B. Mennucci, *WIREs Comput. Mol. Sci.* **2012**, *2*, 386–404.

[94] H.-D. Meyer, F. Gatti, G. Worth, *Multidimensional Quantum Dynamics: MCTDH Theory and Applications*, John Wiley & Sons, **2009**.

[95] H.-D. Meyer, U. Manthe, L. S. Cederbaum, *Chem. Phys. Lett.* **1990**, *165*, 73–78.

[96] C. B. Milojevich, D. W. Silverstein, L. Jensen, J. P. Camden, *J. Am. Chem. Soc.* **2011**, *133*, 14590–14592.

[97] C. B. Milojevich, D. W. Silverstein, L. Jensen, J. P. Camden, *J. Phys. Chem. C* **2013**, *117*, 30446–3054.

[98] P. R. Monson, W. M. McClain, *J. Chem. Phys.* **1970**, *53*, 29–37.

[99] S. Mukamel, *Principles of Nonlinear Optical Spectroscopy*, Oxford University Press, New York, **1999**.

[100] J. W. Ochterski, "Vibrational Analysis in *Gaussian*," last accessed 22.06.2021, **1999**.

[101] T. Ohtsuki, S. Kanzaki, S. Nishimura, Y. Kunihiro, M. Sisido, K. Watanabe, *Nat. Commun.* **2016**, *7*, 12501.

[102] J. P. Olson, M. R. Banghart, B. L. Sabatini, G. C. R. Ellis-Davies, *J. Am. Chem. Soc.* **2013**, *135*, 15948–15954.

[103] W. W. Parson, *Modern Optical Spectroscopy*, 2nd ed., Springer, **2015**.

[104] M. Pawlicki, H. A. Collins, R. G. Denning, H. L. Anderson, *Angew. Chem. Int. Ed.* **2009**, *48*, 3244–3266.

[105] A. P. Pelliccioli, J. Wirz, *Photochem. Photobiol. Sci.* **2002**, *1*, 441–458.

[106] A. Perot, C. Fabry, *Astrophys. J.* **1899**, *9*, 87.

[107] C. B. Reese, *Org. Biomol. Chem.* **2005**, *3*, 3851–3868.

[108] A. Rizzo, S. Coriani, K. Ruud, V. Barone, *Computational Strategies for Spectroscopy: From Small Molecules to Nano Systems*, John Wiley & Sons, **2012**, Chapter 2, pp. 77–136.

[109] A. Rodrigues-Correia, X. M. M. Weyel, A. Heckel, *Org. Lett.* **2008**, *15*, 5500–5503.

[110] E. Runge, E. K. U. Gross, *Phys. Rev. Lett.* **1984**, *52*, 997–1000.

[111] F. Santoro, *FCclasses, a Fortran 77 code.* last accessed 07/12/2020, **2018**.

[112] F. Santoro, R. Improta, A. Lami, J. Bloino, V. Barone, *J. Chem. Phys.* **2007**, *126*, 084509.

[113] F. Santoro, D. Jacquemin, *WIREs Comput Mol Sci* **2016**, *6*, 460–486.

[114] F. Santoro, A. Lami, V. Barone, *Computational Strategies for Spectroscopy: From Small Molecules to Nano Systems*, John Wiley & Sons, **2012**, Chapter 10, pp. 475–516.

[115] F. Santoro, A. Lami, R. Improta, V. Barone, *J. Chem. Phys.* **2007**, *126*, 184102.

[116] F. Santoro, A. Lami, R. Improta, J. Bloino, V. Barone, *J. Chem. Phys.* **2008**, *128*, 224311.

[117] S. K. Sarkar, S. Mukherjee, P. Thilagar, *Inorg. Chem.* **2014**, *53*, 2343–2345.

[118] A. J. Sayvetz, *J. Chem. Phys.* **1939**, *7*, 383–389.

[119] G. Scalmani, M. J. Frisch, B. Mennucci, J. Tomasi, R. Cammi, V. Barone, *J. Chem. Phys.* **2006**, *124*, 094107.

[120] Y. Shao, Z. Gan, E. Epifanovsky, A. T. Gilbert, M. Wormit, J. Kussmann, A. W. Lange, A. Behn, J. Deng, X. Feng, D. Ghosh, M. Goldey, P. R. Horn, L. D. Jacobson, I. Kaliman, R. Z. Khaliullin, T. Kuś, A. Landau, J. Liu, E. I. Proynov, Y. M. Rhee, R. M. Richard, M. A. Rohrdanz, R. P. Steele, E. J. Sundstrom, H. L. Woodcock III, P. M. Zimmerman, D. Zuev, B. Albrecht, E. Alguire, B. Austin, G. J. O. Beran, Y. A. Bernard, E. Berquist, K. Brandhorst, K. B. Bravaya, S. T. Brown, D. Casanova, C.-M. Chang, Y. Chen, S. H. Chien, K. D. Closser, D. L. Crittenden, M. Diedenhofen, R. A. DiStasio Jr., H. Do, A. D. Dutoi, R. G. Edgar, S. Fatehi, L. Fusti-Molnar, A. Ghysels, A. Golubeva-Zadorozhnaya, J. Gomes, M. W. Hanson-Heine, P. H. Harbach, A. W. Hauser, E. G. Hohenstein, Z. C. Holden, T.-C. Jagau, H. Ji, B. Kaduk, K. Khistyaev, J. Kim, J. Kim, R. A. King, P. Klunzinger, D. Kosenkov, T. Kowalczyk, C. M. Krauter, K. U. Lao, A. D. Laurent, K. V. Lawler, S. V. Levchenko, C. Y. Lin, F. Liu, E. Livshits, R. C. Lochan, A. Luenser, P. Manohar, S. F. Manzer, S.-P. Mao, N. Mardirossian, A. V. Marenich, S. A. Maurer, N. J. Mayhall, E. Neuscamman, C. M. Oana, R. Olivares-Amaya, D. P. O'Neill, J. A. Parkhill, T. M. Perrine, R. Peverati, A. Prociuk, D. R. Rehn, E. Rosta, N. J. Russ, S. M. Sharada, S. Sharma, D. W. Small, A. Sodt, T. Stein, D. Stück, Y.-C. Su, A. J. Thom, T. Tsuchimochi, V. Vanovschi, L. Vogt, O. Vydrov, T. Wang, M. A. Watson, J. Wenzel, A. White, C. F. Williams, J. Yang, S. Yeganeh, S. R. Yost, Z.-Q. You, I. Y. Zhang, X. Zhang, Y. Zhao, B. R. Brooks, G. K. Chan, D. M. Chipman, C. J. Cramer, W. A. Goddard III, M. S. Gordon, W. J. Hehre, A. Klamt, H. F. Schaefer III, M. W. Schmidt, C. D. Sherrill, D. G. Truhlar, A. Warshel, X. Xu, A. Aspuru-Guzik, R. Baer, A. T. Bell, N. A. Besley, J.-D. Chai, A. Dreuw, B. D. Dunietz, T. R. Furlani, S. R. Gwaltney, C.-P. Hsu, Y. Jung, J. Kong, D. S. Lambrecht, W. Liang, C. Ochsenfeld, V. A. Rassolov, L. V. Slipchenko, J. E.

Subotnik, T. van Voorhis, J. M. Herbert, A. I. Krylov, P. M. Gill, M. Head-Gordon, "Advances in molecular quantum chemistry contained in the Q-Chem 4 program package," *Mol. Phys.* **2015**, *113*, 184–215.

[121] H. E. Sharp, H. M. Rosenstock, *J. Chem. Phys.* **1964**, *41*, 3453–3463.

[122] Y. R. Shen, *The Principles of Nonlinear Optics*, John Wiley & Sons, New York, **1984**.

[123] J. C. Slater, *Phys. Rev.* **1951**, *81*, 385–390.

[124] G. J. Small, *J. Chem. Phys* **1971**, *54*, 3300–3306.

[125] P. T. C. So, C. Y. Dong, B. R. Masters, K. M. Berland, *Annu. Rev. Biomed. Eng* **2000**, *2*, 399–429.

[126] V. Stehr, R. F. Fink, M. Tafipolski, C. Deibel, B. Engels, *WIREs Comput Mol Sci* **2016**, *6*, 694–720.

[127] A. Szabo, N. S. Ostlund, *Modern Quantum Chemistry: Introduction to Advanced Electronic Structure Theory*, Dover, **1996**.

[128] D. J. Tannor, *Introduction to Quantum Mechanics: A time-dependent perspective*, University Science Books: USA, **2007**.

[129] F. Terenziani, "Excitation Energy Transfer," last accessed 28/06/2021, **2013**.

[130] F. Terenziani, C. Katan, E. Badaeva, S. Tretiak, M. Blanchard-Desce, *Adv. Mater.* **2008**, *20*, 4641–4678.

[131] L. H. Thomas, *Math. Proc. Camb. Philos. Soc.* **1927**, *23*, 542–548.

[132] J. Tomasi, B. Mennucci, R. Cammi, *Chem. Rev.* **2005**, *105*, 2999–3093.

[133] A. Treibs, F.-H. Kreuzer, *Justus Liebigs Ann. Chem.* **1968**, *718*, 208–223.

[134] C. A. Ullrich, *Time-Dependent Density-Functional Theory: Concepts and Applications*, Oxford University Press, **2012**.

[135] O. Vendrell, H.-D. Meyer, *J. Chem. Phys.* **2011**, *134*, 044135.

[136] H. Wang, *J. Phys. Chem. A* **2015**, *119*, 7951–7965.

[137] H. Wang, M. Thoss, *J. Chem. Phys.* **2003**, *119*, 1289–1299.

[138] P. A. Weiss, D. W. Silverstein, L. Jensen, *J. Phys. Chem. Lett.* **2014**, *5*, 329–335.

[139] L. J. G. W van Wilderen, J. Bredenbeck, *Angew. Chem. Int. Ed.* **2015**, *54*, 11624–11640.

[140] L. J. G. W. van Wilderen, A. T. Messmer, J. Bredenbeck, *Angew. Chem. Int. Ed.* **2014**, *53*, 2667–2672.

[141] L. J. G. W. van Wilderen, A. T. Messmer, J. Bredenbeck, *Angew. Chem.* **2014**, *126*, 2705–2710.

[142] E. B. Wilson, J. C. Decius, P. C. Cross, *Molecular Vibrations: The Theory of Infrared and Raman Vibrational Spectra*, McGraw-Hill, **1955**.

[143] P. G. M. Wuts, *Greene's Protective Groups in Organic Synthesis*, 5th ed., Wiley, **2014**.

[144] C. Yu, Y. Xu, L. Jiao, J. Zhou, Z. Wang, E. Hao, *Chem. - Eur. J.* **2012**, *53*, 6437–6442.

EIDESSTATTLICHE ERKLÄRUNG

Ich versichere an Eides statt durch meine eigene Unterschrift, dass ich die vorstehende Arbeit selbständig und ohne fremde Hilfe angefertigt und alle Stellen, die wörtlich oder annäherend wörtlich aus Veröffentlichungen genommen sind, als solche kenntlich gemacht habe. Die Versicherung bezieht sich auch auf in der Arbeit gelieferte Zeichnungen, Skizzen, bildliche Darstellungen und dergleichen.

Frankfurt am Main, Januar 2022

Madhava Shyam
Niraghatam